

ON THE COMPLEX STELLAR POPULATIONS OF
ANCIENT STELLAR SYSTEMS

ALESSANDRO SAVINO

A thesis submitted in partial fulfilment of the requirements of
Liverpool John Moores University
for the degree of
Doctor of Philosophy.

This research programme was carried out in collaboration with the Kapteyn
Astronomical Institute, Rijksuniversiteit Groningen.

July 2018

Declaration

The work presented in this thesis was carried out at the Astrophysics Research Institute, Liverpool John Moores University. Unless otherwise stated, it is the original work of the author.

While registered as a candidate for the degree of Doctor of Philosophy, for which submission is now made, the author has not been registered as a candidate for any other award. This thesis has not been submitted in whole, or in part, for any other degree.

Alessandro Savino
Astrophysics Research Institute
Liverpool John Moores University
IC2, Liverpool Science Park
146 Brownlow Hill
Liverpool
L3 5RF
UK

SEPTEMBER 7, 2018

Abstract

The study of ancient stellar systems in the vicinity of the Milky Way provides a wealth of information on the conditions, in the early Universe, that led to the properties we observe today in galaxies and in their constituent components. Resolved stellar populations enable us to gain detailed insights on the age and chemical composition of such stellar systems, tracing their properties on a fine spatial scale.

The deep investigation of Local Group objects revealed that even very old, low mass, stellar systems host unexpected complexities in their stellar populations. Such complexities remain largely unexplained, our understanding limited by observational and theoretical limitations.

Here I present work aimed at a deeper characterisation of the complex stellar populations in dwarf spheroidal galaxies and Galactic globular clusters. I use a combination of observational and modelling techniques to shed light on the detailed stellar properties of these objects.

Part of my investigation focuses on the horizontal branch of dwarf spheroidal galaxies. By careful modelling of the horizontal branch in the galaxy Carina, which has well known star formation history, I demonstrate that the horizontal branch contains precious information, that can be used to refine age measurements in nearby galaxies.

To this aim, I develop a new modelling method that, for the first time, combines constraints from the main sequence turn-off and the horizontal branch to provide very precise measurements of the star formation history in resolved galaxies. The combined information from different regions of the colour-magnitude diagram permits to recover

the value of mass loss experienced by red giant branch stars with very high precision. I test this technique on a range of synthetic populations and on the well studied galaxy Sculptor, demonstrating the increased age resolution that this approach provides.

I apply my modelling tool to the distant galaxy Tucana, determining a very detailed star formation history, where multiple events of star formation can be clearly distinguished. The identification of the different stellar populations on the horizontal branch permits us to characterise the spatial distribution of the star formation events in this galaxy.

I also perform a photometric study of the massive globular cluster M13, focussing on the multiple stellar populations present in this object. I identify and trace the different stellar populations out to most external regions of this cluster. The spatial distribution of these populations, which shows no sign of radial segregation, reveal the very advanced dynamical evolutionary stage of the cluster.

The work presented in this manuscript constitutes a step forward to understand the formation of low mass ancient stellar systems and paves the way for deeper studies of large samples of stellar systems in the Milky Way vicinity.

Publications

In the course of completing the work presented in this thesis, the following papers have been submitted for publication in a refereed journal:

Savino A., deBoer T.J.L., Salaris M. et al., “*MORGOTH: incorporating horizontal branch modelling into star formation history determinations*”, 2018, submitted to MNRAS

Hidalgo S.L., Pietrinferni A., Cassisi S. et al., “*The Updated BaSTI Stellar Evolution Models and Isochrones. I. Solar-scaled Calculations*”, 2018, ApJ, 856, 125H

Savino A., Massari D., Bragaglia A. et al., “*M13 multiple stellar populations seen with the eyes of Strömgren photometry*”, 2018, MNRAS, 474, 4438S

Lardo C., Salaris M., **Savino A.** et al., “*Multiple populations along the asymptotic giant branch of the globular cluster M4*”, 2017, MNRAS, 466, 3507L

Lapenna E., Lardo C., Mucciarelli A. et al., “*Lost and Found: Evidence of Second-generation Stars Along the Asymptotic Giant Branch of the Globular Cluster NGC 6752*”, 2016, ApJ, 826L, 1L

Savino A., Salaris M. and Tolstoy E., “*Inclusion of horizontal branch stars in the*

derivation of star formation histories of dwarf galaxies: The Carina dSph", 2015,
A&A, 583A, 126S

Contents

Declaration	ii
Abstract	iii
Publications	v
Contents	vii
List of Tables	x
List of Figures	xi
1 Introduction	1
1.1 Complex stellar populations in dwarf spheroidal galaxies	3
1.2 Star formation history measurements in resolved stellar systems	5
1.3 Properties of horizontal branch stars	8
1.4 Multiple stellar populations in globular clusters	12
1.5 This thesis	15
2 HB modelling of Carina	17
2.1 Introduction	17

2.2	Data	19
2.3	Synthetic horizontal branch modelling	23
2.3.1	Results with the reference simulation	25
2.4	Implications for the star formation history	30
2.5	Conclusions	37
3	SFH recovery with the HB	39
3.1	Talos, modelling the MSTO region	42
3.2	MORGOTH, including the horizontal branch	43
3.2.1	HB model computation	44
3.2.2	HB matching to the rest of the CMD	47
3.2.3	Solving for the SFH	48
3.2.4	Uncertainty estimation	49
3.3	Testing the method	51
3.3.1	Synthetic tests on simple stellar populations	51
3.3.2	Moving beyond single age synthetic models	55
3.4	The Sculptor dwarf spheroidal	58
3.5	Conclusions	64
4	The SFH of the Tucana dwarf galaxy	66
4.1	Introduction	66
4.2	Modelling the colour-magnitude diagram	68
4.3	Results and discussion	71

4.4	Conclusions	78
5	Strömgren photometry of M13	80
5.1	Introduction	80
5.2	Data reduction	83
5.3	Colour-magnitude diagram	86
5.4	M13 multiple populations	87
5.4.1	Spectroscopic confirmation	88
5.4.2	Radial profiles	92
5.5	Discussion and Conclusions	98
6	Conclusions and future outlook	100
	Bibliography	105

List of Tables

2.1	The integrated RGB mass loss (ΔM^{RGB}) prescription as originally determined for the Sculptor dSph and used for the older Carina population, together with the one used for the intermediate age population in § 2.4.	26
2.2	Age, metallicity, and normalized star formation rate of the toy SFH (see text for details).	31
5.1	Exposure times, number of frames and average seeing of our dataset. .	84
6.1	List of Galactic star clusters included in the Wide-Field Strömgren survey carried out in June 2018. Metallicities, half light radii (r_h , in arcminutes) and relaxation times at the half light radius (t_h , in years) come from the 2010 version of Harris (1996). Estimates for the mass come from Baumgardt (2017).	104

List of Figures

1.1	Distribution on the sky (top), radial density profile (bottom left) and number ratio (bottom right) of the two stellar populations identified on the HB of the Sculptor dSph. The foreground at the level of the HB is also reported for comparison. From: Tolstoy et al. (2004)	4
1.2	Synthetic Hertzsprung-Russel diagram (left) and (V-I) vs I CMD (right) of a stellar population with solar metallicity and constant star formation rate over a Hubble time. Stars corresponding to different age ranges are marked with different colours. Main sequence tracks for 1, 1.2, 1.5, 1.9, 3 and 7 M_{\odot} stars are also reported. From: Gallart et al. (2005).	6
1.3	SFH time resolution as function of cosmic look-back time, evaluated for a range of synthetic simple stellar populations. The arrow marks the age of the input stellar population. The Gaussians show the recovered SFH. The means and standard deviations of the measured distributions are also reported. From: Hidalgo et al. (2011).	7
1.4	(V-I) vs I CMD of the Sculptor dSph. The major CMD features are marked by red boxes. The HB of this galaxy can be clearly identified in the bright part of the CMD. From: de Boer et al. (2011).	9

1.5	The effect of changing stellar population parameters on the (B-V) vs V morphology of a synthetic HB, compared to a reference realisation (blue). The top panel shows the effect of increasing metallicity (red) and decreasing RGB mass loss or age of the stellar population (green). The bottom panel shows the effect of increasing helium abundance (red) and increasing the spread in the RGB mass loss (cyan). The dashed lines mark the boundary of the pulsation instability strip. Credit: M. Salaris.	10
1.6	High-resolution spectroscopy measurements of [O/Fe] and [Na/Fe] for a sample of 19 Galactic GCs. Red circles have measurements of both sodium and oxygen, while blue arrows have only upper limits in the oxygen abundance. Average measurement error bars are reported. The anticorrelation between the sodium and oxygen abundances can be clearly seen in this plot. From: Carretta et al. (2009).	12
1.7	Synthetic spectra of two RGB stars with $T_{eff} = 4476K$, $\log g = 1.2$, $[Fe/H] = -1.5$ and typical abundance patterns of the primordial/first (black) and enriched/second (red) populations. Absorption features of CN, NH and CH are indicated. Overplotted, there are the response curves of Johnson UBVI (thin black lines) and Strömgren <i>uvby</i> (grey shaded regions) passbands. From: Sbordone et al. (2011).	13
2.1	Carina dSph. <i>Upper panel:</i> Star formation rate as a function of time from the adopted SFH. <i>Lower panel:</i> Weighted mean metallicity as a function of time. The red dotted histograms show the 1σ dispersion.	20

2.2	Carina dSph. Comparison between the different fields of our data set. The black dots represent stars in the de Boer et al. (2014) photometric catalogue inside one tidal radius. The blue rectangle is the field of the Bono et al. (2010) catalogue. The red stars mark the position of RR Lyrae stars, while the blue squares are the stars with spectroscopic measurements (Helmi et al., 2006). The zero point of the horizontal and vertical axis is set to $RA = 6h\ 41m\ 36.6s$ and $Dec = -50^\circ\ 57'\ 58''$ (J2000).	21
2.3	CMD of the Carina dSph from the B10 photometric set	22
2.4	<i>Upper panel:</i> Observed CMD of the HB region of the Carina dSph from B10. Red crosses mark the position of RR Lyrae stars. The red boxes are those chosen for detailed comparison. The solid black line represents the ZAHB, extending up to a mass of $1.45M_\odot$ for a metallicity of $Z=0.0001$. <i>Lower panel:</i> The synthetic HB for Carina. The red, blue, and green dots mark stars with ages $t > 7Gyr$, $4Gyr < t < 7Gyr$, and $t < 4Gyr$ respectively.	26
2.5	<i>Upper panel:</i> Observed (red) and synthetic (blue) star counts as a function of $(B - V)$ colour in boxes B and R (left and right, respectively). The bin size is 0.015 mag. Poisson errors on the observed star counts are also displayed. <i>Lower panel:</i> As in the upper panel, but for the V magnitude.	28
2.6	Observed (black) and synthetic (red) period distribution for RR Lyrae stars. The bin size is 0.05 day. Poisson errors on the observed counts are also displayed.	29
2.7	Distribution of our HB synthetic stars in the age-metallicity plane. <i>Upper panel:</i> Synthetic generated employing our toy model SFH. <i>Lower panel:</i> Synthetic generated employing the dB14 SFH.	31

2.8	Observed CMD of Carina (black dots) superimposed on the synthetic CMD computed from our toy SFH. Colour coding is the same as Fig. 2.4.	32
2.9	Same plot as Fig. 2.5 except for our toy SFH. The rightmost panel represents the RC box. The scale on the ordinate axis is set to 2, 2, and 10 counts per tickmark for the three upper panels (from left to right) and 1, 2, and 5 counts per tickmark for the lower panels.	33
2.10	Same as Fig. 2.6 but for our toy SFH.	34
2.11	<i>Left panel:</i> Normalized MDF from red giant stars. The black histogram shows the MDF inferred from our toy model. The red shaded histogram represents the empirical distribution determined by Helmi et al. (2006) and employed by dB14. <i>Central panel:</i> as for the right panel, but with the inclusion of intrinsic measurement errors in our MDF. <i>Right panel:</i> as for the central panel, but also taking into account the observed spread in the [Ca/Fe] values of Carina stars (see text for details).	36
3.1	Flow chart representing the main procedural steps of MORGOTH. . . .	45
3.2	<i>a):</i> the (B - V) vs V Hess diagram of our old and metal poor mock SSP (t = 12.5 Gyr, [Fe/H] = -2.5 dex). <i>b):</i> The best fit Hess diagram recovered with MORGOTH.	52
3.3	Same as Fig. 3.2 but for our younger and metal richer SSP (t = 8 Gyr, [Fe/H] = -1.0 dex.)	53
3.4	The comparison between the SFHs recovered with and without the HB modelling. The red solid lines are the Gaussian functions that best fit the SFHs. The blue dashed lines mark the true age of the stellar populations. <i>a)</i> Solutions for the young metal rich SSP. <i>b)</i> Solutions for the old metal poor SSP.	54

3.5	<i>a)</i> the mock (B - V) vs V Hess diagram of our galaxy with a bursty SFH. <i>b)</i> The best fit Hess diagram recovered with MORGOTH.	56
3.6	The best fit solutions for our bursty galaxy, compared with the real values. <i>a)</i> The SFH in the age-metallicity plane. The three panels are for our input SFH, the one recovered with excluding the HB and the one recovered modelling also the HB (left, centre, right, respectively). <i>b)</i> The recovered RGB mass loss as a function of metallicity (black solid line). The red solid line is the input mass loss prescription. The dotted black lines delimit the $1-\sigma$ confidence region of our solution. <i>c)</i> The star formation rate as a function of time, recovered with and without the HB modelling. The red solid lines represent the input values. <i>d)</i> The star formation rate as a function of metallicity, recovered with and without the HB modelling. The red solid lines represent the input values.	57
3.7	<i>a)</i> the mock (B - V) vs V Hess diagram of our galaxy with a continuous SFH. <i>b)</i> The best fit Hess diagram recovered with MORGOTH.	58
3.8	The best fit solutions for our galaxy with continuous SFH, compared with the real values. <i>a)</i> The SFH in the age-metallicity plane. The three panels are for our input SFH, the one recovered with excluding the HB and the one recovered modelling also the HB (left, centre, right, respectively). <i>b)</i> The recovered RGB mass loss as a function of metallicity (black solid line). The red solid line is the input mass loss prescription. The dotted black lines delimit the $1-\sigma$ confidence region of our solution. <i>c)</i> The star formation rate as a function of time, recovered with and without the HB modelling. The red solid lines represent the input values. <i>d)</i> The star formation rate as a function of metallicity, recovered with and without the HB modelling. The red solid lines represent the input values.	59

3.9	<i>a)</i> V vs $(B-I)$ Hess map of the Sculptor dSph. The photometric catalogue is taken from de Boer et al. (2011) and it has been corrected for RR Lyrae variability. <i>b)</i> Best fit Hess diagram obtained with MORGOTH. The red solid lines mark the punishment region for RGB models.	60
3.10	<i>a)</i> The age-metallicity distribution of star formation for Sculptor, recovered with MORGOTH. <i>b)</i> The inferred RGB mass loss (black solid line). The dotted black lines mark the $1-\sigma$ uncertainties of our estimate. The red solid line shows the results from Salaris et al. (2013). <i>c)</i> Star formation rate as a function of cosmic time. The red histogram shows the solution of de Boer et al. (2012). <i>d)</i> Star formation rate as a function of metallicity.	62
4.1	The HST CMD of the Tucana dSph, from Monelli et al. (2010). The morphology of the HB is corrected for RR Lyrae variability. The major CMD features are indicated. The arrows mark the position of the HB gaps.	69
4.2	Observed (left) and best-fit (centre) Hess diagrams for Tucana, colour coded by stellar density. The right panel shows the stellar count residuals, expressed in terms of the Poisson error.	71
4.3	Total RGB mass loss as a function of metallicity, as measured from our modelling. The black solid line shows our measurements and the dashed black lines mark the one sigma confidence interval. <i>a)</i> Comparison with measurements obtained, on globular clusters, by Gratton et al. (2010) (blue) and Origlia et al. (2014) (green). <i>b)</i> Comparison with measurements obtained, on the Sculptor dSph, by Salaris et al. (2013) (red) and Savino et al. (submitted) (magenta).	72
4.4	<i>a)</i> Best-fit SFH in the age-metallicity plane, colour coded by star formation rate. <i>b)</i> Corresponding star formation rate as a function of cosmic look-back time.	73

4.5	Upper panel: the observed HB of Tucana. Lower panel: the synthetic HB from our model. Stars belonging to the oldest star formation event are coloured in blue, those belonging to the intermediate event are coloured in green and stars belonging to the most recent event are coloured in red. The dashed lines mark the approximate position of the instability strip.	74
4.6	Observed HB and RGB of Tucana. A theoretical isochrone for $t=8$ Gyr and $[Fe/H] = -1.27$, and the corresponding ZAHB locus, are superimposed. The blue point marks the ZAHB position of HB stars experiencing the RGB mass loss as measured in this study. The green point marks the ZAHB location corresponding to no RGB mass loss, i.e., the maximum HB mass obtainable from this stellar population. . .	76
4.7	Our selection criterion to isolate the three HB clumps of Tucana. The red and green box are designed to minimize contamination from less massive stars evolving towards the AGB. b) Cumulative radial distribution of the HB stars in the three clumps.	77
5.1	Archival image of M13 from Sloan Digital Sky Survey. The solid red box is the field of view of our dataset for WFC chip four. The solid green box is the field of view of NOT observations from Grundahl et al. (1998). The dashed blue circle marks M13 half-light radius.	83
5.2	The magnitude difference as a function of magnitude for the bright stars in common between our catalogue and Grundahl et al. (1998). The four panels show the photometric filters used in this work. The red points are the stars used to calibrate the magnitudes of our dataset. The dashed black lines are the zero-point corrections estimated for our photometry.	85

5.3	The photometric uncertainty as a function of magnitude for all stars with $ sharp < 0.3$. The red points are the stars selected by our photometric error cut. The dashed vertical lines mark the position of the main sequence turn-off.	86
5.4	M13 ($v - y$) vs y CMD. <i>Left panel:</i> the entire photometric catalogue. <i>Right panel:</i> only the stars selected by our cleaning criteria. Green diamonds are AGB stars with spectroscopic measurements (see § 5.4.1 for details).	87
5.5	M13 CMD in the c_y index versus the y magnitude, extracted from our final catalogue. Average error bars in c_y are plotted to permit an easy comparison with the width of the RGB.	88
5.6	M13 c_y vs y CMD (black dots). The diamonds are the stars for which we have spectroscopic data, divided into primordial (red), intermediate (blue) and extreme (green) populations. The empty diamonds are stars that we identify as AGBs.	90
5.7	M13 c_y vs y CMD (black dots). The red and blue dots represent, respectively, the primordial and enriched population as selected by our photometric criterion. The upper and lower magnitude range for our selection have been obtained by comparison with HST data. See the text for more details.	92

5.8	<p>a) M13 c_y vs y CMD from the INT catalogue (black dots). The diamonds are the stars in common with the HST catalogue, divided into primordial (red) and enriched (blue) on the basis of the HST chromosome map criterion. The solid green line shows the photometric criterion defined by equation 5.1. The dotted black lines mark the magnitude range that we use for our analysis. b) Chromosome map built from the HST dataset (black dots). The diamonds are the stars in common with the INT catalogue, divided into primordial (red) and enriched (blue) on the basis of the INT photometric criterion. The solid green line shows the criterion used to separate multiple populations, corresponding to the mean ridge line for the lower sequence, shifted by three times the photometric uncertainty.</p>	95
5.9	<p>Upper panel: the cumulative distributions for the primordial (red) and enriched (blue) populations in the central regions of M13, obtained using HST data from the UV Legacy Survey of Galactic Globular Clusters. Lower panel: the number ratio of enriched stars to primordial stars in different radial bins.</p>	96
5.10	<p>As for Fig. 5.9 but for the outer regions of M13. These distributions have been obtained using our INT catalogue.</p>	97
6.1	<p>The cumulative number of known galaxies as a function of distance from the Milky Way, from the catalogue of Karachentsev et al. (2013). The dashed lines represent the detection limits, for 10 hours of integration, with HST and JWST of either old turn-off and horizontal branch stars in a 12.5 Gyr old stellar population with a metallicity of $[Fe/H] = -2.0$.</p>	102

Chapter 1

Introduction

Since the discovery that many of the diffuse nebulae observed in the sky are external galaxies, covering a variety of morphological and structural properties (Hubble, 1925, 1926, 1929), one of the main goals of astrophysics has been to understand the conditions and the processes that led to the galaxy population we observe today. In particular, given that universe was more actively star forming at redshifts between two and three (Madau & Dickinson, 2014), an accurate characterization of the properties of stellar systems at ancient times is pivotal for a comprehensive understanding of galaxy formation and evolution.

The wide range of techniques and observations that are used to shed light on the early epochs of galaxy evolution can be divided into two broad categories. The first one aims to study stellar systems at high redshift. The biggest advantage of this approach is to directly observe the processes that shaped galaxies, making the scientific interpretation relatively straightforward. On the other hand, such studies require difficult observations, and they are often limited to the brightest and biggest objects. The other approach, often referred to as “near-field cosmology” or “stellar archaeology”, focuses on nearby systems, with the goal of reconstructing their past by looking at their current properties. Working with nearby objects has the obvious advantage that very detailed observations can be obtained, but it also requires a more sophisticated modelling to link the observables to the history of the stellar system.

In the archaeological approach, objects which are entirely composed by ancient stellar populations are very valuable, as they carry the most pristine imprint of the conditions in the early Universe, where they formed. In the Local Group, such objects mainly belong to two classes: dwarf spheroidal galaxies (dSphs) and globular clusters (GCs). For long time, these objects were thought to be relatively simple stellar systems. GCs have for long time been assumed to be the prototype of simple stellar population (i.e. a population of coeval stars characterized by a homogeneous initial chemical composition), and they have been extensively used as a laboratory to test stellar evolution models. dSphs, on the other hand, have been known for decades to present spreads in age and metallicity. Even so, these spreads were assumed to be associated with relatively simple and short star formation histories (SFHs).

In recent years ever more accurate observations have led to evidence that both GCs and dSphs host complexities in their stellar populations. Although intrinsically different in nature, these complex populations represent a challenge for the formation scenarios of these objects. Theoretical models for the formation of dSphs and GCs are currently unable to explain the complex features hosted by these stellar systems. Understanding the origin of these complex population phenomena will shed new light on the formation on stellar systems in the early universe and it will provide an important piece of information for the development of a comprehensive and satisfactory galaxy evolution framework.

In this thesis, I present work that is aimed to characterize more precisely the properties of ancient stellar populations in nearby resolved stellar systems. This is done with a range of observational and modelling techniques based on colour-magnitude diagram (CMD) analysis. One of the issues with CMD analysis is the presence of large errors in the derived age and metallicity of very old stars. In this thesis I develop a new CMD modelling technique that uses the properties of helium burning stars to provide a detailed insight into the early SFH of dSphs. In addition, GC stellar populations are analysed by making use of wide field Strömgen photometry. This technique allows to trace chemical inhomogeneities in the most external regions of GCs, that are thought to preserve the formation conditions of these objects.

1.1 Complex stellar populations in dwarf spheroidal galaxies

Among the simplest galaxies that can be found in the Local Group, it has been long recognized that dSphs are not simple stellar populations. Due to the distance of these galaxies, early studies focused on the brighter (hence easier to observe) stars, nominally the red giant branch (RGB), the helium burning stars on the horizontal branch (HB) and the helium burning variables, the RR Lyrae. However, theoretical limitations and the data quality available at the time prevented a quantitative characterisation of the SFH in these galaxies, allowing only to assess the presence of stars with a range of age and chemical composition. Evidence of metallicity spreads in the stellar population of dSphs arose from the colour distribution of their RGB stars (Zinn, 1981; Mould et al., 1984; Grillmair et al., 1996) and this was supported by spectroscopic determinations (Zinn, 1978; Lehnert et al., 1992; Suntzeff et al., 1993). Similarly, indications that dSphs have extended SFHs emerged from the analysis of their RGB stars (Aaronson & Mould, 1985), of their RR Lyrae population (Saha et al., 1986) and of their main sequence turn-off (MSTO), broader than that of GCs (Mighell, 1990; Monkiewicz et al., 1999). As increasingly accurate photometry became possible, with advent of large format CCDs, a few dSphs, such as Carina and Fornax, were identified to have experienced rather complex SFHs, revealed by the structure of their CMDs (Mighell, 1990; Smecker-Hane et al., 1994; Beauchamp et al., 1995; Stetson et al., 1998; Hurley-Keller et al., 1998). Compared to these extreme cases, the majority of dSphs were thought to have relatively simpler stellar populations, composed mainly of old stars. However, the challenging nature of the observations required to characterise these old populations, made difficult to distinguish whether the stellar content of these galaxies formed in a single event of star formation or it is the result of a more complex SFH.

This picture changed in the last 20 years. Thanks to the advent of large aperture telescopes and of the Hubble Space Telescope, evidence mounted that many dSphs host distinct stellar components. Such conclusion derived from many independent analysis approaches, such as the study of the HB and RGB morphology (e.g., Majewski

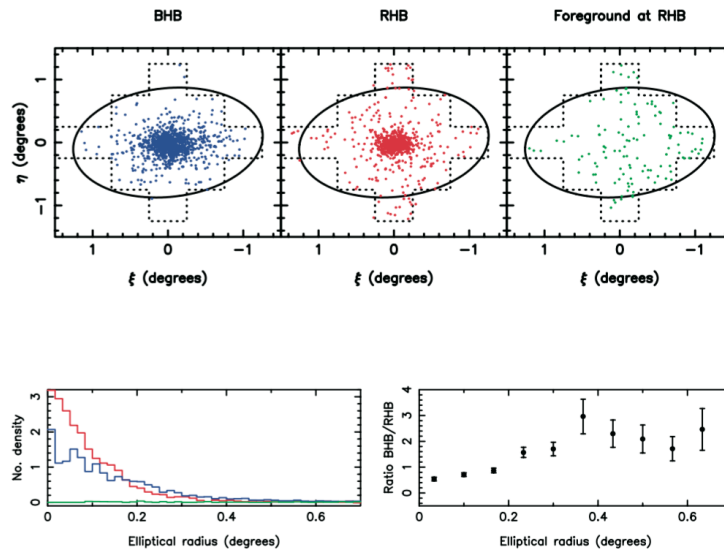


Figure 1.1: Distribution on the sky (top), radial density profile (bottom left) and number ratio (bottom right) of the two stellar populations identified on the HB of the Sculptor dSph. The foreground at the level of the HB is also reported for comparison. From: Tolstoy et al. (2004)

et al., 1999; Bellazzini et al., 2001; Harbeck et al., 2001; Tolstoy et al., 2004; Monelli et al., 2010; Weisz et al., 2014), kinematic measurements (Tolstoy et al., 2004; Battaglia et al., 2006; Ibata et al., 2006), dynamical modelling (Battaglia et al., 2008; Walker et al., 2009; Zhu et al., 2016) and pulsational characterisation of RR Lyrae stars (Saha et al., 1986; Clementini et al., 2004; Bernard et al., 2009). An example of such detections is given, for the Sculptor dSph, in Fig. 1.1.

While several scenarios have been suggested to explain the presence of these multiple stellar components, such as mergers (Amorisco & Evans, 2012a; del Pino et al., 2015), tidal interactions with the Milky Way (Pasetto et al., 2011) or bursty SFH modulated by supernova feedback (Salvadori et al., 2008; Revaz et al., 2009), a definitive answer on the origin of these complex stellar population has not yet been found. Clearly, the presence of these distinct components in the stellar content of dSphs carries a great deal of information on how these systems formed, and it needs to be reproduced in any satisfactory galaxy evolution framework.

The presence of multiple stellar populations in dwarf galaxies can also be a useful tool for a deeper understanding of these objects. While there is solid evidence that low mass galaxies are extremely dark matter dominated objects, the density profile of

their dark matter halo it is still unclear. There is substantial debate on whether the dark matter profile at the centre of these objects presents a core or a cusp (e.g., Kley *et al.*, 2002; Koch *et al.*, 2007; Battaglia *et al.*, 2008; Walker *et al.*, 2009; Walker & Peñarrubia, 2011; Agnello & Evans, 2012; Amorisco & Evans, 2012b; Breddels *et al.*, 2013). Having different populations of stars residing in the same dark matter halo is a valuable resource to the resolution of this problem. The simultaneous dynamical modelling of the distinct stellar components can constrain strongly the slope of the dark matter density profile. However, to obtain a reliable measurement, stars belonging to different populations need to be correctly identified and separated. While several approaches have been taken in this regard (e.g., Battaglia *et al.*, 2008; Walker & Peñarrubia, 2011; Zhu *et al.*, 2016), contamination still remains an issue. A deeper identification and characterisation of the distinct stellar populations that reside in dSph will certainly help to alleviate the problem.

1.2 Star formation history measurements in resolved stellar systems

In the study of extragalactic objects, distance is one of the major limiting factors in the information that can be extracted, either through direct observation or by means of subsequent modelling. Galaxies in the local vicinity can be probed up to small spatial scales and faint features. For high redshift systems, on the other hand, one is typically limited to the integrated properties. The most favorable case is when a galaxy is close enough that we can resolve the individual stars that compose it. Then, very strong constraints can be obtained on the nature of that stellar population.

One of the most interesting advantages of having deep photometry of resolved galaxies is the possibility to measure detailed SFHs, potentially back to the oldest times. It has been long known that stars of different age and metallicity occupy different regions in the CMD of a stellar population (an example is given in Fig. 1.2). This means that, with the appropriate modelling, the CMD of a galaxy can reveal a lot about the distribution

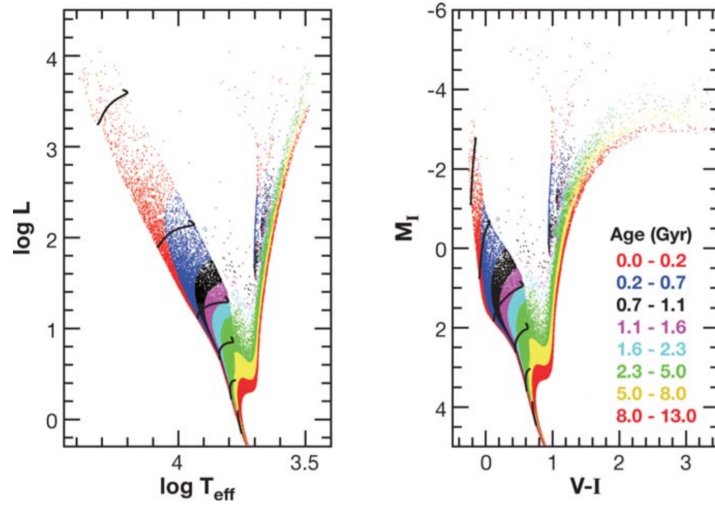


Figure 1.2: Synthetic Hertzsprung-Russel diagram (left) and (V-I) vs I CMD (right) of a stellar population with solar metallicity and constant star formation rate over a Hubble time. Stars corresponding to different age ranges are marked with different colours. Main sequence tracks for 1, 1.2, 1.5, 1.9, 3 and 7 M_{\odot} stars are also reported. From: Gallart et al. (2005).

of age and metallicity of its stars (and hence the galaxy SFH).

There are many techniques to measure the SFH of a galaxy from its CMD, but the most commonly employed make use of synthetic CMDs, which are generated from theoretical evolutionary tracks and compared to the observed CMD (e.g., Tosi et al., 1991; Tolstoy & Saha, 1996; Gallart et al., 1996). A very useful approach is to consider the CMD of a complex stellar population as the superposition of many simpler CMDs, each having a small range of age and metallicity (Aparicio et al., 1997; Dolphin, 1997). In this way, once parameters like the binary fraction and the IMF are assumed, many partial CMD models can be generated, covering a grid in the age-metallicity parameter space. These models can be linearly combined to make a complex CMD, where the weights of the linear combination represent the SFH. The best fitting SFH is the one that most resembles the observed CMD. The best fit is usually found by maximizing a merit function, that compares the stellar density across the observed and modelled CMDs. Many different implementations of this approach exist and are able to extract the SFH of resolved galaxies (e.g., Aparicio & Hidalgo, 2009; de Boer et al., 2012; Cignoni & Tosi, 2010; Harris & Zaritsky, 2012; Cignoni et al., 2015).

It is important to note that different CMD features have different importance in tracing

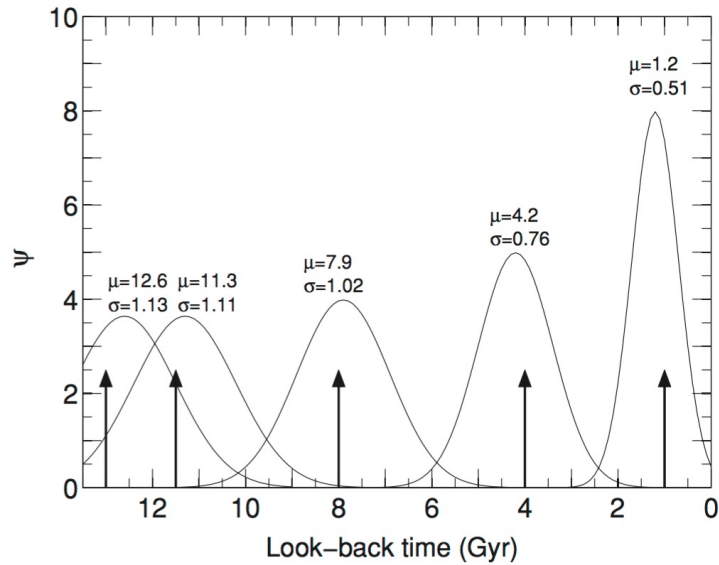


Figure 1.3: SFH time resolution as function of cosmic look-back time, evaluated for a range of synthetic simple stellar populations. The arrow marks the age of the input stellar population. The Gaussians show the recovered SFH. The means and standard deviations of the measured distributions are also reported. From: Hidalgo et al. (2011).

the SFH. Different regions of the CMD have a different dependence on the age and metallicity of the stellar population. The RGB colour, for instance, is strongly sensitive to metallicity but has a much weaker dependence on the age. For this reason the RGB alone is not sufficient to recover the star formation as a function of cosmic time. Other features have a strong dependence on age and metallicity but present theoretical challenges that make them hard to interpret. This is the main reason why the HB is typically neglected, when more suitable age indicators are available. In this regard, a wealth of information is contained in the MSTO. The brightness of this feature is sensitive to both age and metallicity, and the theoretical models for this evolutionary phase are reliable and well understood. This feature is considered to be the main age indicator of a stellar population and, when detected, it permits to reconstruct detailed SFHs that stretch back to the oldest times (Cignoni & Tosi, 2010).

In spite of the huge improvement that synthetic CMD modelling has experienced in recent years, there are still challenges. One of the most important regards the precision of the measured SFHs. Ideally, one would like to measure colours and magnitudes of stars with minimal errors, to get the most reliable SFH of the galaxy. However there

are a number of effects that limit the precision of the measurements from a CMD (Hidalgo et al., 2011; de Boer et al., 2012). This is caused by theoretical, observational and numerical problems. A first problem is the degeneracy between age and metallicity, which strongly affects the magnitude of the MSTO. Moreover, main sequence stars are relatively faint, meaning that even in close galaxies they are affected by sizeable photometric uncertainties and incompleteness. Finally, effects linked to the finite number of stars in the stellar populations, and to the binning of both the CMD and the age-metallicity parameter space degrade the information that can be extracted from the CMD. The result is that the recovered SFH for a simple stellar population will not be a Dirac delta but a Gaussian with a non-zero width (Fig. 1.3). This width informs about the time resolution of the method, the ability to resolve two events of star formation separated by a small amount of time. Time resolution tends to be worse at larger look-back times and, for very old populations, it is typically of the order of 1-1.5 Gyr. This obviously limits the constraints that can be put on the very early phases of galaxy formation.

1.3 Properties of horizontal branch stars

HB stars are bright stars that can be easily identified in the CMD of any old ($\gtrsim 8 - 10 \text{ Gyr}$) stellar population (see Fig. 1.4). These stars are the helium burning progeny of low mass ($\lesssim 1 M_{\odot}$) RGB stars. The HB phase can cover a wide effective temperature range, that includes the instability strip. When HB stars cross this region of the CMD they become pulsators, referred to as RR Lyrae variables. HB stars which are hotter and cooler than the instability strip are referred to as blue HB and red HB, respectively.

It has been known for decades that the main parameter that drives the HB morphology of a stellar population is metallicity (Sandage & Wallerstein, 1960). This is clear by looking at the population of galactic GCs. On average, metal rich clusters tend to have red HBs, while metal poor ones tend to have blue HBs. There are however exceptions, with clusters that show different HB morphologies than expected from their metallicity. This issue implies that there are additional parameters controlling a stellar population

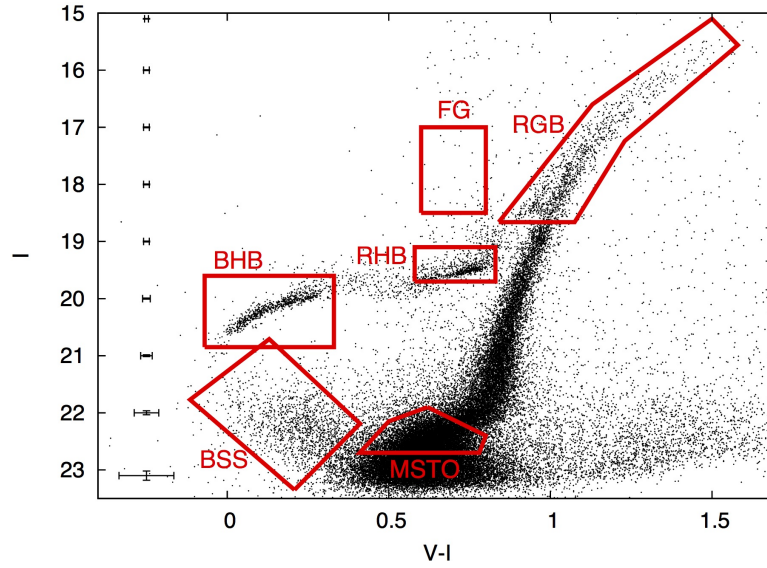


Figure 1.4: (V-I) vs I CMD of the Sculptor dSph. The major CMD features are marked by red boxes. The HB of this galaxy can be clearly identified in the bright part of the CMD. From: de Boer et al. (2011).

HB, and it is often referred as the “HB second parameter problem” (Dotter et al., 2010; Gratton et al., 2010). In reality, it is more likely that a combination of many a parameters affects the shape of the HB in GCs, making a prediction for a given stellar population difficult to make.

From the theoretical point of view, stellar models tell us that the luminosity and effective temperature of stars at the beginning of the helium burning (which define the zero age horizontal branch, or ZAHB) are uniquely determined by three ingredients: the mass of the helium core, the mass of the helium burning star and the chemical composition of the envelope (e.g., Cassisi & Salaris, 2013). For low-mass stars ($\lesssim 1.5M_{\odot}$), the mass of the helium core is mainly controlled by the chemical composition of the star (where the global metallicity and the helium abundance dominate, with a weaker dependence on the detailed chemical pattern). At a fixed stellar mass, an increase in metallicity will make the ZAHB fainter and cooler. An increase in helium abundance will make the ZAHB hotter, and its luminosity will generally increase, except for very low mass HB stars.

At fixed chemical composition, a change in the total stellar mass will not affect the luminosity of the ZAHB and only the ZAHB temperature will change, increasing for

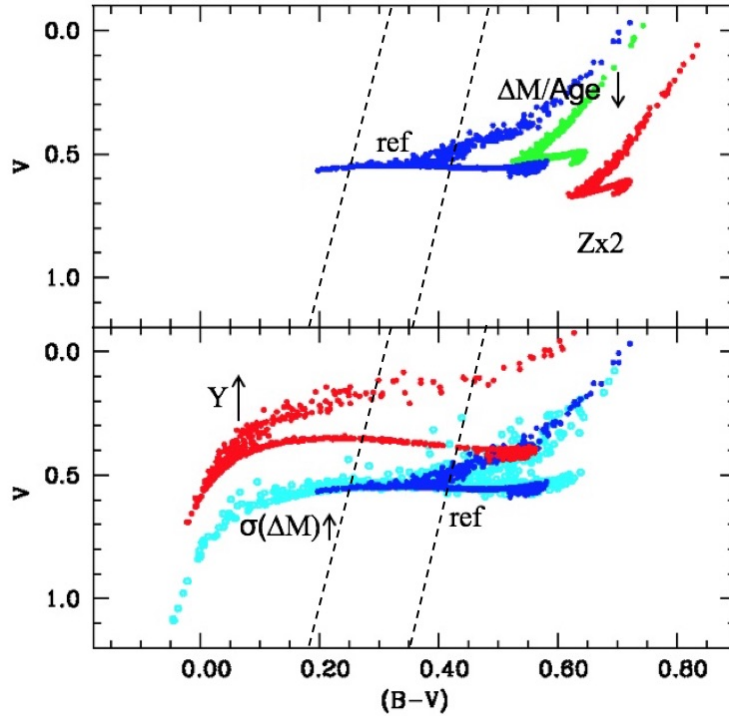


Figure 1.5: The effect of changing stellar population parameters on the (B-V) vs V morphology of a synthetic HB, compared to a reference realisation (blue). The top panel shows the effect of increasing metallicity (red) and decreasing RGB mass loss or age of the stellar population (green). The bottom panel shows the effect of increasing helium abundance (red) and increasing the spread in the RGB mass loss (cyan). The dashed lines mark the boundary of the pulsation instability strip. Credit: M. Salaris.

smaller mass values. The mass of a ZAHB star, of a given chemical composition, depends on the age of the stellar population and on the amount of mass that is lost along the RGB. So older ages (higher mass loss) will result in hotter HB stars and younger ages (lower mass loss) will result in cooler ones. At fixed age, an intrinsic spread in the value of mass loss will result in a range of ZAHB effective temperatures. The interplay among these several parameters is displayed in Fig. 1.5. Regardless of the ZAHB properties, HB stars in later stages of the helium burning will become more luminous with time and, after looping toward the blue, they will move to cooler temperatures, while they migrate to the asymptotic giant branch. During this phase is possible that these evolved stars cross the instability strip. The only exception is represented by very low mass HB stars that, instead, move directly to the hot and faint white dwarf sequence.

The morphological dependence makes the HB a promising SFH tracer in a galaxy. In

fact, if we assume helium abundance in dwarf galaxies can be scaled with metallicity (Geisler et al., 2007; Salaris et al., 2013; Fabrizio et al., 2015), then the morphology of the HB is uniquely determined by the galaxy SFH and the RGB mass loss. The possibility to extract information about the SFH from the HB presents several advantages. First, these stars are very bright. This means that they can be detected with much less exposure time compared to the old MSTO or, at fixed exposure time, they can be detected in more distant galaxies. In addition, at fixed metallicity, the colour of HB stars changes dramatically with modest changes in stellar mass. This means that, potentially, very detailed SFHs can be obtained by the modelling of this phase. Finally, as the HB is an independent SFH indicator compared to the MSTO, the age-metallicity degeneracy can be strongly alleviated when both these evolutionary phases are modelled together.

Obviously, the interpretation of the properties of HB stars requires knowledge about the amount of mass lost on the previous RGB phase. Measuring this quantity proved to be very hard for decades (Willson, 2000), also due to the peculiar nature of GCs (see § 1.4). The poor understanding of mass loss processes is the main reason why HB stars are typically neglected in the SFH measurements of Local Group dwarf galaxies.

In recent years, empirical measurements in both GCs and dSphs (Gratton et al., 2010; Salaris et al., 2013; Origlia et al., 2014) revealed that metallicity seems to be the main parameter driving mass loss, with higher metallicity corresponding to higher mass loss values during the RGB. There are also indications that, at fixed metallicity, mass loss variations among RGB stars of the same population are very small (Caloi & D’Antona, 2008; Salaris et al., 2013; Tailo et al., 2016). However, a solid understanding of the processes regulating RGB mass loss is still missing and whether RGB mass loss obeys a universal law among different stellar systems, or exhibits more complex variations, remains still an open question.

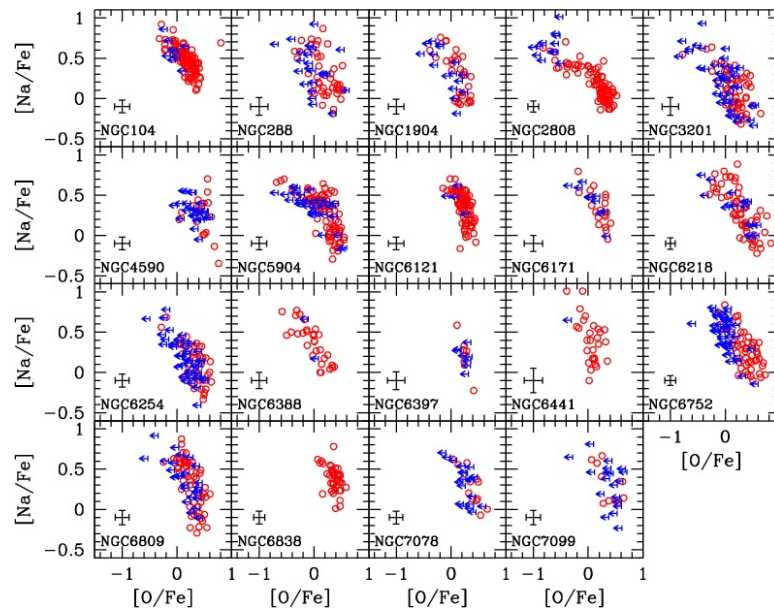


Figure 1.6: High-resolution spectroscopy measurements of $[O/Fe]$ and $[Na/Fe]$ for a sample of 19 Galactic GCs. Red circles have measurements of both sodium and oxygen, while blue arrows have only upper limits in the oxygen abundance. Average measurement error bars are reported. The anticorrelation between the sodium and oxygen abundances can be clearly seen in this plot. From: Carretta et al. (2009).

1.4 Multiple stellar populations in globular clusters

Galactic GCs were for long time believed to be the prototype of simple stellar population. They are massive star clusters with a very low binary fraction and they generally have no metallicity dispersion and negligible age spreads (Renzini & Buzzoni, 1986). Some indication that the stellar populations of GCs are chemically more complex than previously assumed came already more than 40 years ago (see, e.g, Kraft, 1979; Pilachowski et al., 1983, and references therein). However, it is with the advent of 8-m class telescopes, multi-object spectrographs and the exquisite photometry that Hubble Space Telescope can provide, that we have realised the extent and complexity of what is nowadays called the “GC multiple population phenomenon”.

When talking about multiple populations in GCs, we refer to variations in the chemical abundance pattern among stars of the same cluster. These variations are observed only in certain light elements and do not affect the abundance of iron-peak elements, thus excluding the link with supernova enrichment. Specifically, this pattern emerges

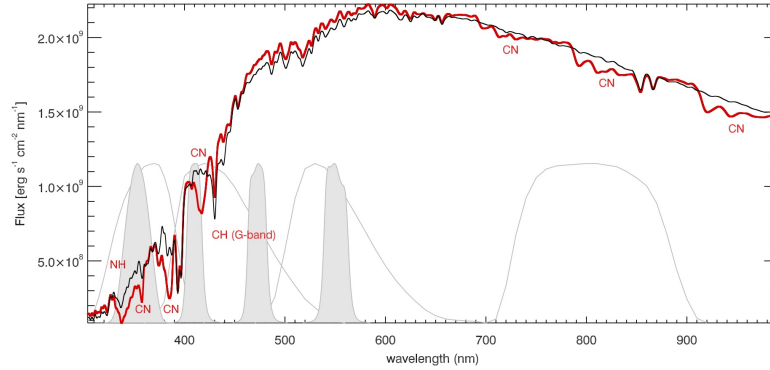


Figure 1.7: Synthetic spectra of two RGB stars with $T_{eff} = 4476K$, $\log g = 1.2$, $[Fe/H] = -1.5$ and typical abundance patterns of the primordial/first (black) and enriched/second (red) populations. Absorption features of CN, NH and CH are indicated. Overplotted, there are the response curves of Johnson UBVI (thin black lines) and Strömgren *uvby* (grey shaded regions) passbands. From: Sbordone et al. (2011).

in the form of correlation and anti-correlation in the elemental abundance of different elements (Gratton et al., 2012, and references therein). While some of the stars in a cluster have a chemical mixture fully compatible to what observed in halo stars of the same metallicity (these are generally called first, or primordial, population), a significant fraction of the cluster members are enhanced in the abundance of N and Na, and they are depleted in the abundance of C and O (second, or enriched, population). Some clusters present analogous trends in the abundance of Mg, Al and Si. These chemical differences, which are currently thought to differentiate distinct stellar populations, are observed with high-resolution spectroscopy studies, as shown in Fig. 1.6.

These distinct stellar components can also be detected with precision photometry, in the form of multiple sequences in the CMD (e.g., Piotto et al., 2007; Piotto, 2009; Piotto et al., 2012). Although these splits in the CMD are caused by several effects, depending on the passbands used and the evolutionary phase observed, the most commonly used tracer is the photometric signature of RGB stars in specific optical and ultraviolet filters. When a photometric band comprises strong features of molecules such as CN, CH and NH, the abundance of C and N leaves an imprint on the measured magnitude. This effect is clearly showed in Fig. 1.7.

An important discovery was that stars that are enriched in Na and N also show enhancement in the helium abundance (Piotto et al., 2007; Gratton et al., 2011; Dalessandro

et al., 2011). Helium abundance is one of the parameters driving the colour of the HB. Indeed, there is evidence that, within a cluster, stars belonging to different populations end up in different locations on the HB (Gratton et al., 2011; Dalessandro et al., 2011). It is now clear that the presence of multiple populations in GCs is the reason why the HB second parameter problem was so difficult to tackle. Interestingly, the chemical patterns seen in GCs are not observed in dwarf galaxies (Geisler et al., 2007; Salaris et al., 2013; Fabrizio et al., 2015). If this holds true, this might give clues as to what is special about GCs. It also makes the interpretation of HB morphology in dwarf galaxies simpler.

To date, the origin of multiple stellar populations in GCs remains a mystery. It is generally accepted that the elemental abundance variations observed in GC stars must be linked to high-temperature CNO nuclear reaction cycle. However, the astrophysical object where this nuclear processing took place, and the mechanism that led to the imprint of this chemical pattern in GC stars are still matter of debate. Many of the theoretical scenarios put forward so far invoke the pollution of gas in the cluster by objects such as rotating massive stars, asymptotic giant branch stars or supermassive stars (e.g., Ventura et al., 2001; Decressin et al., 2007; Denissenkov & Hartwick, 2014). This processed material is then locked into newly formed stars either through a subsequent event of star formation or through dynamical interactions in the dense and young proto-cluster. While each one of these models has strengths and weaknesses in reproducing the observables, there are still several major problems that have not been addressed properly, such as the fraction of primordial to enriched stars, as well as the ratio between helium enhancement and light element enrichment (Bastian et al., 2015; Bastian & Lardo, 2015). A thorough review of the main scenarios, of their successes and limitations is given in Bastian & Lardo (2017).

In recent years, interest has arisen about the radial distribution of multiple populations within GCs. Models requiring multiple star formation events predict an initial difference in concentration between the primordial and the enriched population (D’Ercole et al., 2008, 2010). A characterisation of the spatial and kinematic properties of multiple population has the potential to give strong clues about the origin of this phe-

nomenon. However, GCs are collisional stellar systems, meaning they experience a significant dynamical evolution during their lives (Spitzer, 1987). The initial conditions linked to multiple population formation will then progressively be erased by the dynamical relaxation of the cluster, which proceeds rapidly in the dense central regions. It has been shown (Vesperini et al., 2013) that an imprint of the initial spatial distribution might still present in old GCs. However, this is mainly the case for the external regions of the cluster, where dynamical timescales are much longer than in the centre. Wide-field studies become then necessary, in order to reach the outermost, pristine, regions of GCs. To date, many studies have been carried out on the radial distribution of multiple populations (Carretta et al., 2009; Lardo et al., 2011; Beccari et al., 2013; Dalessandro et al., 2014; Nardiello et al., 2015; Larsen et al., 2015; Massari et al., 2016; Nardiello et al., 2018; Dalessandro et al., 2018). However a homogeneous analysis on a large sample of clusters, over a wide field of view and on a large stellar sample is still lacking.

1.5 This thesis

In this thesis I identify and characterise the different populations of stars in ancient stellar systems. The first object I investigate is the Carina dSph (chapter 2). This chapter demonstrates the potential that the information in the HB of a galaxy has to refine our knowledge of the early phases of galaxy formation. Modelling the HB of this galaxy, I discover that certain HB features cannot be reproduced by current SFH determinations. By modelling the stellar distribution on the HB, I suggest that the SFH of this galaxy is made of more distinct events of star formation than previously assumed. A quantitative measurement of the SFH is prevented by the uncertainties inherent to the very simple modelling of only the HB.

Motivated by the previous study, I develop a new CMD modelling tool, MORGOth, presented in chapter 3. This new technique models the entire CMD of a resolved galaxy, consistently treating the MSTO region and the HB morphology in accordance with the adopted RGB mass loss. This allows to explore the mass loss parameter space,

resulting in a solid measurement of this quantity. The simultaneous modelling of many CMD features helps to soften the degeneracies and allows to greatly improve the time resolution of the resulting SFH. I apply this method to the CMD of Sculptor (previously analysed by de Boer et al., 2012; Salaris et al., 2013), recovering a very detailed SFH, where the two populations of Sculptor are clearly visible as two distinct events of star formation.

In Chapter 4 I apply my method to the distant dwarf galaxy Tucana, where the morphology of the HB clearly reveals the presence of three distinct events of star formation. I constrain the age and metallicity range of these events, focussing on how these are reflected in the details of the HB stellar distribution and of the RR Lyrae properties. This allows me to trace the spatial distribution of different star formation events in the galaxy, concluding that star formation proceeded in an outside-in progression.

Chapter 5 is focused on the multiple populations in GCs. I perform a wide-field photometric study of the cluster NGC6205 (M13). By making use of Strömgren photometry, I am able to identify RGB stars belonging to the different populations of the cluster. The wide fields allow me to trace the spatial profile of the multiple populations out to ~ 6.5 half-light radii. I find no evidence of radial segregation, probably due to the dynamical evolution of the cluster. This chapter highlights the effectiveness of wide-field, ground based, Strömgren photometry to probe the outer regions of galactic GCs, and it demonstrates how important it is to take the dynamical evolution of the cluster into account when considering the spatial distribution of multiple populations.

Finally, chapter 6 summarizes the main results described in this thesis and paves the ground for additional work to be carried out in the future. This will include a deeper study of the ancient SFH of dSphs, both in the Local Group and in external galaxy groups, and the development of a large, homogeneous survey of galactic GCs with Strömgren photometry.

Chapter 2

Horizontal branch modelling of the Carina dwarf spheroidal galaxy

This Chapter has been published as Savino et al. (2015).

2.1 Introduction

Dwarf galaxies (DGs) play a major role in modern astrophysics as they are believed to be the building blocks of the process of galaxy formation. Therefore DGs constitute a sort of fossil record of the formation epoch of the cosmic structures, and the determination of their star formation history (SFH) is crucial to understanding the mechanisms of galaxy formation and early evolution.

Detailed SFHs of DGs can only be determined in the Local Group where they can be resolved into individual stars down to the oldest main sequence (MS). These determinations are usually based on the theoretical interpretation (via stellar evolution models and isochrones) of observed colour magnitude diagrams (CMDs) and, when available, spectroscopic heavy-element abundances, typically of the red giant branch (RGB) populations. The primary age indicators for these populations are found in the main sequence turn-off (TO) region of the CMD, which is located at faint magnitudes

for the oldest populations and is very sensitive to photometric errors.

The horizontal branch (HB) is routinely neglected in SFH determinations of DGs, in spite of its brightness compared to the old TO, and the extreme sensitivity –in terms of colour and brightness distribution– to the mass and metallicity distribution of the parent stars. The reason is that the interpretation of the HB morphology in potentially simpler populations like Galactic globular clusters is problematic. Numerous studies of Galactic globular clusters (GCs) have shown that age and metallicity alone cannot account for the mean colour and extension of the HB (e.g. Catelan, 2009; Dotter et al., 2010; Gratton et al., 2010). A major difficulty is that stars arriving on the zero age HB (ZAHB) have lost mass during the previous RGB phase, and to date it is still impossible to predict from first principles the amount of mass lost by RGB stars. This issue is further complicated by the currently well-established presence in individual GCs of multiple populations of stars with enhanced helium abundances at fixed metallicity (e.g. Gratton et al., 2012, , and references therein), which affect both the colour and magnitude of the HB.

Despite these complications (and the presence of He-enhanced populations at fixed metallicity may well be just a feature of GCs), HB stars contain a wealth of information for constraining the star formation rate and metallicity evolution of DGs at the earliest times. In Salaris et al. (2013) we presented the first detailed simulation of the HB of the Sculptor Dwarf Spheroidal (dSph) galaxy by means of synthetic modelling techniques, taking into account the SFH and metallicity evolution determined from the MS and RGB spectroscopic observations. We found that the number count distribution along the observed HB could be reproduced with a simple mass loss law (that agrees very closely with the determinations by Origlia et al., 2014, for a sample of GCs), and that there is no excess of bright stars that require He-enhanced populations.

The purpose of the present work is to investigate, by means of the same synthetic HB modelling as for Sculptor, the HB populations of another DG belonging to the Local Group, the Carina dSph galaxy. This galaxy has a SFH that is very different from that of Sculptor, showing multiple star formation episodes separated in time and in the amount of stellar mass involved. Numerous studies have probed a broad

range of properties, through deep photometric investigations (e.g. Smecker-Hane et al., 1996; Monelli et al., 2003; Bono et al., 2010); spectroscopic analysis, both at medium (e.g. Smecker-Hane et al., 1999; Koch et al., 2006; Helmi et al., 2006) and high (e.g. Shetrone et al., 2003; Koch et al., 2008; Fabrizio et al., 2012; Lemasle et al., 2012; Venn et al., 2012) resolution; variable star characterization (e.g. Saha et al., 1986; Mateo et al., 1998; Dall’Ora et al., 2003; Coppola et al., 2013); and SFH analysis (e.g. Pasetto et al., 2011; Small et al., 2013; de Boer et al., 2014). These detailed works provide us with the information needed to make a meaningful comparison between synthetic and observed HB populations. In particular, our analysis will provide strong additional constraints on the controversial issue of the galaxy metallicity distribution function (MDF) as determined spectroscopically and photometrically from RGB stars (see e.g. Bono et al., 2010; VandenBerg et al., 2015, for different conclusions about the consistency between spectroscopic and photometric MDFs).

This work is structured as follows: We present the data set used for our investigations in § 2.2; we compare the synthetic and observed HBs in § 2.3; we discuss the impact of our results on the SFH in § 2.4; we present a summary in § 2.5.

2.2 Data

For the computation of our synthetic HB we employed, as reference SFH, that determined by de Boer et al. (2014) (hereafter dB14). Among the several SFHs in the literature, we chose the dB14 solution because it is the only one that combines the photometric modelling of the CMD with spectroscopic information about the metallicity distribution. Given the very high sensitivity of the HB morphology to metal content, this approach is preferable.

For the sake of homogeneity we adopted the dB14 solution obtained with the BaSTI evolutionary tracks (Pietrinferni et al., 2004), which are the same ones used in our synthetic HB calculations. Carina photometry has been divided by dB14 into three concentric annuli inside the tidal radius of the galaxy, plus a fourth field outside the

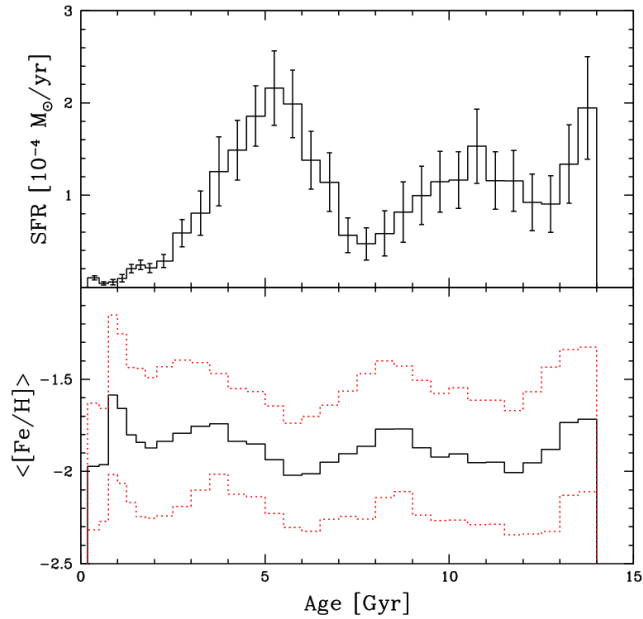


Figure 2.1: Carina dSph. *Upper panel:* Star formation rate as a function of time from the adopted SFH. *Lower panel:* Weighted mean metallicity as a function of time. The red dotted histograms show the 1σ dispersion.

tidal radius. For each field, an independent SFH has been computed. The solution gives the star formation rate in a grid of age and $[\text{Fe}/\text{H}]$ bins, and includes an estimate of $[\alpha/\text{Fe}]$ in each bin. The SFH used in our synthetic HB calculations refers to the sum of the annuli inside the tidal radius. Our synthetic HB simulation with this SFH will be called reference simulation.

Figure 2.1 shows star formation rate and mean stellar $[\text{Fe}/\text{H}]$ as a function of time. There are at least two major epochs of star formation at old and intermediate ages, ranging between 9-14 and 3-7 Gyr, respectively, while the mean metallicity remains in the relatively narrow interval $-2 < [\text{Fe}/\text{H}] < -1.6$.

We compare the synthetic CMDs with the photometric data from Bono et al. (2010) (hereafter B10), which include 4152 CCD images acquired between December 1992 and January 2005. Although the use of dB14 photometry would have granted a perfect match between the stellar population sampled and the SFH, we chose to employ a different data set because of the several advantages it offers.

First, the smaller photometric errors in the B10 CMDs, of the order of ~ 0.004 mag

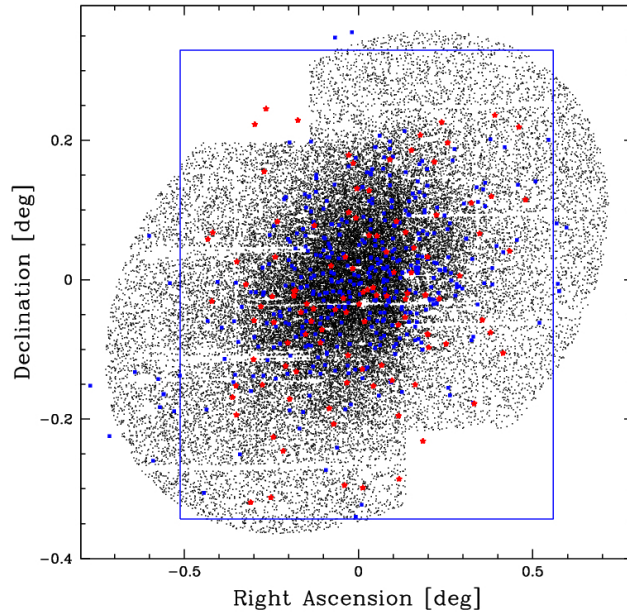


Figure 2.2: Carina dSph. Comparison between the different fields of our data set. The black dots represent stars in the de Boer et al. (2014) photometric catalogue inside one tidal radius. The blue rectangle is the field of the Bono et al. (2010) catalogue. The red stars mark the position of RR Lyrae stars, while the blue squares are the stars with spectroscopic measurements (Helmi et al., 2006). The zero point of the horizontal and vertical axis is set to RA = $6h\ 41m\ 36.6s$ and Dec = $-50^{\circ}\ 57'\ 58''$ (J2000).

at the HB level, allow for a more robust comparison between observed and synthetic CMDs. In addition, the same field has been the subject of a deep variable star search (Coppola et al. submitted). Furthermore, as the B10 photometric catalogue merges observations taken at different epochs, different random phases in different frames for a given variable star tend to be averaged. The colour and magnitude of possible undetected RR Lyrae in B10 will therefore be closer to the intrinsic mean values than it is for a single-epoch data set.

Finally, the photometric data set from dB14 retains the contamination by foreground stars of the Milky Way, as it is statistically taken into account at later stages during the SFH determination. Since Carina is a fairly diffuse stellar system at relatively low Galactic latitude, the number of foreground stars is large and, because the HB is much less populated than other evolutionary stages, the contamination can be a serious problem. The B10 catalogue, instead, has been carefully cleaned of Milky Way stars and unresolved galaxies.

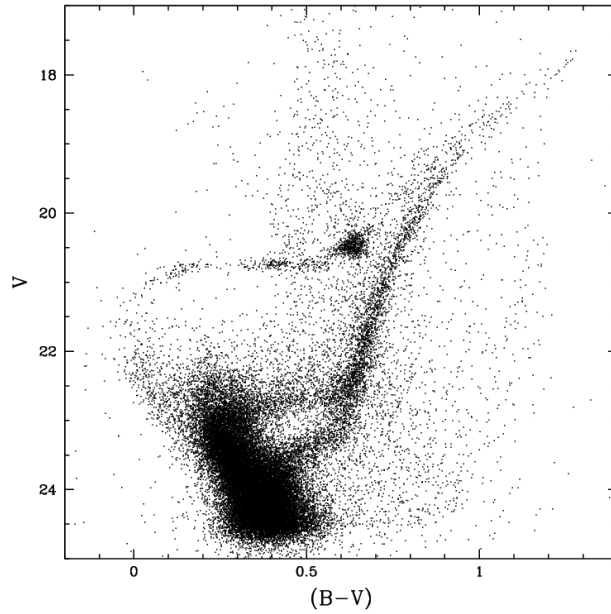


Figure 2.3: CMD of the Carina dSph from the B10 photometric set

Figure 2.2 shows the comparison between the dB14 field inside the tidal radius and the B10 field. In theory, a spatial gradient in the stellar population properties may affect our comparison because of the different areas sampled. Nonetheless, as the difference in the spatial coverage is a minor fraction of the total sampled area, and since the star counts are dominated by the central region of the galaxy, we expect this effect to be quite small. It should be also noted that the results presented in this paper still hold when the synthetic CMD is compared with the dB14 photometric catalogue.

For the variable star modelling, we used the catalogue from Coppola et al. (2015, submitted), which contains information about spatial position, intrinsic mean colour and magnitude, as well as pulsation properties of RR Lyrae stars. Using the stars' coordinates, we removed variables caught at random phase in our photometry, and replaced them with their intrinsic position on the CMD. We used the period distribution to add additional observational constraints to our HB simulations.

A glance at the Carina ($V, B - V$) CMD (Fig. 2.3) reveals the complexity of its stellar population. Two distinct MS turn offs can be clearly seen, with distinct subgiant branches merging in a very narrow RGB. The accepted scenario envisages Carina as a system that has undergone two or more major events of star formation, separated by a

period of several Gyr (Smecker-Hane et al., 1996; Monelli et al., 2003). In addition, a very young population is probably present, as suggested by the presence of a blue plume above the MS and by the detection of several Anomalous Cepheids (Monelli et al., 2003). The narrow RGB, coupled with the observed broad metallicity distribution (Koch et al., 2006; Helmi et al., 2006), suggests a conspiracy among age, metal content, and alpha element abundances that leads to all stars having a very similar colour on the RGB.

The burstiness of the Carina SFH can be seen in the helium burning loci as well, with an old extended horizontal branch that is clearly detached from a younger, more populated red clump (RC). The discreteness of the Carina stellar populations is very helpful since it allows us to simplify our analysis and model each component separately.

2.3 Synthetic horizontal branch modelling

We computed synthetic HB models with the code developed and fully described by Salaris et al. (2013) together with the BaSTI library of scaled solar evolutionary tracks (Pietrinferni et al., 2004). The use of scaled solar models with the same total metallicity $[M/H]$ of Carina stars is justified, since α -enhanced evolutionary tracks closely mimic scaled solar ones with the same total metallicity Z , in the metallicity regime of this galaxy (see e.g. Salaris et al., 1993).

We adapted the code to allow for the large mass range on the Carina HB reaching $\sim 1.4 M_{\odot}$. Higher masses correspond to a population younger than 1 *Gyr* (at Carina's typical metallicity) and can be ignored in our analysis as their magnitudes in the helium burning phase are considerably brighter than the RC and are a small contribution to the SFH of Carina.

Briefly, for each bin of the input SFH, a number of synthetic stars is generated spanning the whole range of age and metallicity inside the bin (employing a uniform probability within both age and metallicity bins), and with a value of $[\alpha/Fe]$ given for that bin. For each star, the corresponding evolutionary track is computed interpolating

in mass and metallicity the tracks from the BaSTI grid. If the age of a star is greater than the age at the RGB tip, a specific amount of mass is removed and the position on the corresponding HB track is determined.

Once the position of a star in the CMD is determined, its colour and magnitude are perturbed with a magnitude dependent Gaussian photometric error, as provided with B10 photometry. We then applied to the resultant synthetic CMD a reddening of $E(B-V) = 0.06$ (Schlegel et al., 1998) and a distance modulus of $(m - M)_0 = 20.11$, as used in dB14. Unless specified differently, we populated our synthetic CMDs with a considerably higher number of stars than the observed CMD of Carina in order to minimize the Poisson error in the final model.

The comparison of the model and the observed HB is a two-step process. First, an initial analysis is made by eye to see whether the colour extension and the main features of the HB are recovered. Then, after rescaling the total number of HB stars in the synthetic sample to the observed counterpart, we compare star counts and the mean colour and magnitude inside three boxes that encompass the RC (hereafter box RC), the red HB plus the RR Lyrae instability strip (IS – hereafter box R), and the blue HB (hereafter box B –see Fig. 2.4). If the star counts are reproduced within one σ Poisson uncertainty and the difference in the mean photometric properties are within ± 0.01 mag, we consider the synthetic model to be a good match.

We note that we take into account only the uncertainties arising from the Poisson distribution of the star counts. Another source of uncertainties is represented by the error bar associated with the star formation rate in every bin of our reference SFH. Unfortunately, including this uncertainty in our analysis is problematic because the errors are not independent from each other. Indeed, the conservation of the total number of stars and of the density distribution across the CMD required by the SFH fitting procedure introduces a correlation among the individual error bars, so a realistic modelling of the resulting uncertainty on the model HB star counts is unfeasible without the covariance matrix of the SFH solution that is not provided by dB14. Undoubtedly, the issue of a proper inclusion of the SFH errors deserves to be addressed in future works.

Clearly, theoretical HB models have also intrinsic uncertainties that affect the predicted HB star counts as a function of colour and magnitude. The main source of uncertainty is related to the treatment of the He-core convective mixing (see e.g. Cassisi & Salaris, 2013; Gabriel et al., 2014; Spruit, 2015, and references therein) that affect evolutionary timescales, luminosities and morphology of the HB tracks in the CMD. The treatment of core mixing in the adopted BaSTI models includes semiconvection, as described in Pietrinferni et al. (2004), and allows the so-called R_2 -parameter to be reproduced; this parameter is defined as the number ratio of asymptotic giant branch to HB stars, measured in a sample of galactic Globular clusters, and is very sensitive to the treatment of core mixing during the HB phase (see Cassisi et al., 2003, for a thorough discussion).

We also computed the pulsation period of synthetic stars inside the IS and compared them with the observed period distribution. We employed both the IS boundaries and the pulsational equation from Di Criscienzo et al. (2004), assuming a mixing length $ml = 1.5 H_p$. This choice reasonably matches the IS boundaries as inferred from the RR Lyrae colour distribution. The first overtone periods (P_{FO}) are related to the fundamental (P_F) by the relation $\log P_F = \log P_{FO} + 0.13$ (Di Criscienzo et al., 2004).

The stars in the so-called OR zone, in which a RR Lyrae can pulse F, FO, or double mode, were treated as F pulsators. This is, in principle, a rough approximation, but given the small fraction of FO pulsators in the observed RR Lyrae sample ($\sim 14\%$), we expect the number of FO pulsators in the OR zone to be very small.

2.3.1 Results with the reference simulation

As a starting point, we employed the mass loss law as determined by Salaris et al. (2013) for the Sculptor dSph, which gives an increasing value for the integrated RGB mass loss with increasing metallicity, as described in Table 2.1. Figure 2.4 shows the HB of Carina as well as the synthetic model computed from the SFH. Different colours mark different age ranges. For the sake of comparison, we show a synthetic HB with approximately the same number of stars as observed in Carina's HB.

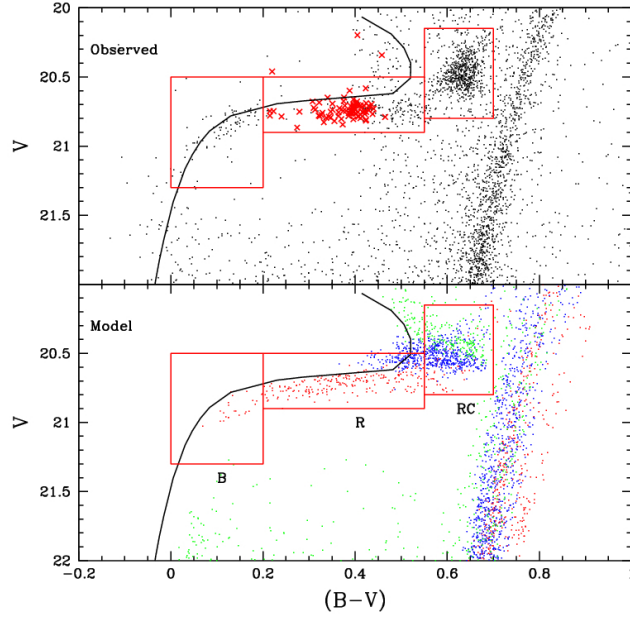


Figure 2.4: *Upper panel:* Observed CMD of the HB region of the Carina dSph from B10. Red crosses mark the position of RR Lyrae stars. The red boxes are those chosen for detailed comparison. The solid black line represents the ZAHB, extending up to a mass of $1.45M_{\odot}$ for a metallicity of $Z=0.0001$. *Lower panel:* The synthetic HB for Carina. The red, blue, and green dots mark stars with ages $t > 7\text{Gyr}$, $4\text{Gyr} < t < 7\text{Gyr}$, and $t < 4\text{Gyr}$ respectively.

Table 2.1: The integrated RGB mass loss (ΔM^{RGB}) prescription as originally determined for the Sculptor dSph and used for the older Carina population, together with the one used for the intermediate age population in § 2.4.

Metallicity range	$\Delta M_{Sculptor}^{RGB}$ M_{\odot}	$\Delta M_{t < 7\text{Gyr}}^{RGB}$ M_{\odot}
$[M/H] < -1.8$	0.095	0.048
$-1.8 < [M/H] < -1.3$	0.14	0.07
$-1.3 < [M/H]$	0.16	0.08

We can see two major differences between synthetic and observed HB. First, what is manifestly poorly reproduced is the morphology of the RC, which is more disperse than the observed one, and with a “blue cloud” of stars that blend with the red end of the old HB. Some problems are not completely unexpected since Sculptor, for which the mass loss was determined to be dependent only on the metallicity, hosts only an old stellar population. Given the mass range of the stars on the RC, their lifetime on the RGB is considerably shorter with respect to the old population. We can, therefore, naively expect the total mass loss to be different, plausibly lower for this population. We, thus, tried to modify the mass loss for the younger population, to reproduce the observations. However, in this way, the problem could only be mitigated but not totally solved.

This can be explained as follows: the RC blue cloud above the HB is primarily composed of stars with $Z \leq 0.0002$. The black solid line in Fig. 2.4 shows the zero age horizontal branch (ZAHB), extending to a mass of $1.45 M_{\odot}$, for $Z = 0.0001$, which is typical of the bulk of the metal-poor population in Carina. The position on the ZAHB becomes redder as the mass increases until, over a certain mass threshold, the ZAHB turns toward bluer colours without merging with the RC, which means that stars of that metallicity will always be bluer than the observed RC colour regardless of the mass loss.

Given that the synthetic HB is uniquely determined by the mass loss law and the input SFH, this problem is an indication that the properties of Carina stellar population recovered by the dB14 SFH model do not match exactly the true SFH.

Considering now the HB within boxes B and R (the old HB that comprises synthetic stars with age $t \geq 7Gyr$, displayed as red dots in Fig. 2.4), we can see that the total colour extension is nicely reproduced. This implies that, given the input SFH, the true mass loss for the old population cannot be drastically different from that inferred for the Sculptor dSph. Figure 2.5 compares the colour and magnitude distributions of observed and synthetic HBs. As previously stated, the Sculptor-like mass loss law nicely reproduces the colour extension of the HB. Furthermore, the relative star counts inside the two boxes are reproduced within one sigma.

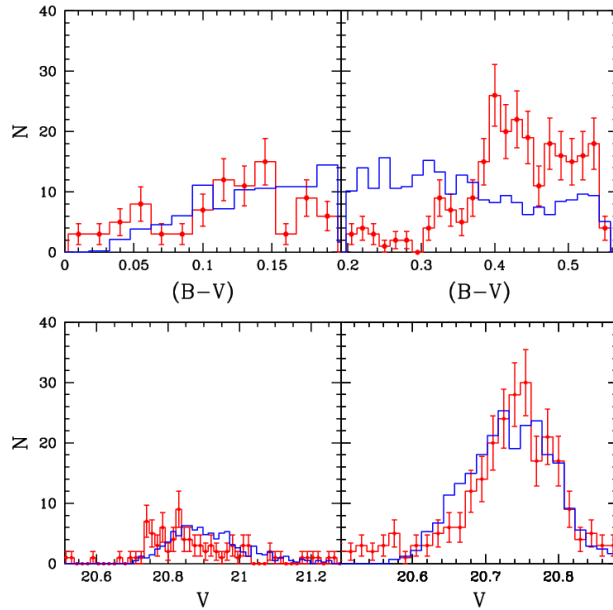


Figure 2.5: *Upper panel*: Observed (red) and synthetic (blue) star counts as a function of $(B - V)$ colour in boxes B and R (left and right, respectively). The bin size is 0.015 mag. Poisson errors on the observed star counts are also displayed. *Lower panel*: As in the upper panel, but for the V magnitude.

The fit of the mean colour and magnitude is not perfect. In box B, the computed mean colour differs by about 0.01 mag from the observed one, while the difference in magnitudes is of the order of 0.03 mag. It should be said that, in this region of the CMD star counts are low and a few stars can significantly alter the mean colour and magnitude. The synthetic distributions look very consistent within the observed error bars, suggesting that the difference in the means might be due to stochasticity.

In box R the V magnitude mean value and the overall distribution are remarkably well reproduced. The difference between observed and synthetic mean V is of the order of the photometric uncertainty. What are strikingly different are the star counts as a function of colour. The mean $(B - V)$ colour of our synthetic stars differs by more than 0.05 mag from the observed one. This can be explained by looking at the colour distribution of the two populations. The observed star counts drop for colours bluer than 0.4 and tend to increase again toward the blue HB. This gap around $(B - V) = 0.3$ is missing in the synthetic HB, which is uniformly populated.

We note here that the procedure followed by B10 to select Carina member stars is less

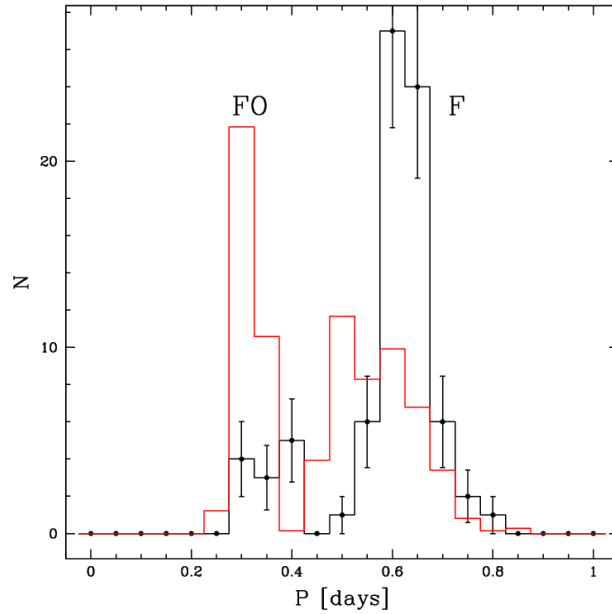


Figure 2.6: Observed (black) and synthetic (red) period distribution for RR Lyrae stars. The bin size is 0.05 day. Poisson errors on the observed counts are also displayed.

efficient for intermediate colour objects ($0.4 < (B - V) < 0.6$) and a residual amount of field stars is left in the CMD, as can be seen in Fig. 2.3. It is interesting to note that this contamination affects the star counts in box R and may be partly responsible for some of the observed stars at the red side of the gap, with $(B - V) > 0.4$. A reliable way to deal with this effect is hard to find, but we estimated the effect on the colour distribution to be of the order of 15-20% of the typical star count. We conclude that, despite the contamination, the observed gap feature exists.

The discrepancy in the distributions between model and data in the red box, which includes the IS, can also be seen in Fig. 2.6, which shows the period distributions for the RR Lyrae pulsators. The observed RR Lyrae population has a period distribution strongly peaked around $P \sim 0.6 d$ and is mainly composed of F pulsators, whereas the synthetic population has a much broader F period distribution and tends to strongly overestimate the FO population.

This can be understood by looking at the relation employed for computing the periods. The driver of the pulsational period is the effective temperature. The periods and the colour distribution are thus closely related. Both the lack of FO pulsators and of F

short periods is explained by the observed gap in the stellar distribution at the level of the IS. Our synthetic, more homogeneously populated HB naturally covers a broader range of periods and predicts too many stars in the FO zone of the IS.

To overcome this problem we tried to change the mass loss law. An analysis of age and metallicity distributions along the HB revealed that our synthetic IS is populated by a broad range of ages and metal contents. Consequently, changing the amount of mass loss for a single value or a small range of metallicities (or ages) cannot create such a well-defined gap. On the other hand, changing the whole mass loss law will considerably affect the colour extension of the blue HB, which is extremely sensitive to small mass changes. The conclusion is that the observed gap in the HB cannot be reproduced by varying the mass loss law, except by adopting a very fine-tuned ad hoc dependence on both age and metallicity, which we see as physically hard to justify.

We have therefore investigated the SFH as a possible cause of the discrepancies encountered, to assess the additional constraints that can be made on the Carina dSph SFH using the HB modelling.

2.4 Implications for the star formation history

A complete characterization of the SFH based on the HB is not feasible because of the uncertainty on the RGB mass loss. Nonetheless, as seen in the previous section, there are problems in our modelling, i.e. the RC blue cloud present in our synthetic CMD and the missing HB gap around $(B - V) \sim 0.3$, that cannot be overcome by simply changing the mass loss. The only other option for solving this problem should therefore be connected to the SFH solution we are employing.

We next investigated which component of the SFH could be responsible for these problems. The lower panel of Fig. 2.7 shows the distribution of our synthetic HB stars in the age-metallicity plane. The region of our synthetic HB which corresponds to the observed gap has been found to be mainly populated by two components which are enclosed within the two blue solid boxes: a group of metal-poor stars with ages between

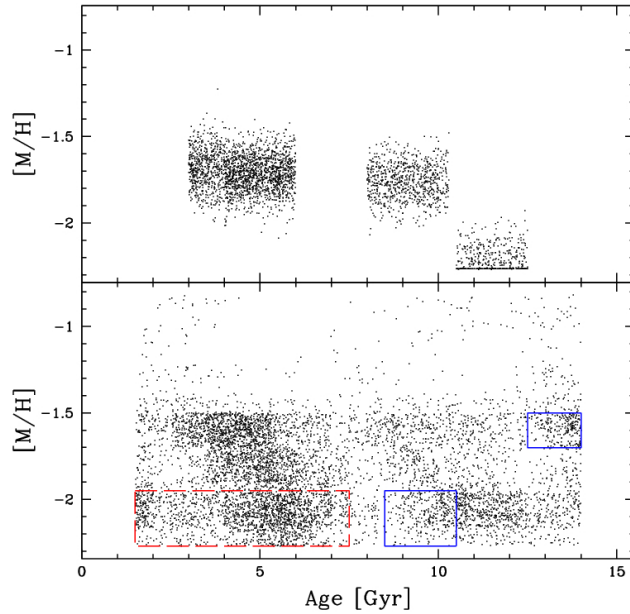


Figure 2.7: Distribution of our HB synthetic stars in the age-metallicity plane. *Upper panel:* Synthetic generated employing our toy model SFH. *Lower panel:* Synthetic generated employing the dB14 SFH.

Table 2.2: Age, metallicity, and normalized star formation rate of the toy SFH (see text for details).

	t_{min}	t_{max}	$\langle [M/H] \rangle$	SFR
	Gyr	Gyr		
Burst 1	3.0	4.0	-1.69	0.12
Burst 2	4.0	6.0	-1.71	0.39
Burst 3	8.0	10.3	-1.77	0.29
Burst 4	10.5	12.5	-2.23	0.2

9 and 10 Gyr and a group of very old, more metal-rich stars, with $[M/H] \sim -1.6$. In particular, we note that the presence of a population of old metal-rich stars is also principally responsible for the broad synthetic RGB observed in Fig. 2.4 because these stars populate its reddest part. On the other hand, the RC blue cloud feature is caused, as noted in the previous section, by stars belonging to the intermediate population and with $[M/H] \lesssim -1.9$ (red dashed box in the figure).

This finding highlights how the HB morphology can point out forbidden ranges of age and metal content that would result in unobserved features. It also suggests that the input SFH has too wide a distribution in age and metallicity, whereas Carina’s true

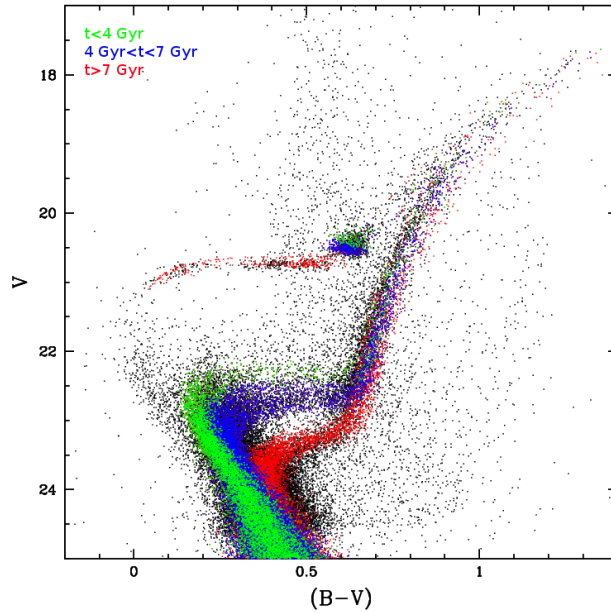


Figure 2.8: Observed CMD of Carina (black dots) superimposed on the synthetic CMD computed from our toy SFH. Colour coding is the same as Fig. 2.4.

SFH is more confined to specific regions of the age-metallicity plane. To verify this hypothesis we built a “toy” bursty SFH. We tried to reproduce a synthetic HB as similar as possible to the observed one, trying at the same time to reproduce qualitatively the RGB and the TO region. The best fit model is composed of four separate bursts whose properties are summarized in Table 2.2. We employed a flat probability distribution for the ages in the intervals given in the table, and a Gaussian $[M/H]$ distribution with the listed average values and $\sigma=0.1$ dex. We adopted the Sculptor-like mass loss law for the old population. For the intermediate population, we assumed the RGB mass loss rate to be half that of the older population, to roughly take into account the shorter RGB lifetime (for example, a $0.8M_{\odot}$ red giant, typical of a 12-13 Gyr old population, takes ~ 1.4 Gyr at $Z = 0.0001$ and ~ 2.3 Gyr at $Z = 0.001$ to reach the RGB Tip from the TO. In contrast, the time taken by a $1M_{\odot}$, typical of 5-6 Gyr old populations, is ~ 0.7 Gyr and ~ 1.3 Gyr, respectively).

Figure 2.8 shows the resulting synthetic CMD superimposed on the observed one. Our toy model roughly reproduces the morphology of the TOs and the SGBs, as well as the RGB colour and the morphology of the HB. Figure 2.9 shows the colour and

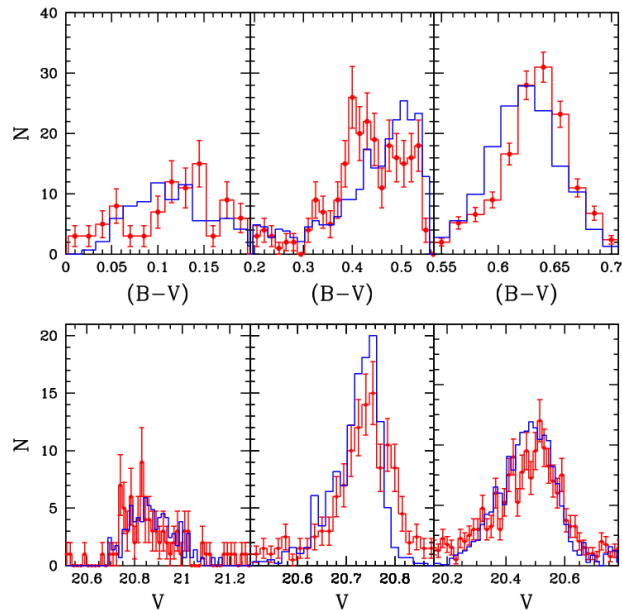


Figure 2.9: Same plot as Fig. 2.5 except for our toy SFH. The rightmost panel represents the RC box. The scale on the ordinate axis is set to 2, 2, and 10 counts per tickmark for the three upper panels (from left to right) and 1, 2, and 5 counts per tickmark for the lower panels.

magnitude distributions inside the B, R, and RC boxes in Fig. 2.4. The relative numbers inside each box are reproduced within one sigma, and the mean values of colour and magnitude differ by at most 0.01 mag from the observed ones. Even the detailed distribution looks consistent, although still with a few minor mismatches .

As an additional test, we looked at the RR Lyrae period distributions, as shown in Fig. 2.10. The F period distribution is very peaked and looks similar to the observed one. The ratio between F and FO pulsators is qualitatively reproduced as well.

It should be noted that this toy model is not intended to be the exact SFH solution, since we still lack strong constraints on the mass loss and we do not try to match the precise number density distribution across the whole CMD. Our purpose is to show how a more bursty SFH, in terms of age and metal content, is able to explain at the same time the morphology of the CMD and the detailed structure of the HB, and to suggest the age and duration of these bursts.

The age-metallicity distribution of HB stars simulated with this model is shown in the upper panel of Fig. 2.7. The comparison with the distribution in the lower panel derived

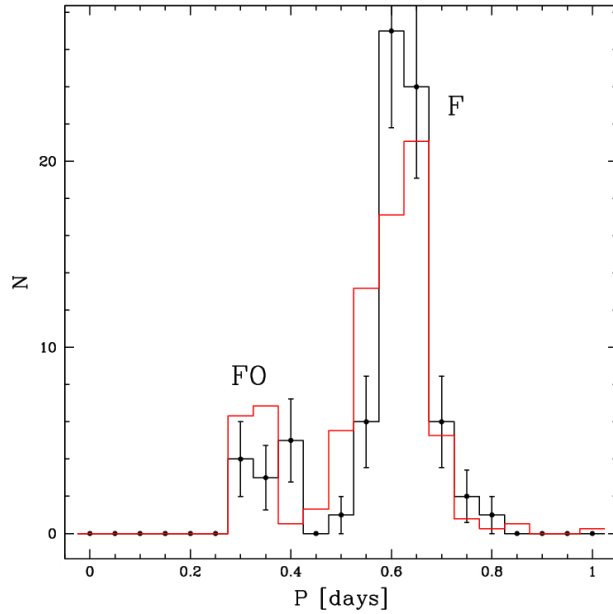


Figure 2.10: Same as Fig. 2.6 but for our toy SFH.

from the dB14 SFH allows us to identify differences and similarities between the two SFHs. The locations in the age-metallicity plane of all the star formation events of the toy model are roughly matched by those predicted by the dB14 solution, although the latter has a greater age spread, especially at old ages. Unsurprisingly, the major difference is the lack of metal-poor stars for ages younger than 10 Gyr and of very old stars with $[M/H] \sim -1.6$.

In view of this comparison, we conclude that the discrepancies between the observed HB and the synthetic helium burning population computed using the dB14 SFH are caused by two factors. First, the age resolution of the SFH naturally leads to a smooth HB, erasing any sharp substructure in the true SFH. de Boer et al. (2014) test the age resolution of their method with a series of synthetic populations generated by a 10 Myr burst centred at different ages. Even in the best case, the recovered burst duration would have been 500 Myr, which is the width of a bin element at old ages. It can be seen from their Fig. 6 that in the old age regime the recovered SFH is a Gaussian with a dispersion of the order of 1 Gyr. This effect is due to the strong degeneracy in the age-metallicity space of TO and RGB, coupled with the non-negligible photometric error at that magnitude level for a system as distant as a dwarf galaxy.

As a second point, the presence of spurious components in the dB14 SFH causes a fraction of the synthetic HB population to reside in regions of the CMD that are observed to be devoid of stars. The origin of these spurious components is not clear. A possible explanation is that any difference between the spectroscopically measured MDF, which is used as a strong constraint in the SFH characterization, and the true MDF may force the SFH determination algorithm to assign the wrong age to a fraction of stars in order to match the density distribution across the TO and the SGB regions. For the Carina dSph, the problem of metallicity is particularly thorny; the photometric and spectroscopic estimates, both high and mid resolution, do not always agree with each other (Smecker-Hane et al., 1996; Rizzi et al., 2003; Tolstoy et al., 2003; Bono et al., 2010; Koch et al., 2006; Lemasle et al., 2012).

To investigate this point, we adopted the $[\alpha/\text{Fe}]$ vs. $[\text{M}/\text{H}]$ relation, recovered from the dB14 SFH, to compute the $[\text{Fe}/\text{H}]$ values of our model. We computed our MDF from RGB stars, down to 3 magnitudes below the RGB tip, which is the typical selection criterion for DG spectroscopic measurements. Inferring the metallicity distribution from the same region of the CMD is crucial; owing to the varying evolutionary lifetime with metallicity, stars end up on the upper RGB with a different MDF with respect to the original one on the MS.

The left panel of Fig. 2.11 shows our synthetic MDF compared with the measurements from Helmi et al. (2006), which have been employed in the dB14 analysis. In contrast with our sharply bimodal distribution, the measured MDF has a much broader distribution, which is unsurprising, given that the measurement errors naturally tend to smooth the underlying distribution.

To check whether the two MDFs are consistent within the uncertainties, we convolved our MDF with a Gaussian error of 0.1 dex, which is the typical uncertainty of the Helmi et al. (2006) measurements. As can be seen in the middle panel of Fig. 2.11, the bimodality of our MDF is still clearly noticeable and we conclude that the intrinsic measurement errors are not big enough to reproduce the observed MDF width which, in addition, is fairly asymmetric.

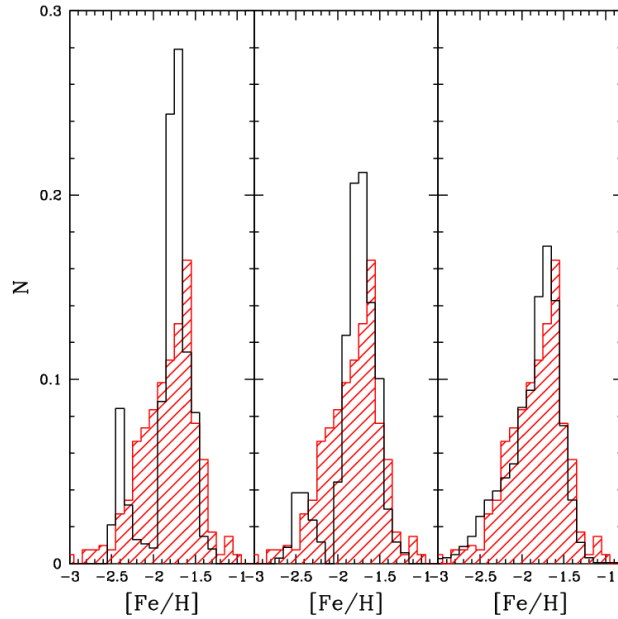


Figure 2.11: *Left panel:* Normalized MDF from red giant stars. The black histogram shows the MDF inferred from our toy model. The red shaded histogram represents the empirical distribution determined by Helmi et al. (2006) and employed by dB14. *Central panel:* as for the right panel, but with the inclusion of intrinsic measurement errors in our MDF. *Right panel:* as for the central panel, but also taking into account the observed spread in the $[\text{Ca}/\text{Fe}]$ values of Carina stars (see text for details).

It is important to notice, however, that this medium-resolution metallicity distribution has been inferred from the CaII triplet (CaT). As Battaglia et al. (2008) showed, the equivalent width (EW) of this feature is sensitive not only to the iron abundance, but also to the $[\text{Ca}/\text{H}]$ value (as is expected). Furthermore, the variation of other α -element abundances, especially the $[\text{Mg}/\text{H}]$ ratio, modifies the free electron density and, thus, the continuum opacity, indirectly affecting the measured EW. This effect has been already observed in globular clusters (Mucciarelli et al., 2012).

The MDF adopted for the dB14 SFH has been evaluated using the CaT- $[\text{Fe}/\text{H}]$ calibration by Starkenburg et al. (2010). This relation was determined assuming a fixed metal mixture with $[\alpha/\text{Fe}]=0.4$ and $[\text{Ca}/\text{Fe}]=0.25$. As noted in the same work, at fixed iron abundance, a decrease of the $[\text{Ca}/\text{Fe}]$ value of 0.25 dex causes a smaller EW of the CaT feature, mimicking a value of $[\text{Fe}/\text{H}]$ lower by ~ 0.2 dex

Several high-resolution spectroscopic investigations of Carina have found a large spread

in the abundance of elements like Ca and Mg, which has been explained as evidence of inhomogeneous mixing of the gas phase (Shetrone et al., 2003; Lemasle et al., 2012; Venn et al., 2012; Fabrizio et al., 2015). In particular, the bulk of the [Ca/Fe] measurements range from $\sim +0.3$ to slightly subsolar values. Using the CaT calibration without considering the variation in calcium abundance will then tend to underestimate the iron abundance. This has been already noticed by Venn et al. (2012).

A precise quantitative evaluation of this uncertainty is very difficult, since it requires detailed knowledge of several quantities, like the trend of the mean [Ca/Fe] value and of its spread at varying metallicity, and the accurate EW dependence on the electron donor elements' abundance. Nevertheless, as a first approximation we took this effect into account by perturbing our MDF with an asymmetric uncertainty: we assumed that half of the stars had their [Fe/H] overestimated, with a dispersion of 0.1 dex, and the other half had it underestimated, with a dispersion of 0.25 dex. This roughly takes into account the Carina observed distribution of [Ca/Fe] around the fiducial [Ca/Fe]=0.25 employed in Starkenburg et al. (2010) CaT-[Fe/H] calibration.

The resulting distribution is shown in the right panel of Fig. 2.11. The two distributions are in good agreement, suggesting that, at least qualitatively, an uncertainty of the order of 0.2-0.3 dex toward lower metallicities is able to produce the broad MDF we observe. Assuming this to be the case, this could likely lead to spurious components in the best fit SFH, as the estimated high fraction of metal-poor stars is included in the solution, with the algorithm accordingly distributing them in age to preserve the relative numbers between the two populations.

2.5 Conclusions

We have performed a detailed simulation of the HB of the Carina dSph using recent and detailed SFH estimates by dB14. We found that the overall colour extension of the old HB is reproduced well with an integrated RGB mass loss that ranges from 0.1 to $0.14 M_{\odot}$ as a function of [M/H] in complete agreement with what has been found

for the Sculptor dSph. This concordance hints that the mass loss law derived for the Sculptor dSph may also reproduce the HB morphology in other dSphs with similar metallicity.

On the other hand, we found some discrepancies with the detailed colour distribution along the old HB and RC that required a modification of the input SFH by dB14. We then built a toy bursty SFH that reproduces well the observed HB star counts in both V and $(B - V)$, and also matches qualitatively the RGB and the TO region, as well as the pulsational properties of RR Lyrae stars.

The comparison between the MDF of our bursty SFH and the one measured from the infrared CaT feature using the CaT-[Fe/H] calibration by Starkenburg et al. (2010) shows a qualitative agreement, once the range of [Ca/Fe] abundances measured in a sample of Carina stars has been taken into account, which induces a bias of the derived [Fe/H] distribution toward values that are too low. Although we emphasize that Carina is one of the few Local Group galaxies where this bias can be so severe, extra caution should be taken when using the CaT to estimate [Fe/H] in systems with poor or no constraints on the detailed metal mixture.

In conclusion, the work we have presented shows how the information contained within the HB can, in principle, be extracted and interpreted to make predictions about the properties of the stellar population in DGs. The results on the Carina dSph illustrate that the inclusion of the detailed HB morphology in the CMD analysis is able to refine the SFH determination of resolved stellar systems. Owing to the strong sensitivity of its morphology and luminosity to the age and metallicity of the parent population, the HB is a powerful benchmark to rule out forbidden ranges of age and metal content that would result in unobserved features on the CMD. This capability grants us additional resolution when pinpointing the SFH details of DGs, especially at early times.

We aim to consolidate the synthetic HB modelling technique, with the goal of making quantitative predictions on the properties of resolved stellar populations, consequently enhancing the power of CMD analysis, especially in distant systems where the old MS-TO information is hard to access.

Chapter 3

A self consistent method to model the horizontal branch in star formation history measurements

This Chapter has been submitted for publication in MNRAS.

Determining detailed star formation histories (defined as the star formation rate as a function of age and metallicity – SFHs) for a variety of different types of galaxies is important to the understanding of galaxy formation and evolution. The SFH of galaxies in the local Universe, going back to the earliest times, allows a comparison with predictions, over the same time frame, from cosmological and galaxy evolution models (see, e.g., Lanfranchi & Matteucci, 2004; Salvadori et al., 2008; Romano & Starkenburg, 2013; Starkenburg et al., 2013; Garrison-Kimmel et al., 2014; Fattahi et al., 2016; Sorce et al., 2016, for models of Local Volume galaxy properties). In this way we can constrain the conditions in the local Universe when the Milky Way and its satellites were forming.

Resolving individual stars, in a stellar population, down to the main sequence turn-off (MSTO), allows a detailed and accurate SFH to be determined. Unfortunately, with current observational capabilities we are only able to resolve a small sample of

galaxies, primarily dwarf galaxies in the Local Group (e.g., Tolstoy et al., 2009; Weisz et al., 2011). Even so, the information that we can extract from these few nearby dwarf galaxies is very valuable and complements what we can learn from the study of unresolved, more distant galaxies (e.g., Gallazzi et al., 2008; Boylan-Kolchin et al., 2016; Goddard et al., 2017). Moving beyond the satellites of the Milky Way, detecting the main sequence of the old population becomes challenging, and photometric data is often only able to reach down to the upper red giant branch (RGB) and the horizontal branch (HB) of galaxies (e.g., Martin et al., 2016, 2017).

To determine the SFH of a resolved galaxy, a common approach is to build synthetic colour-magnitude diagrams (CMDs) to compare observed and predicted stellar distributions (e.g., Tosi et al., 1991; Tolstoy & Saha, 1996; Aparicio et al., 1997; Dolphin, 1997; Harris & Zaritsky, 2001; Cignoni & Tosi, 2010). An important contribution towards quantitative and reliable SFH determinations came with the work of Dolphin (2002), who formalized many of the numerical challenges in SFH recovery, and performed detailed modelling of an homogeneous Hubble Space Telescope (HST) dataset of nearby galaxies. This framework was further developed with a thorough characterization of the typical uncertainties in SFH determinations by Dolphin (2012) and Dolphin (2013). The SFH determinations for nearby galaxies, using synthetic techniques, are extensive, thanks especially to the exquisite sensitivity and resolving power provided by the advent of HST (e.g., Aloisi et al., 1999; Cole et al., 2007; Monelli et al., 2010; Weisz et al., 2011, 2014; Sacchi et al., 2016).

One of the limitations of current SFH determinations of old stellar populations in the Local Group is that synthetic diagrams are typically only generated up to the tip of the RGB. Therefore, they neglect the later stages of stellar evolution, most importantly the HB phase. The main reason for this has been that RGB mass loss plays a strong role in shaping the morphology of the HB. As the mass loss phenomenon has proven difficult to characterize, this dependence has made predicting the HB of a given stellar population challenging (e.g., Gratton et al., 2010, and references therein).

Accurately modelling the HB, taking into account the uncertain value of RGB mass loss, is a promising way forward to improve the SFH for nearby and distant galaxies.

HB stars are much brighter than their MSTO counterparts, making them less affected by photometric uncertainties. This means that the HB morphology can be accurately characterized out to the edge of the Local Group and beyond. Theoretical calculation shows that the photometric properties of HB stars depend mostly on the metallicity and the stellar mass (e.g., Iben & Rood, 1970). For a fixed chemical composition, the mass of HB stars is determined by the age of the stellar population and the amount of mass lost during the previous RGB phase. Thus, at fixed mass loss the HB morphology depends only on the SFH of the system. Furthermore, when the MSTO morphology is included, then the modelling of the HB has the potential to dramatically mitigate the age-metallicity degeneracy, as two stellar populations with different age-metallicity combination and the same MSTO luminosity will look quite different on the HB. For these reasons, the information contained in the HB can be used to significantly improve the recovered SFH, provided that we can accurately model the mass loss (Savino et al., 2015).

Previous studies have used the HB to constrain SFHs both in the Milky Way (Preston et al., 1991; Santucci et al., 2015) and in external galaxies (Schulte-Ladbeck et al., 2002; Rejkuba et al., 2011; Grocholski et al., 2012). In particular, the analysis of the HB has been crucial to constrain the stellar population properties of galaxies beyond our nearest Galactic companions. However, determining an accurate star formation rate, comparable to measurements from the MSTO, from the HB has been difficult to achieve. This is because these previous analyses necessarily employed theoretical isochrones for the HB modelling. These are built assuming a specific, only loosely constrained, mass loss efficiency. Not allowing this parameter to vary has a big impact on the measured SFH from the HB.

In this paper we present a new SFH determination technique that flexibly and consistently takes into account the HB morphology when analysing the CMD of a galaxy, allowing a variation in the RGB mass loss. This approach provides precise SFHs and accurate measurements of the RGB mass loss. The starting point of MORGOTh (**M**odelling **O**f **R**esolved **G**alaxies with **O**ptimized **T**urn-off and **H**B synthesis), was the routine TALOS (de Boer et al., 2012), which has been modified to include synthetic

HBs, to handle the effect of mass loss and to recover a more detailed SFH, using the information of all the evolutionary phases up to the end of the early asymptotic giant branch.

In §3.1 we give a brief description of how TALOS works, in §3.2 we describe MORGOTH, in §3.3 we present several performance tests using mock observations and in §3.4 we model the stellar population of the Sculptor dwarf spheroidal galaxy (dSph). In §3.5 we summarize our work.

3.1 Talos, modelling the MSTO region

TALOS is a SFH determination routine presented and verified in de Boer et al. (2012). The algorithm of this code has been developed according to the prescriptions laid out in Dolphin (2002). For a complete description, see de Boer et al. (2012). Here we briefly describe the main features.

TALOS determines a galaxy SFH by comparing an observed CMD to a set of synthetic simple stellar population models, which are generated on a fine grid of age and metallicity (in this paper the term metallicity always refers to $[\text{Fe}/\text{H}]$). Parameters like the binary fraction, the $[\alpha/\text{Fe}]$ vs $[\text{Fe}/\text{H}]$ relation and the initial mass function (IMF) are taken into account. If available, spectroscopic metallicities can also be added as an additional constraint. The synthetic metallicity distribution functions (MDFs) are generated, sampling the model CMDs as the spectroscopic measurements. In order to accurately compare models and observations, observational effects are added to the synthetic CMDs to match the observations. Such effects include distance, reddening, photometric uncertainties and completeness fractions across the CMD. Measurement errors and completeness levels are determined from artificial star tests.

After transforming the CMDs into Hess diagrams (defined as the density map of stars across the CMD, given a specific CMD binning scheme), TALOS searches for the linear combination of models that minimize the Poisson analogue of the unreduced χ^2

function:

$$\chi_P^2 = 2 \sum_i (m_i - n_i + n_i \ln \frac{n_i}{m_i}) \quad (3.1)$$

Where m_i is the number of stars in a synthetic Hess bin, and n_i is the observed star count in the same bin. The spectroscopic MDF comparison can be included in the χ_P^2 evaluation. The MDFs are rescaled, to compensate for the CMD having many more stars and consequently dominating the final χ_P^2 . Given the regularity of the χ_P^2 surface built in this way, the minimum can be located through the Fletcher-Reeves-Polak-Ribiere (FRPR) algorithm (Press et al., 1992), which makes use of a conjugate gradient technique. This method is very fast, as it makes use of the function derivatives to find the minimum.

The uncertainties are evaluated by fitting the SFH for a range of different CMD sampling and parameter space sampling combinations (the former relates to the CMD binning choice while the latter relates to the binning of the age-metallicity grid). For each combination of CMD and parameter space sampling, a solution is evaluated and is used to estimate the uncertainties related to data sampling. These arise because the observed stellar population is finite in size and is just a random realization of the underlying statistical population. For this reason, the best fit solution is used to replace 20 per cent of the observed stars and to create several alternative CMDs from which the SFH is recovered again. In this way, the final SFH solution is the average of at least 100 different solutions, from which the standard deviation is used to estimate the uncertainties on the star formation rates.

3.2 **MORGOTH, including the horizontal branch**

The main complication of including the HB morphology (when modelling the SFH of a galaxy) is that the amount of mass lost by RGB stars during their evolution is uncertain. Thus, in principle, exploring the effects of different mass loss assumptions requires to generate a complete synthetic CMD for each mass loss prescription, as done, for instance, in Salaris et al. (2013). Such an approach has a high computational

cost and makes an extensive exploration of the mass loss parameter space challenging.

Fortunately, another approach is possible, because the helium core mass in low mass stars ($M \lesssim 1.5M_{\odot}$) at the start of the helium burning phase is very weakly dependent on the progenitor mass (see, e.g., Salaris & Cassisi, 2005). In addition, the progenitor RGB evolution is essentially insensitive to mass loss, unless extremely high values are considered. These properties imply that a theoretical HB evolutionary track, of a given stellar mass and chemical composition, is independent of the combination of progenitor mass (i.e., age of the stellar population) and total RGB mass loss. This property of HB stars is commonly exploited in synthetic stellar population generations (e.g., Salaris et al., 2013; Savino et al., 2015; Tailo et al., 2016).

Using this technique in *MORGOTH*, we treat the HB modelling in a straightforward way. We compute a grid of synthetic simple stellar populations, using the same procedure of *TALOS*, which are generated up to the tip of the RGB. This grid covers a range of stellar population ages and metallicities. These simple stellar population models are then complemented by a grid of synthetic HB models, which are calculated for different metallicities and HB stellar masses (see § 3.2.1 for details). These HB models contain stars between the onset of quiescent helium burning and the first thermal pulse on the asymptotic giant branch. For any arbitrary mass loss prescription, we can map the HB grid onto the simple stellar population grid. After appropriately rescaling the stellar density, the two synthetic models are combined to create a self-consistent Hess diagram that includes the helium burning phase. In this way we greatly reduce the number of the required synthetic CMD computations.

In the rest of this section we will provide a general description of the *MORGOTH* approach, which is also schematized in Figure 3.1.

3.2.1 HB model computation

The stellar evolution library we use to compute all the synthetic models is the *BaSTI* stellar library (Pietrinferni et al., 2004, 2006). These models have been successfully

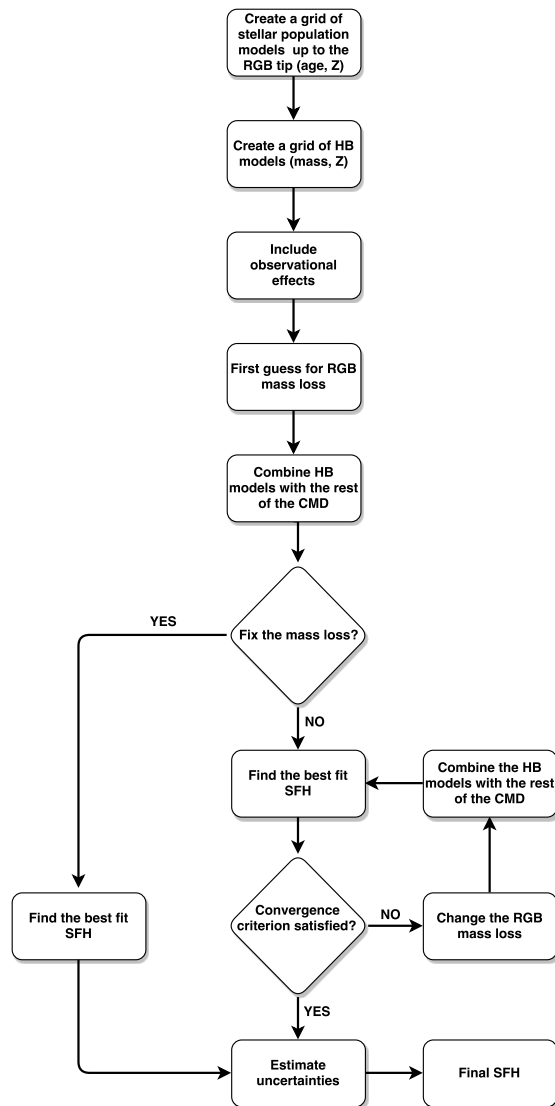


Figure 3.1: Flow chart representing the main procedural steps of MORGOTH.

tested and used to reproduce the HB properties of globular clusters and resolved galaxies (e.g., Cassisi et al., 2003; Dalessandro et al., 2011, 2013; Salaris et al., 2013). To increase our method’s versatility, we extended the HB track grid, computing additional tracks, reaching a mass of $1.5M_{\odot}$ at the beginning of the He-burning phase (A. Pietrinferni, private communication). With this extended grid we can create synthetic CMDs of intermediate age stellar populations (as young as $\sim 2 \text{ Gyr}$), that typically present a red clump instead of an HB. In the following we describe how we calculate our grid of synthetic HB models.

For any given simple stellar population, we assume that RGB stars lose a total amount of mass ΔM , which has a Gaussian distribution with standard deviation $\sigma_{\Delta M}$. The extent of this Gaussian spread is a chosen parameter. Recent studies of globular clusters and dwarf galaxies suggest that the dispersion is of the order of a few thousandths of solar mass, at fixed metallicity (Caloi & D’Antona, 2008; Salaris et al., 2013; Tailo et al., 2016). In all the synthetic CMDs shown in this paper, we keep this value fixed at $\sigma_{\Delta M} = 0.005M_{\odot}$. Thus the resultant HB stars will have a Gaussian distribution of mass on the zero age horizontal branch (ZAHB), with an average value \overline{M}_{ZAHB} . We generate a set of synthetic HB models, covering a grid of $[\text{Fe}/\text{H}]$ and \overline{M}_{ZAHB} values.

To populate a synthetic HB model, we need to calculate a distribution of stellar masses and a distribution of ages since the start of the helium burning. Aside from the obvious constraint that the average mass on the ZAHB should be equal to \overline{M}_{ZAHB} , the synthetic HB model has to satisfy two more conditions. The first one is that stars in later phases of the helium burning should be, on average, more massive than stars on earlier phases. This is because, at fixed mass loss, stars near the end of the helium burning come from more massive progenitors. The second constraint is that, when the synthetic HB is matched to a simple stellar population CMD, the number of stars on the HB and the stellar mass distribution have to be consistent with the adopted IMF.

These constraints are satisfied by adopting the following procedure. For each value of $[\text{Fe}/\text{H}]$ and \overline{M}_{ZAHB} we assume a realistic mass loss value (we adopt the prescription from Origlia et al., 2014, but the choice is not particularly critical) to calculate the progenitor mass that produces \overline{M}_{ZAHB} . We call this value M_{ZAHB}^{prog} . We then consider

an age range $\Delta t = 200 Myr$ (the exact value is not important, as long as it is larger than the maximum HB lifetime) and determine the range of initial masses whose age at the tip of the RGB is in the range between the age of M_{ZAHB}^{prog} , denoted as t_0 , and $t_0 - \Delta t$. We extract a mass distribution for this range of progenitors according to the chosen IMF, and assign to them the corresponding HB mass by adding the selected value of the RGB mass loss (with a Gaussian distribution). For each HB mass we calculate its location along the HB phase considering that its age from the ZAHB is equal to the age difference at the tip of the RGB between its progenitor and the progenitor of \bar{M}_{ZAHB} . HB masses whose age would be larger than their HB lifetime are considered to be evolved off the HB.

When the mass loss is changed, we calculate a correction factor, for each HB model, that takes into account the change in the progenitor masses. This factor is the ratio, coming from the IMF, of the new progenitor number abundance to the original progenitor number abundance. We use this factor to scale the HB density distribution so that our models are always consistent with the adopted IMF. However, due to the short lifetime of HB stars, this correction is very small.

3.2.2 HB matching to the rest of the CMD

Given the two grids of models we generate (one for the HBs and one for the rest of the CMDs), we are able to create synthetic CMDs that include the HB and the early asymptotic giant branch. Our method is able to create synthetic CMDs for any arbitrary mass loss prescription, as the only requirement is to calculate \bar{M}_{ZAHB} for a given population, to choose the appropriate HB model and to rescale its Hess diagram consistently with the IMF. The simple stellar population model and its corresponding HB are then merged into a single Hess diagram. As the HB grid is discrete, there might be small differences between the \bar{M}_{ZAHB} of a given population and the closest HB model. For this reason, a very fine mass sampling of the HB grid is preferred. We find a compromise between mass sampling and computation speed with a mass sampling step of $0.005 M_{\odot}$.

In practice, we need a functional form for the integrated RGB mass loss. Recent studies of globular clusters, have suggested a linear relationship between the total amount of mass lost on the RGB and the cluster metallicity (Gratton et al., 2010; Origlia et al., 2014). Within the error bars, the two results agree and are also compatible with the mass loss inferred by Salaris et al. (2013) for the Sculptor dSph. For this reason, we parametrise the integrated RGB mass loss as a linear function of the stellar population metallicity, and hence describe it with two parameters. It is possible that this parametrisation may be inappropriate when modelling younger stellar populations, as they have not been considered by these observational studies and for which the RGB evolutionary timescale (likely related to the total mass loss) is significantly affected by the stellar mass or, in other words, age.

It should be noted that assumptions about the mass loss functional form only affect the link between the global CMD models and their related HB models.

3.2.3 Solving for the SFH

With the set of models and the matching procedure described above, we can estimate the SFH of a resolved stellar population using all the evolutionary phases that are typically observed in old and intermediate age stellar populations.

The main difference with previous CMD modelling approaches is the RGB mass loss and how it is treated. One way to proceed is to make an assumption about the mass loss parameters and to keep them fixed. The adopted mass loss is then used to match the HB models with the rest of the CMDs and the SFH computation proceeds as in TALOS.

Another approach is to leave the mass loss parameters free and explore them in determining the best fit SFH solution. On the HB, the age of the stellar population and the RGB mass loss are degenerate, as different combinations of these two variables can lead to the same mass on the HB. If an independent age indicator is available (for example the MSTOs), then this degeneracy can be broken and both the age and the

mass loss can be determined. The HB models and the rest of the CMDs are rematched every time the mass loss is changed. This process continues until the combination of SFH and mass loss parameters that minimises χ_P^2 is found.

The simplest approach would be to solve for the mass loss parameters and the SFH at the same time. Unfortunately, this creates local minima, meaning that analytical optimisation techniques, such as the conjugate gradient descent used in TALOS, do not converge. Alternatively, heuristic methods, such as Markov-Chain Monte Carlo or genetic algorithms, are very slow, given the high dimensionality of the problem, introduced by the many CMD models.

As explained in Dolphin (2013), if one or more parameters affects our CMD models, we assume that the likelihood of a given parameter combination is proportional to the maximum SFH likelihood (hence the minimum χ_P^2) that is obtained with that combination. We, thus, explore the mass loss parameter space using an amoeba minimiser (Nelder & Mead, 1965) until we find the mass loss prescription that produces the minimum χ_P^2 . We chose the amoeba minimisation because of its speed, compared to other heuristic methods. The topology of our χ_P^2 surface is such that this method efficiently converges without getting trapped in the local minima, because the scale and the depth of these minima, which arise because of our discrete HB grid, are much smaller than the large scale structure of the χ_P^2 surface. This means that the minimiser is insensitive to the presence of these features until it is very close to the global minimum (on a scale of the order of the HB mass sampling). This hybrid analytical-heuristic approach allows us to overcome the local minima introduced by the mass loss while exploiting the speed of the SFH optimisation.

3.2.4 Uncertainty estimation

Once the preferred SFH solution has been found, we estimate the uncertainties on our solution. New solutions are calculated for different CMD and parameter space samplings, as described in §3.1. For each of these, we generate additional CMDs using the *Poisson statistics* criterion, described in Aparicio & Hidalgo (2009). For

each bin i of the observed CMD, we replace the measured stellar count n_i with a new value, drawn from a Poisson distribution with expectation value $\lambda = n_i$. This way of treating data sampling uncertainties is preferred to the one used in TALOS because it does not depend on the best-fit SFH, which in some cases can be quite different from the true SFH of the galaxy.

The way mass loss is incorporated into the uncertainty estimation depends on whether the mass loss parameters were fixed. If the mass loss is left as a free parameter, a separate measurement is made for each SFH solution. Similarly to the SFH analysis, the final mass loss is the average of all the individual solutions and the uncertainties on the parameters are taken from the standard deviation of the solutions. To prevent solutions that produce a bad CMD fit to contaminate our final measurement, we apply a median absolute deviation cut on the mass loss parameter distribution, eliminating strong outliers.

If the mass loss parameters are fixed, the uncertainties on these parameters are taken into account when computing uncertainties on the SFH. The entire process of SFH evaluation and the uncertainty estimation is repeated several times. Each time the mass loss parameters are extracted from a gaussian distribution, according to their uncertainties. The final SFH will be the one corresponding to the mass loss that gives us the minimum χ_P^2 , whereas the scatter of the entire set of solutions will provide the confidence interval for our SFH.

The uncertainties on the individual star formation rates are highly correlated. For this reason, MORGOTH also estimates the covariance between each pair of star formation rates. This information is needed to treat the SFH uncertainties properly, as varying the star formation rates independently could lead to unphysical solutions that, for example, do not match the mass of the galaxy.

3.3 Testing the method

It is necessary, with a new analysis procedure, to benchmark it on science cases for which the expected solution is known. The standard approach is to use synthetic CMDs with known SFH to emulate typical observed examples. Of course, these tests on mock observations represent an idealised situation and, while they are very useful to assess the validity of the adopted methodology, they are free from many of the systematics that affect real data. These include uncertainties in the modelling parameters (such as distance, reddening and alpha enhancement), mismatch with theoretical models and poor characterisation of the observational effects. Thus we also apply the method to a well studied object with a previous analysis, including the HB modelling. This has the advantage of working with “real” data, testing that the method is robust against the typical uncertainties of observations. However, in this case, we can only make a relative comparison with previous studies.

In this section and in the next, we are going to present tests on synthetic datasets of different complexity, and on the well studied Local Group galaxy Sculptor.

3.3.1 Synthetic tests on simple stellar populations

The performance of a SFH modelling technique should pass the basic test applied to simple stellar populations (Hidalgo et al., 2011; de Boer et al., 2012). A simple stellar population is defined to have a single age and metallicity (or an age and metallicity spread negligible compared to the resolution of either). SFH determinations are typically broader than the input, due to a combination of observational effects and methodological limitations (Hidalgo et al., 2011; Aparicio et al., 2016). Measuring this effect for a simple stellar population gives an estimate of the intrinsic time resolution of the method.

Globular clusters are typically characterized by very small spreads in age and metallicity, and could be interesting targets to test MORGOth on real simple stellar populations. However, globular clusters are also known to have substantial spreads in certain

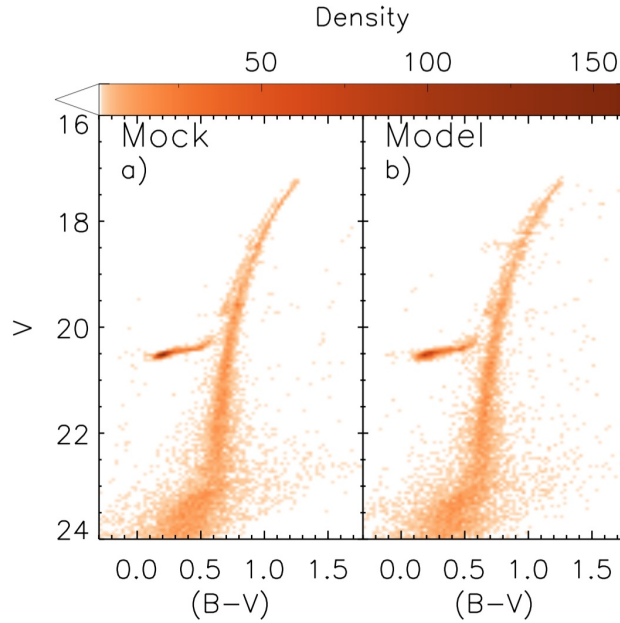


Figure 3.2: *a*): the $(B - V)$ vs V Hess diagram of our old and metal poor mock SSP ($t = 12.5$ Gyr, $[\text{Fe}/\text{H}] = -2.5$ dex). *b*): The best fit Hess diagram recovered with MORGOTH.

light element abundances, including helium (see, e.g., Gratton et al., 2012, and references therein). These spreads have a strong influence on the morphology of the HB, which thus cannot be straightforwardly linked to the SFH of the system. The field stellar populations of nearby resolved galaxies show no sign of these abundance patterns (Shetrone et al., 2003; Geisler et al., 2007; Fabrizio et al., 2015), but they are characterised by an extended SFH. For this reasons, we can only perform simple tests on synthetic data.

We created a synthetic CMD for two simple stellar populations. One with an age of 12.5 Gyr and a metallicity, $[\text{Fe}/\text{H}] = -2.5$ dex, and the other with an age of 8 Gyr old and $[\text{Fe}/\text{H}] = -1.0$ dex. We chose these values to span the range of age and metallicity typically observed in Local Group dSphs, such as Sculptor. This is also the region of the age-metallicity parameter space where stellar populations exhibit extended HBs. We emulated realistic observational effects for a dust free stellar system at a distance of 100 kpc, using the photometric errors and the artificial star tests of the Sculptor dSph CTIO observations, presented in § 3.4. We made these tests for a fixed mass loss law, taken from Origlia et al. (2014). The resultant CMDs are shown, as Hess maps, in Fig. 3.2 and Fig. 3.3, and the recovered SFHs are shown in Fig. 3.4

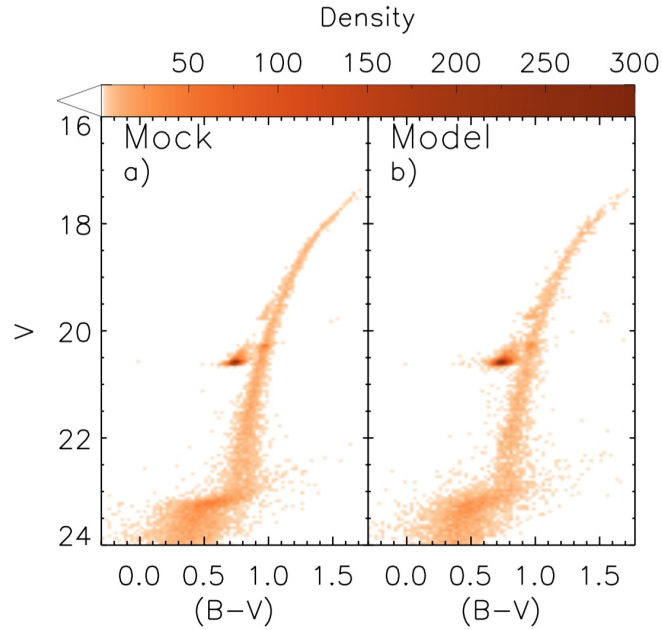


Figure 3.3: Same as Fig. 3.2 but for our younger and metal richer SSP ($t = 8$ Gyr, $[\text{Fe}/\text{H}] = -1.0$ dex.)

We first determined the SFH without the HB, as done by TALOS and similar methods. The recovered SFHs are well fit by a Gaussian function with standard deviation of 700 Myr, for the young population, and 1.3 Gyr, for the old population. These values are in line with what found by other studies (e.g., Hidalgo et al., 2011; de Boer et al., 2012).

When adding the HB to the SFH care has to be taken to balance the HB and the MSTO contributions in the final likelihood function to determine the best overall solution. If this is not done then the high number of MSTO stars tends to dominate the Poissonian likelihood determination, which can weaken the impact of the HB. Namely, when there is a difference between the SFH that best fits the MSTO and the one that best fits the HB then, without any intervention in the process, small improvements in the quality of the MSTO fit will be preferred to big improvements in the quality of the HB fit. Such differences can easily arise because of numerous observational or numerical effects, such as the imperfect characterisation of the photometric uncertainties, the discrete binning of the CMD and of the parameter space, uncertainties in the modelling parameters, statistical effects linked to the finite number of stars modelled in the stellar population or uncertainties in the stellar evolution models. To compensate for this, we

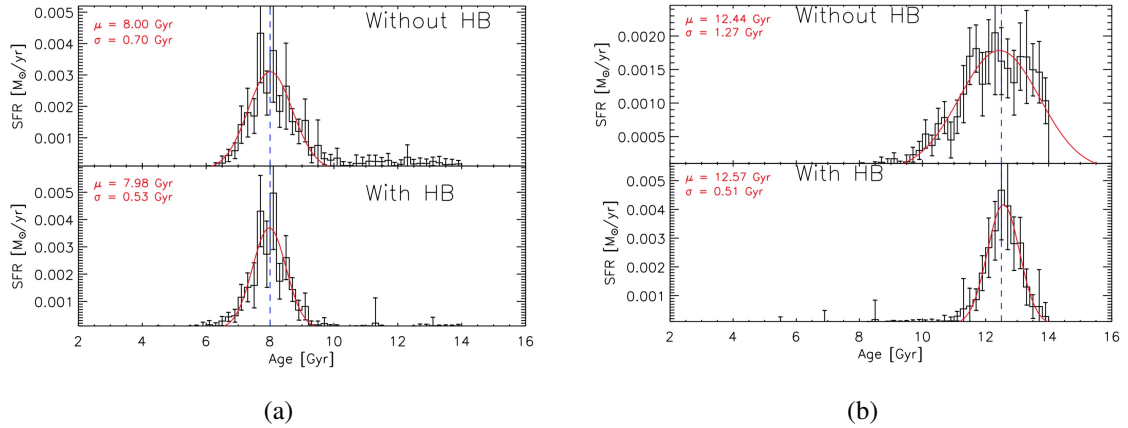


Figure 3.4: The comparison between the SFHs recovered with and without the HB modelling. The red solid lines are the Gaussian functions that best fit the SFHs. The blue dashed lines mark the true age of the stellar populations. *a)* Solutions for the young metal rich SSP. *b)* Solutions for the old metal poor SSP.

apply a scaling factor to the likelihood in the HB region. The relatively few stars here add important constraints on the age and metallicity of the stellar populations at the oldest times. For this reason, we scale the likelihood coming from the Hess bins of the HB region by the ratio of HB stars to non-HB stars, in a similar fashion to what is done with the spectroscopic MDFs by TALOS. This weighting gives a more balanced importance to both the HB and MSTO regions.

Fig. 3.4 shows that the inclusion of the HB leads to an improvement in the precision of the recovered SFHs, which now have a standard deviation of 500 Myr, compared to the modelling without the HB. This improvement is mild for the younger population (Fig. 3.4a), where the bright MSTO stars allow a fairly precise SFH. However, for the older population (Fig. 3.4b), the MSTO is fainter and characterized by a slower morphology evolution with age. In this case, the inclusion of the HB, whose morphology is very sensitive to stellar mass, significantly improves the age measurement, increasing the precision by a factor of ~ 2.5 .

Obviously, these experiments with synthetic data represent an ideal situation and give us the maximum theoretical precision that this approach can reach. In reality, any discrepancy between the synthetic models and a real galaxy, such as distance, reddening or stellar evolutionary track mismatches or uncertainties, will degrade our model-data

comparison.

Among these systematics, a major role is played by mass loss, which was assumed to be known in our modelling. Any mismatch between the predicted and true mass loss will bias the age determination of the stellar population, because of the degeneracy of these two parameters on the HB. The importance of this effect is given by the derivative of the RGB tip mass over time, at a given age. For a 12.5 Gyr old population this amounts to $\sim 0.02 M_{\odot} \text{Gyr}^{-1}$, with a slight dependency on metallicity, while for a 8 Gyr old population it is $\sim 0.04 M_{\odot} \text{Gyr}^{-1}$. This translates to an effect on the SFH of 500 Myr and 250 Myr, respectively, for each $0.01 M_{\odot}$ of difference in the mass loss.

3.3.2 Moving beyond single age synthetic models

The simple stellar population tests we performed confirm the potential of HB morphology to add additional independent constraints to standard SFH analysis and significantly improve age resolution at old times. A clear limitation of our simple stellar population experiments is the assumption that the RGB mass loss is known. Another shortcoming is the very simple SFH adopted. Real galaxies will typically have much more complex SFHs, spanning a range of age and metallicity, reflected in the morphology of their CMDs.

To address both these issues we carried out additional experiments with synthetic data to simulate more realistic conditions. We created synthetic CMDs for two galaxies with different SFHs. We used the same observational conditions as in § 3.3.1 (distance, photometric uncertainties, completeness, etc.). We then run MORGOTH to recover the SFH, as well as the RGB mass loss, for which no assumption was made, except a linear dependence on $[\text{Fe}/\text{H}]$.

In the first experiment we simulate a galaxy with two short bursts of star formation, separated by ~ 4 Gyr in age and ~ 0.7 dex in metallicity. The mock CMD of this galaxy is shown in Fig. 3.5a. Fig. 3.5b shows our best fit CMD. It can be seen that our best fit is a realistic representation of the observed CMD, also for the HB morphology.

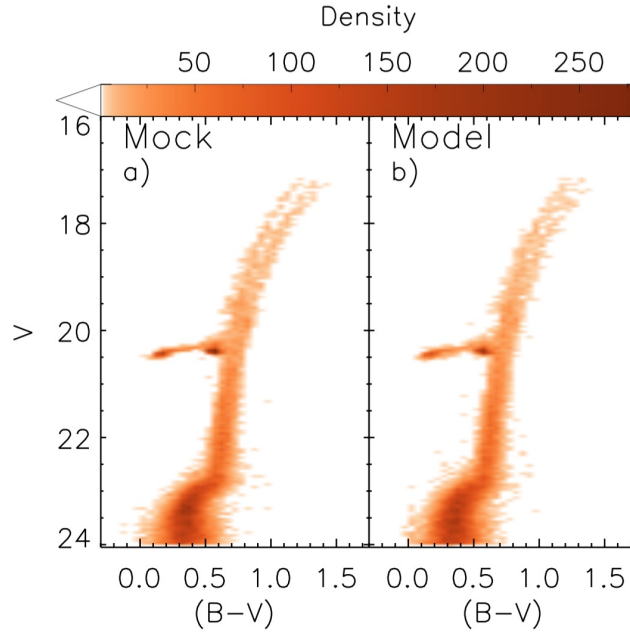


Figure 3.5: *a)* the mock $(B - V)$ vs V Hess diagram of our galaxy with a bursty SFH. *b)* The best fit Hess diagram recovered with MORGOOTH.

The four panels of Fig. 3.6, show the original inputs of our mock galaxy, along with the recovered results. As a reference, we also fit the SFH in the classical way, i.e., excluding the HB. As for the CMD, the recovered SFH is similar to the original input. In particular, the comparison with the reference solution demonstrates that the inclusion of the HB modelling helps to improve separating and characterising these two bursts of star formation, both in age and metallicity. Fig. 3.6b shows the mass loss relation that we recover, compared to that used as input. The simultaneous modelling of the HB and the MSTO region efficiently recovers the RGB mass loss prescription, within one sigma of the original.

We perform the same experiment on a second mock CMD (Fig. 3.7a), built using a constant star formation rate and a steady metallicity evolution (Fig. 3.8a). Again, the solutions we recover with and without the HB modelling, shown in Fig 3.8, prove that including the HB provides more realistic star formation rates, both as a function of age and metallicity. The HB morphology is well reconstructed, as demonstrated by the RGB mass loss inferred to be so closely matching the input.

These additional tests show that MORGOOTH is able to efficiently reconstruct the HB

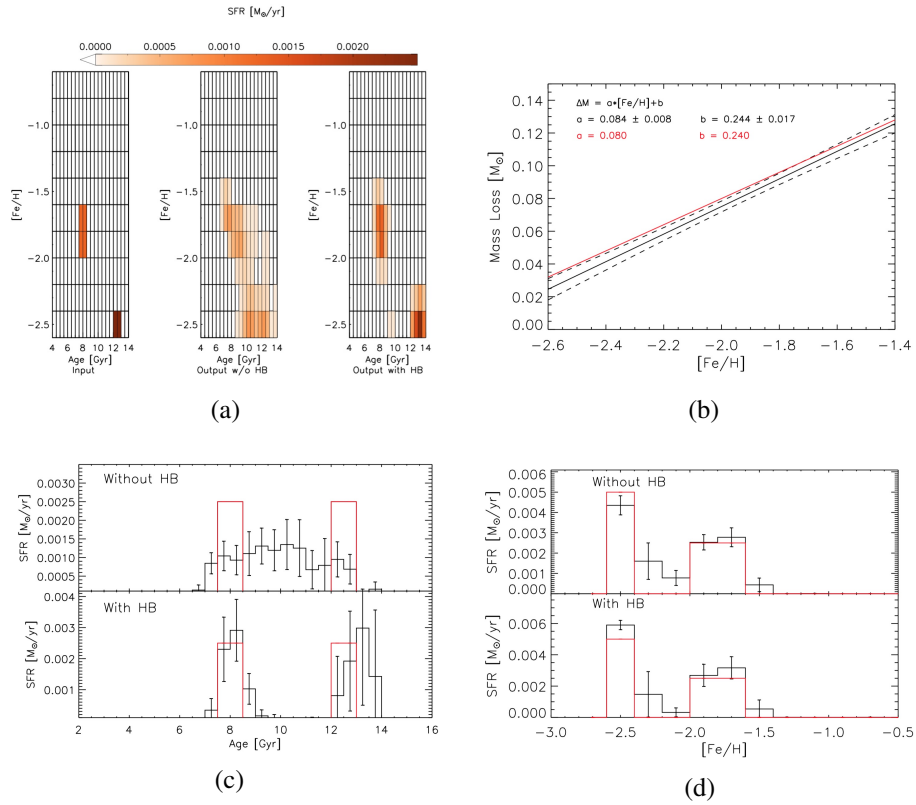


Figure 3.6: The best fit solutions for our bursty galaxy, compared with the real values. *a)* The SFH in the age-metallicity plane. The three panels are for our input SFH, the one recovered with excluding the HB and the one recovered modelling also the HB (left, centre, right, respectively). *b)* The recovered RGB mass loss as a function of metallicity (black solid line). The red solid line is the input mass loss prescription. The dotted black lines delimit the $1\text{-}\sigma$ confidence region of our solution. *c)* The star formation rate as a function of time, recovered with and without the HB modelling. The red solid lines represent the input values. *d)* The star formation rate as a function of metallicity, recovered with and without the HB modelling. The red solid lines represent the input values.

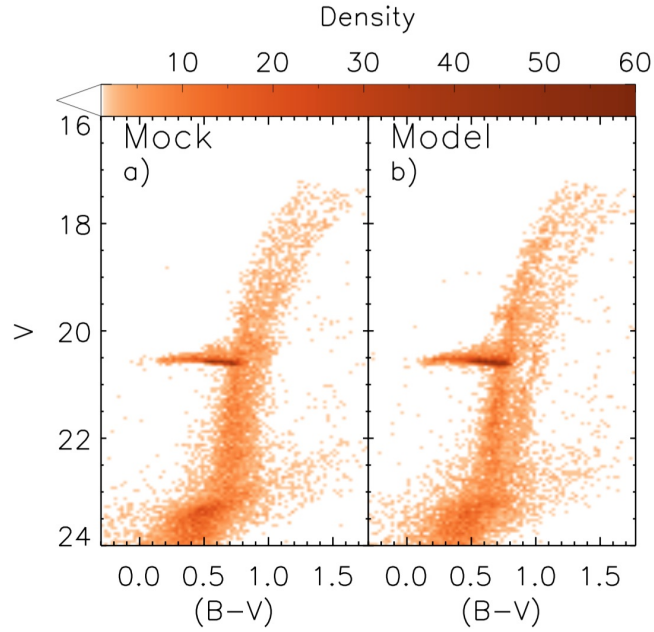


Figure 3.7: *a)* the mock $(B - V)$ vs V Hess diagram of our galaxy with a continuous SFH. *b)* The best fit Hess diagram recovered with MORGOth.

morphology when modelling stellar systems with extended SFHs, even when the RGB mass loss is an unknown and is included in the fitting. Furthermore, the improved accuracy given by the HB constraints is also present in the fit of more complex SFHs. This is clearly visible in the three panels of Fig. 3.6a and Fig. 3.8a, where the SFHs recovered with the aid of the HB are obviously improved, compared to those recovered without the HB.

3.4 The Sculptor dwarf spheroidal

Having successfully shown the effectiveness of our method on synthetic stellar populations, we move to real data and model the resolved population of the well studied Sculptor dSph. This is a close stellar system with a relatively simple SFH, as shown by the detailed SFH from de Boer et al. (2012), using TALOS. The SFH from de Boer et al. (2012) has also been used as a starting point by Salaris et al. (2013), to estimate the RGB mass loss of Sculptor. This means that both the end products of our analysis, the SFH and the RGB mass loss, have already been measured for this galaxy. As TA-

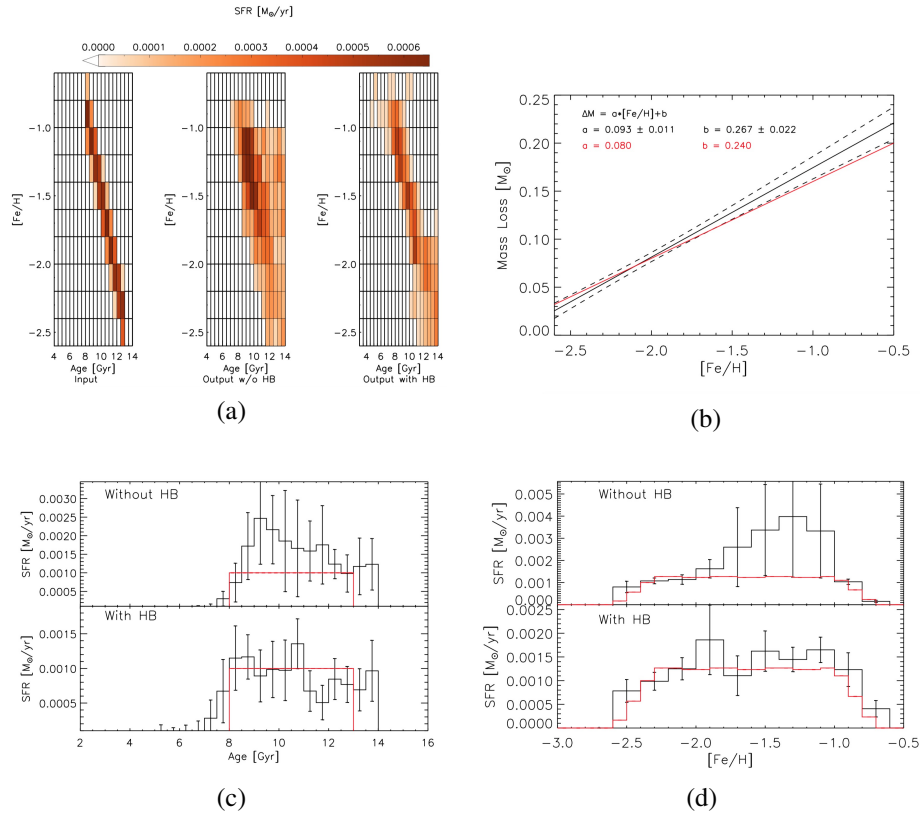


Figure 3.8: The best fit solutions for our galaxy with continuous SFH, compared with the real values. *a)* The SFH in the age-metallicity plane. The three panels are for our input SFH, the one recovered with excluding the HB and the one recovered modelling also the HB (left, centre, right, respectively). *b)* The recovered RGB mass loss as a function of metallicity (black solid line). The red solid line is the input mass loss prescription. The dotted black lines delimit the 1- σ confidence region of our solution. *c)* The star formation rate as a function of time, recovered with and without the HB modelling. The red solid lines represent the input values. *d)* The star formation rate as a function of metallicity, recovered with and without the HB modelling. The red solid lines represent the input values.

LOS is the code from which we developed MORGOTH, this galaxy will provide a very instructive comparison to evaluate the effect of adding constraints from the HB.

To model the CMD of Sculptor, we use the MOSAIC, CTIO 4m photometry from de Boer et al. (2011). We limit the analysis to an elliptical area in the centre of the galaxy, with an equivalent radius of 11 arcmin. This is the same region for which estimates were made of the RGB mass loss by Salaris et al. (2013).

For our analysis, we also have to account for the presence of RR Lyrae variables. When observed only in one or few epochs, these variable stars will have a wide distribution in magnitude and colour, because they are in different phases of their pulsation cycle, thus

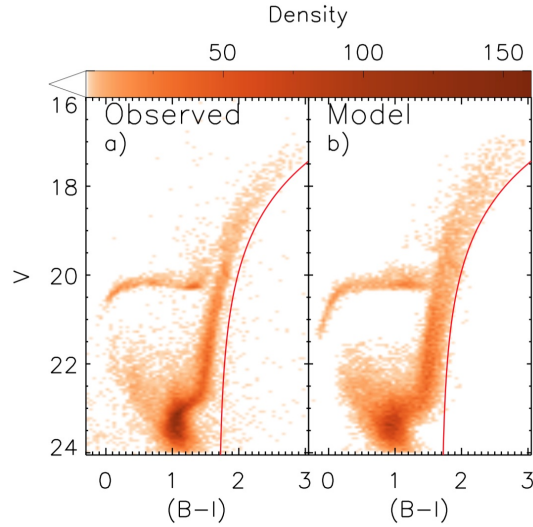


Figure 3.9: *a)* V vs $(B-I)$ Hess map of the Sculptor dSph. The photometric catalogue is taken from de Boer et al. (2011) and it has been corrected for RR Lyrae variability. *b)* Best fit Hess diagram obtained with MORGOTh. The red solid lines mark the punishment region for RGB models.

changing the HB morphology. To model the HB of Sculptor, we need to know the mean magnitude of its RR Lyrae, so that we can reconstruct the original HB morphology in the instability strip. To do that, we cross-correlated our photometric catalogue with the sample of variables from Martínez-Vázquez et al. (2016). In this way, we identify most of the RR Lyrae and substitute their observed magnitudes with their intensity averaged magnitudes. The final photometric sample we obtain is shown, as a Hess map, in Fig. 3.9.

We model the V vs $(B-I)$ CMD of Sculptor, with a fine bin size (0.05 mags) to take advantage of the detailed structure of the HB. We chose this filter combination to maximize the colour extension on the HB. The model populations we use sample the age-metallicity parameter space with a step of 0.5 Gyr and 0.2 dex. Our synthetic populations follow a Kroupa IMF (Kroupa, 2001) and $[\alpha/\text{Fe}]$ measured by high-resolution spectroscopy (Battaglia et al., 2008; Tolstoy et al., 2009). We model the observational effects using both photometric errors and artificial star tests from de Boer et al. (2011, 2012). Finally, we adopt a distance modulus of $(m - M)_0 = 19.67$ and a value of $E(B - V) = 0.018$, as in de Boer et al. (2012).

As we are now modelling the whole CMD, in contrast to de Boer et al. (2012), we also

include the full extent of the RGB. This evolutionary phase is very prominent in the CMD of an old stellar population but it has a relatively low stellar density. This means that it is inherently penalised in our Poisson statistics based modelling approach. A simple way to exploit the information on the RGB would be to also apply a weight to this part of the CMD, as we did with the HB. However, the detailed morphology of the RGB, especially its colour, is quite sensitive to a number of uncertain stellar model ingredients, such as the treatment of convection, the boundary conditions of the stellar model and the bolometric corrections of the cool stellar atmospheres. This means that applying a weight to the RGB would make our fit sensitive to these uncertainties. We resolve the issue by creating a punishment region in our CMD, as shown in Fig. 3.9. Every stellar model that falls on the red side of the line is heavily penalised in our fit. In this way we take advantage of the general morphology of the RGB without being strongly affected by the theoretical uncertainties of the RGB colour.

Our best fit CMD is shown in Fig. 3.9. The resemblance to the observations is, generally, satisfactory. There are, however, some differences in the details. We note that the MSTO and the subgiant branch are wider in our model than in the observed CMD, the model RGB has a slightly redder edge and there is a tail of blue HB stars in the model CMD that is not in the observed CMD. The origin of these problems is likely to be in the characterization of the faint CMD. Similar difficulties in reproducing the detailed structure of the main sequence region were also present in the original analysis of de Boer et al. (2012). The modelling of these faint stars is particularly sensitive to a reliable characterisation of observational conditions. As the available photometry reaches only one magnitude below the MSTO, an accurate estimate of all the uncertainties in this low signal-to-noise region can prove difficult. This problem highlights how crucial it is to have deep and well characterized dataset when modelling the resolved stellar populations in galaxies and how useful the information on the HB can be when such deep photometry is not available. In spite of these difficulties, and of the inclusion of additional constraints coming from the HB modelling, MORGOTH produced a best-fit model that is in line with what we know about the Sculptor dSph.

Looking at the best fit SFH (Fig. 3.10), we find that Sculptor's stellar population is

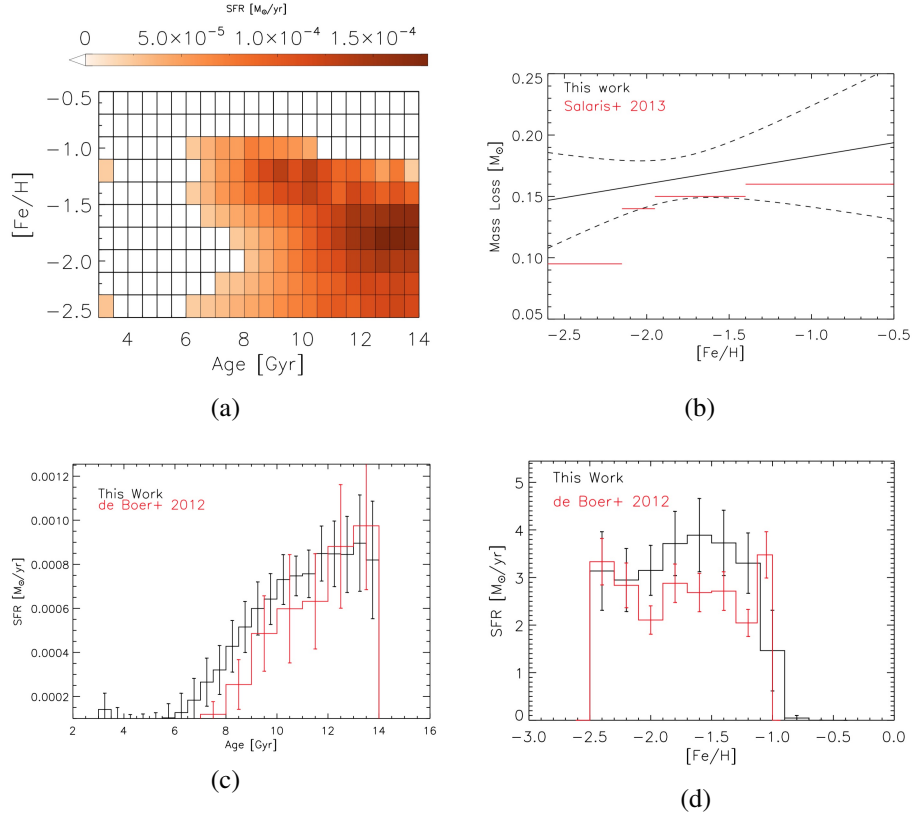


Figure 3.10: *a)* The age-metallicity distribution of star formation for Sculptor, recovered with MORGOTh. *b)* The inferred RGB mass loss (black solid line). The dotted black lines mark the $1-\sigma$ uncertainties of our estimate. The red solid line shows the results from Salaris et al. (2013). *c)* Star formation rate as a function of cosmic time. The red histogram shows the solution of de Boer et al. (2012). *d)* Star formation rate as a function of metallicity.

predominantly old and metal poor, as found by de Boer et al. (2012) and others before him. The star formation rates in the age-metallicity plane show a general evolution of the metal content with time, increasing by approximately one order of magnitude over the SFH of the galaxy. A closer look suggests the presence of two main subpopulations in Sculptor. The first one spans a range in age and metallicity of $11 \text{ Gyr} < t < 14 \text{ Gyr}$ and $-2.0 < [Fe/H] < -1.5$. The second subpopulations has $8 \text{ Gyr} < t < 11 \text{ Gyr}$ and $-1.5 < [Fe/H] < -1.0$. The presence of these two components has already been noted using the spatial distribution of the HB morphology, the metallicity and velocity dispersion distributions on the RGB (Tolstoy et al., 2004; Zhu et al., 2016). Integrating our SFH in age and metallicity (adopting a Kroupa IMF) results in a total stellar mass, within an equivalent radius of 11 arcmin, of $4.67 \pm 0.43 \cdot 10^6 M_{\odot}$.

The detailed comparison with de Boer et al. (2012) results is generally good, both in the

age and metallicity distributions of the SFH. A further confirmation of the higher precision of our method is that, although our age bins are half the size of that used in de Boer et al. (2012), our uncertainties are noticeably smaller. Note that the uncertainties are expected to increase when reducing the parameter space bin size (Dolphin, 2002). Our solution presents a more prominent tail of star formation at younger age. This is because de Boer et al. (2012) masked the blue plume of stars above the MSTO, assuming them to be blue stragglers and thus unrelated to the SFH. Determining whether or not these stars come from a genuine recent star formation event or are blue stragglers is not easy and is beyond our analysis here.

A comparison with the previous RGB mass loss rate determination is also encouraging. The amount of mass loss inferred from our analysis is, overall, a few hundreds of solar mass higher than that measured by Salaris et al. (2013), but the two estimates are in good agreement within their uncertainties. The only significant discrepancy emerges at low metallicity, where we estimate a significantly higher mass loss. This high value regards stars with $[\text{Fe}/\text{H}] \lesssim -2.0$, which cause the blue HB tail in the model CMD. A possible explanation is that this difference comes from our imposition of a linear relation between integrated mass loss and metallicity. The estimate from Salaris et al. (2013) shows a clear drop in the efficiency of mass loss for metal poor stars, greater than what would be expected by linearly extrapolating the values measured for more metal rich stars.

This discrepancy may indicate that our mass loss parametrisation is too simplistic. A higher order polynomial or a non-parametric representation (similar to Salaris et al., 2013) could lead to a more accurate model. We stress, however, that increasing the number of degrees of freedom in our HB models is also likely to make the analysis more susceptible to degeneracies, and to lead to unrealistic solutions. Clearly, the optimal strategy to treat mass loss needs to be evaluated with care. The precise choice of mass loss parametrization, however, is not critical to the conceptual validity of our method.

3.5 Conclusions

We have presented and tested MORGOTH, to show it is capable of accurately determining the SFH of both simple and complex stellar populations by quantitatively taking into account all the major luminous features of the CMD, including the HB. It takes advantage of the internal structural similarities in evolved low mass stars, to model the helium burning phase of old populations in a flexible and computationally affordable manner. Simple tests with mock stellar populations reveal the benefit of having independent constraints on age and metallicity at the old ages, from the HB, increasing the time resolution of classical SFH determinations. Even with no constraints on the mass loss efficiency, our method is capable of a substantial improvement in the SFH precision, at the same as time measuring the total mass lost by RGB stars.

We also tested our method on observations of the Sculptor dSph. The SFH and mass loss estimates obtained are in good agreement with previous analyses (de Boer et al., 2012; Salaris et al., 2013), confirming the reliability of our approach. Our SFH measurements, including the HB, have smaller uncertainties compared with traditional, MSTO only, analysis techniques, and allow us to distinguish the two stellar subpopulations known to exist in Sculptor with greater accuracy than previous CMD analyses.

The detailed modelling of the HB of resolved stellar populations in galaxies opens interesting prospects for more distant surveys. Aside from the obvious advantage of having more accurate SFH measurements thanks to the additional age and metallicity indicators, we now also have the means to measure the amount of mass lost by RGB stars in external galaxies. Understanding RGB mass loss has been a stubborn long-standing problem. In spite of decades of effort, a reliable characterization of this phenomenon has been difficult, even in apparently simpler systems like the Galactic globular clusters (e.g., Catelan, 2009). The origin of this challenge lies in the nature of globular clusters, that are now known to contain a series of chemical peculiarities also reflected in their HB morphology (e.g., Gratton et al., 2011). Dwarf galaxies, on the other hand, seem to be free from these chemical anomalies (Geisler et al., 2007; Fabrizio et al., 2015; Salaris et al., 2013; Savino et al., 2015), but the intrinsic spreads

in the age and metallicity of their stellar populations has made the study of RGB mass loss equally difficult. Developing a method to study this phenomenon in complex stellar populations is, therefore, an important step towards a more complete understanding of both stellar and galactic evolution.

Additionally, a deeper knowledge of mass loss will allow us to obtain detailed SFHs, back to the earliest times, for a much larger number of galaxies. With current analysis techniques, accurate SFHs for the earliest stages of galaxy formation can only be measured if the faintest MSTOs are detected. This limits the maximum distance for this kind of study to the edge of the Local Group. If motivated assumptions can be made about the RGB mass loss, our method has the potential to measure the SFH from the HB alone, which is brighter than equivalent age MSTOs. Deep Hubble Space Telescope observations can already resolve the HB in galaxies outside the Local Group (e.g., Da Costa et al., 2010; Lianou et al., 2013). Next generation facilities, such as the James Webb Space Telescope, the European Extremely Large Telescope and the Thirty Meter Telescope, will be able to resolve HB stars for hundreds of galaxies within several Mpc from the Milky Way (Brown et al., 2008; Greggio et al., 2012; Fiorentino et al., 2017), thus allowing accurate SFHs, back to the earliest times, for a large and diverse sample of resolved stellar systems, covering a range of environments, and over a cosmologically representative volume.

Chapter 4

Revisiting the multiple events of star formation of the Tucana dSph

This Chapter is ready to be submitted.

4.1 Introduction

The formation and evolution of dwarf galaxies represents one of the central testing grounds for many branches of extragalactic astronomy. Given the hierarchical mass assembly predicted by cold dark matter paradigms (e.g., White & Rees, 1978), understanding the processes that shape these low mass objects, not only is important to validate cosmological models, but has broad implications for the evolution of larger galaxies as well.

Resolved stellar populations provide a valuable tool to peer into the past of stellar systems. The colour-magnitude diagrams (CMDs), combined with spectroscopy, gives us the opportunity to reconstruct very detailed star formation histories (SFHs) for our closest neighbours, as well as to probe their chemical enrichment and internal dynamics (see Tolstoy et al., 2009, and references therein). While the Local Group is home to only three massive galaxies, smaller systems are much more numerous, allowing

comparative studies for a substantial sample of galaxies.

One of the discoveries coming from the observations of Local Group dwarfs is that even very simple systems such as the dwarf spheroidal galaxies (dSphs) host complex populations of stars, that differ in metallicity, kinematics and spatial distribution. Aside from the very complex stellar populations of galaxies like Carina and Fornax (e.g., Smecker-Hane et al., 1994; Beauchamp et al., 1995; Stetson et al., 1998), this feature has been detected also in simpler dSphs, such as Sculptor and Sextans (e.g., Majewski et al., 1999; Bellazzini et al., 2001; Tolstoy et al., 2004) and seems to be common in low mass galaxies. While several explanations have been put forward to explain this phenomenon (e.g., Salvadori et al., 2008; Revaz et al., 2009; Pasetto et al., 2011; Amorisco & Evans, 2012a; del Pino et al., 2015), the origin of these complexities is still debated. Clearly, an understanding of the processes that leave this imprint in the stellar population of dwarf galaxies would be a significant step forward to explain galactic formation and evolution.

Among the many ancient stellar systems that are part of the Local Group, of particular interest is the Tucana dSph. Similarly to other nearby dSphs, Tucana has been found to host distinct stellar components (e.g., Bernard et al., 2008; Monelli et al., 2010). Unlike most of the Local Group dSphs, which are satellites of M31 and the Milky Way, Tucana currently resides at the periphery of the Local Group and it is much more isolated (Tucana's distance from the Milky Way is ~ 890 kpc, Bernard et al., 2009). This means that this galaxy has spent at least several Gyrs away from the environmental disturbance of a large galaxy, potentially preserving a much more pristine imprint of the conditions in which this galaxy formed.

However, the distance to this galaxy is also a complication when it comes to the observational characterisation. With current observing facilities, medium-resolution spectroscopy is only feasible for the few brightest giants of Tucana, and high-resolution studies, fundamental to study the abundance of different chemical species, are prohibitive. Photometric studies, while more viable, require depth achievable only with cutting-edge facilities, in order to reach the faintest stars. Such observations have been obtained for Tucana using the Hubble Space Telescope (HST) as part of the LCID

project (Monelli et al., 2010). Nonetheless, the information that can be extracted with photometry alone is limited, and it is often sensitive to strong degeneracies.

In this study, we take advantage of a new modelling method (Savino et al., submitted), to model the CMD of Tucana with higher precision. This approach makes use of the simultaneous modelling of all the CMD features observed in the CMD, to measure the SFH with improved resolution. Making quantitative models of the HB, we obtain a detailed measurement of the early star formation in this galaxy. In § 4.2 we describe the dataset and the modelling approach, in § 4.3 we present and discuss the SFH, while in § 4.4 we summarise our results.

4.2 Modelling the colour-magnitude diagram

The photometric data we use in this analysis have been acquired with the ACS camera, on board of the HST, as part of the LCID project ¹ and have been presented in Monelli et al. (2010). The dataset consists of deep exposures in the $F475W$ and $F814W$ passbands, covering a field of view of $\sim 3'.4 \times \sim 3'.4$ (for reference, the tidal radius of Tucana is $\sim 3'.7$). We complement these data with the catalogue of RR Lyrae from Bernard et al. (2009), derived from the same observations. We cross-matched the positions of the detected RR Lyrae with the photometric catalogue, substituting to their observed magnitudes their intensity-averaged magnitudes. As this quantity is very close to the “static” magnitude that these stars would have if they were not pulsating (Bono et al., 1995), we are able to reconstruct the original morphology of the HB.

The resultant ($F475W - F814W$) vs $F814W$ CMD is shown in Fig. 4.1, where the superb quality of HST photometry can be appreciated. Despite the distance of this galaxy, stars are resolved to ~ 1.5 magnitudes below the oldest MSTO. Among the features that can easily be identified, we note a prominent HB and a plume of blue, bright stars emerging from the MSTO. The HB has a complex structure. This was noted already by Harbeck et al. (2001), but it can be better appreciated with the increased

¹<http://www.iac.es/project/LCID/>

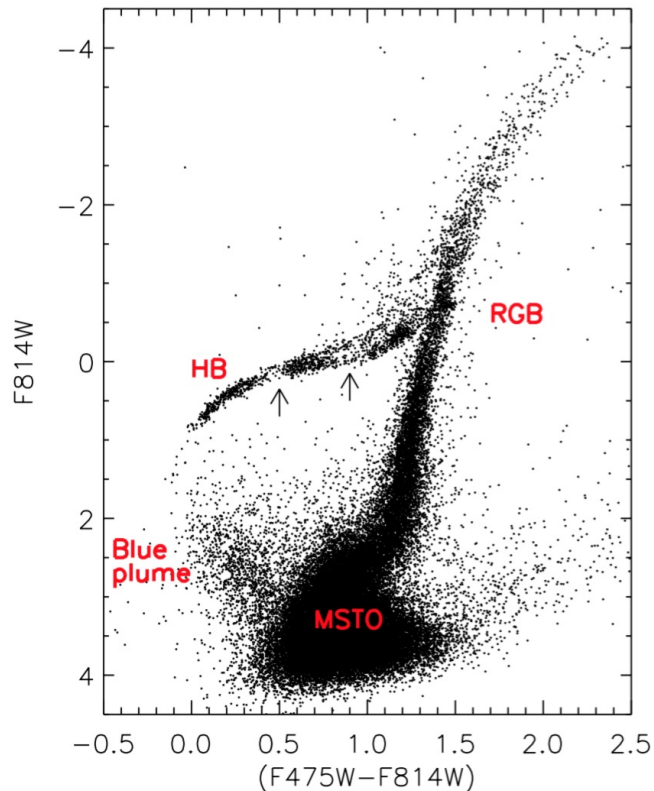


Figure 4.1: The HST CMD of the Tucana dSph, from Monelli et al. (2010). The morphology of the HB is corrected for RR Lyrae variability. The major CMD features are indicated. The arrows mark the position of the HB gaps.

photometric precision of this dataset. The distribution of stars across the HB is not uniform, but has three distinct clumps of stars. These are separated by lower stellar density gaps, at $(F475W - F814W) \sim 0.5$ and $(F475W - F814W) \sim 0.9$.

We model the CMD using MORGOTH (Savino et al., submitted). MORGOTH is a SFH recovery method that models all the evolutionary phases up to the beginning of the thermally pulsing asymptotic giant branch. As the morphology of the HB is strongly dependent on the RGB mass loss, this quantity is left as a free parameter and is measured along with the SFH. The total amount of mass lost on the RGB is assumed to have a linear dependence on the metallicity only. The procedure MORGOTH uses to treat the HB model generation ensures that the SFH and the mass loss measurements are always physically self-consistent. See Savino et al. (submitted, chapter 3) for more details about the method.

To generate synthetic CMD models we need several ingredients. To model the CMD

up to the tip of the RGB we use BaSTI isochrones (Pietrinferni et al., 2004, 2006). These are complemented by a grid of theoretical HB tracks, from the same group, covering a mass range of $0.5 - 1.5 M_{\odot}$. This ensures that we are able to model even the reddest and most massive HB stars of Tucana, as well as the progeny of the blue straggler population. We generate the synthetic models using a Kroupa initial mass function (Kroupa, 2001) and a binary fraction of 0.4, as done in Monelli et al. (2010). The models are calculated covering ages from 1 to 14 Gyr, with a bins size of 0.5 Gyr, and values of $[Fe/H]$ from -2.6 to -0.6 , with a bin size of 0.2 dex. The CMD are transformed into Hess diagrams with a bin size of 0.05 mags in both colour and magnitude. We exclude the faintest 0.5 magnitudes from the fit, to avoid problems related to the lowest stellar mass in our models ($0.5 M_{\odot}$). We adopt a distance modulus $(m - M)_0 = 24.74$ and an extinction $A_V = 0.094$ (Bernard et al., 2009).

Due to the distance of Tucana, no direct measurements have been possible to determine the detailed chemical properties of its stars. For old populations, stars with the same global abundance $[M/H]$, but different values of $[\alpha/Fe]$, will have very similar stellar structures (Salaris et al., 1993). However, the opacity of the stellar atmosphere is much more sensitive to the chemical pattern (Cassisi et al., 2004), especially in the blue region of the spectrum, thus affecting the observed magnitudes and colours. It is thus important to make a realistic assumption about the alpha enhancement profile of Tucana. We assume the oldest stars to be alpha enhanced, as observed in the Milky Way halo and in many old stellar systems. However, younger and more metal rich stars, are likely to have a scaled-solar mixture or even be alpha depleted (Tolstoy et al., 2009). The metallicity at which $[\alpha/Fe]$ starts to decrease and the slope depend on the chemical enrichment history of the galaxy, and they are difficult to predict. For our modelling we assume the $[\alpha/Fe]$ vs $[Fe/H]$ profile of the Sculptor dSph, which has similar properties to Tucana and reliable spectroscopic measurements (Battaglia et al., 2008; Tolstoy et al., 2009). We assume all stars with $[Fe/H] < -1.84$ to have $[\alpha/Fe] = 0.4$. For higher $[Fe/H]$, the alpha enhancement decreases with $\frac{d[\alpha/Fe]}{d[Fe/H]} = -0.64$. In section 4.3 we discuss the impact of adopting a different alpha enhancement profile.

Finally, we need to model photometric uncertainties and incompleteness. This is done

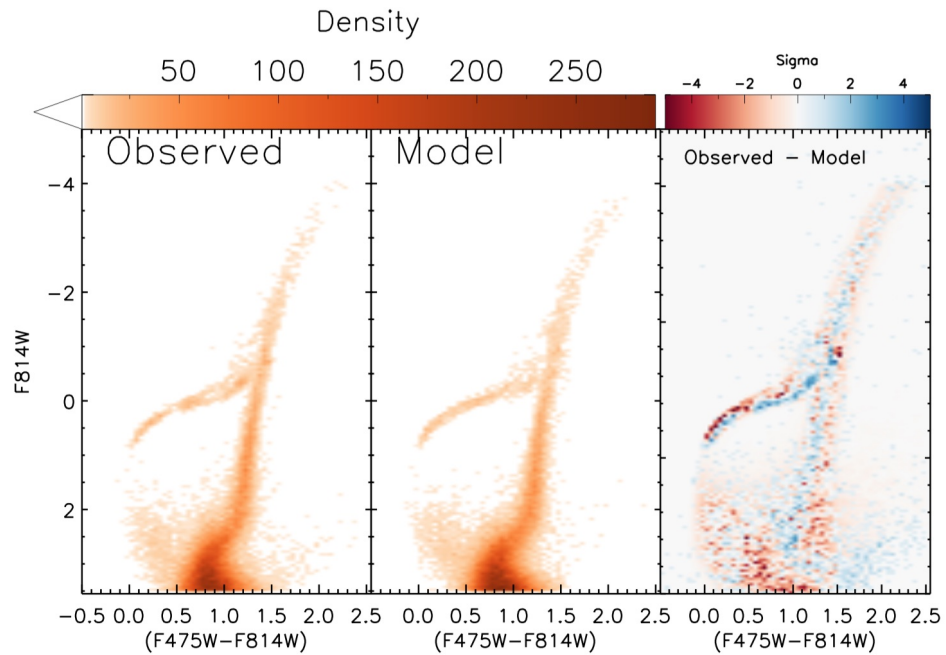


Figure 4.2: Observed (left) and best-fit (centre) Hess diagrams for Tucana, colour coded by stellar density. The right panel shows the stellar count residuals, expressed in terms of the Poisson error.

by means of artificial star tests. These tests tell us the photometric error distribution and the completeness level as a function of position in the CMD. We use this information to include observational effects in the synthetic CMDs. For this task, we use the artificial star results from Monelli et al. (2010).

4.3 Results and discussion

The best fit CMD of Tucana is showed in Fig. 4.2. The agreement with the observed CMD, also shown, is very good. The morphology of all the major stellar evolutionary phases are reproduced. The colour extension of the model HB matches what is observed. We note that, although our model HB is not uniformly populated, it is not as clumpy as the observed HB. This creates strong residuals on the position of the observed HB gaps. The other major difference is that we seem to slightly underpredict the stellar counts in the reddest part of the HB. We will come back to this issue later in this section.

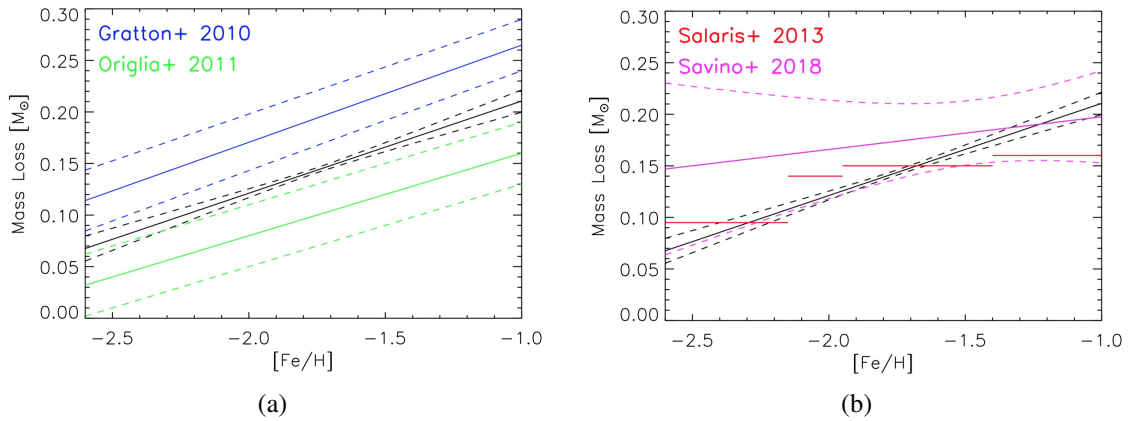


Figure 4.3: Total RGB mass loss as a function of metallicity, as measured from our modelling. The black solid line shows our measurements and the dashed black lines mark the one sigma confidence interval. a) Comparison with measurements obtained, on globular clusters, by Gratton et al. (2010) (blue) and Origlia et al. (2014) (green). b) Comparison with measurements obtained, on the Sculptor dSph, by Salaris et al. (2013) (red) and Savino et al. (submitted) (magenta).

From the CMD modelling, we find that RGB stars lose mass following the relation:

$$\Delta M_{RGB} = [Fe/H] \times (0.089 \pm 0.014) + (0.300 \pm 0.025) M_{\odot} \quad (4.1)$$

with a correlation between the slope and zero-point of the relation of 0.995. The RGB mass loss of our model is shown in Fig. 4.3, along with other measurements from the literature, derived from Galactic globular clusters and from the Sculptor dSph. In agreement with other studies, we find that stars of increasing metallicity lose more mass. Quantitatively, our measurement lies in between the results of Gratton et al. (2010) and Origlia et al. (2014), obtained from Galactic globular clusters, and it is compatible with the measurement of Salaris et al. (2013) and Savino et al. (submitted) for the Sculptor dSph. In spite of the sizeable uncertainties on the slope and zero-point of the mass loss relation, then correlation between this two quantities makes the uncertainties on the integrated RGB mass loss small. The nominal uncertainty on the total mass loss is less than $0.003M_{\odot}$ for $[Fe/H]$ between -1.9 and -1.6 , where most of Tucana’s stars are. However, the mass sampling of our HB model grid is $0.005M_{\odot}$, so this number is a more realistic lower limit for the measurement uncertainty. For stars outside this metallicity range, where we have less constraining power, the measurement

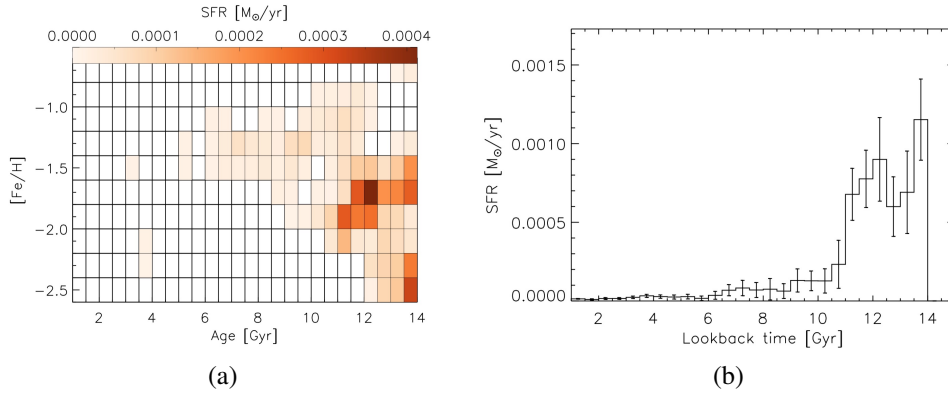


Figure 4.4: a) Best-fit SFH in the age-metallicity plane, colour coded by star formation rate. b) Corresponding star formation rate as a function of cosmic look-back time.

error is smaller than $0.015M_{\odot}$.

Fig. 4.4 shows the SFH corresponding to our best fit CMD, in the age-metallicity plane (Fig. 4.4a), and the star formation rate as a function of cosmic look-back time (Fig. 4.4b). The majority of Tucana’s stars formed more than 11 Gyr ago, in line with previous measurements (Monelli et al., 2010). However, our model contains an extended tail of star formation, persisting until 5-6 Gyr ago. We stress that this younger and more metal rich population is not caused by the blue plume above the MSTO, which is likely to have a strong blue straggler contamination, and which is found in the sparse very young and metal poor bins of our SFH. Integrating the SFH, with a Kroupa initial mass function (Kroupa, 2001), results in a stellar mass of $3.13 \pm 0.14 \cdot 10^6 M_{\odot}$ within the observed field of view.

The SFH is clearly not unimodal, but rather it is composed by three distinct star formation events. The two stronger bursts occurred very early and are separated by $\sim 1\text{Gyr}$, with the second being 0.6 dex more metal rich than the first one. The last star formation event, of lower intensity, started about 10 Gyr ago and lasted for several Gyr, with metallicities as high as $[Fe/H] = -1.0$.

The presence of three distinct events of star formation in the SFH of Tucana is correlated with the clumps observed in the stellar distribution of the HB. Fig. 4.5, shows a comparison between the observed HB of Tucana and the synthetic HB coming from our model. In the synthetic CMD we identify the stars that belong to the three distinct

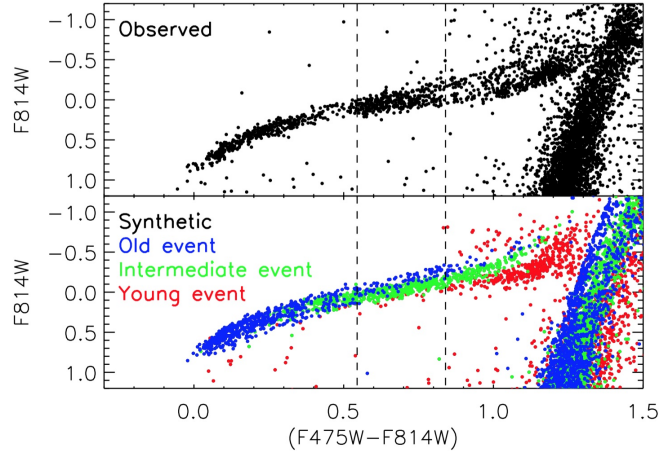


Figure 4.5: Upper panel: the observed HB of Tucana. Lower panel: the synthetic HB from our model. Stars belonging to the oldest star formation event are coloured in blue, those belonging to the intermediate event are coloured in green and stars belonging to the most recent event are coloured in red. The dashed lines mark the approximate position of the instability strip.

episodes of star formation, and colour code them accordingly. It is not surprising that there is a trend along the extension of the HB. Old and metal poor stars tend to reside on the blue end of the HB. Decreasing age and increasing the metallicity cause HB stars to have much redder colours. The age distribution of the SFH matches the position of the HB clumps. We do not fully reproduce the clear gap between the old and the intermediate clump. This happens because we are limited by resolution effects, and it means that the two older bursts of star formation have a narrower distribution in age and metallicity than predicted by our model. This limitation of our resolution is determined in part by the photometric errors. The other major discrepancy between our model HB and the observed one is that our redder HB clump is less populated than observed (Fig. 4.2). Since, the redder clump is associated with the latest star formation event, this may imply that the third star formation episode experienced by Tucana was stronger than we measure, possibly comparable with previous two.

Our modelling is not the first detection of distinct stellar populations in Tucana. Examining the luminosity function of the RGB, Monelli et al. (2010) reported the presence of two distinct RGB bumps. This was associated with the presence of two distinct stellar components, differing in metallicity. Another independent detection has been made, by the same group, looking at pulsational properties of the RR Lyrae (Bernard

et al., 2008). That study divided the RR Lyrae into a “bright” and a “faint” sample, depending on their intensity averaged magnitude, finding that the two groups defined different sequences in the pulsation period-amplitude diagram and suggesting a difference in metallicity between the two groups. The authors of these studies concluded that Tucana experienced two distinct events of star formation, very early on during its formation and separated by a short amount of time. Such explanation is confirmed by our synthetic HB. From Fig 4.5, it can be seen that stars belonging to the intermediate event enter the instability strip already on the ZAHB. Because of this, they are predominantly detected as low luminosity RR Lyrae. In contrast, stars belonging to the oldest and most metal poor event spend most of their life on the blue HB, and they cross the instability strip only when evolving towards the asymptotic giant branch. This difference in metallicity and evolutionary stage explains the higher luminosity of these stars.

The stars that formed during the final star formation event are confined in the reddest clump of the HB. These stars never cross the instability strip, and hence never become RR Lyrae. This is why no claims for a third burst of star formation in Tucana could be made by previous studies. However, the presence of stars much younger and more metal rich than previously thought is required to explain the HB morphology. Fig. 4.6 shows again the observed HB of Tucana, superimposed to a BaSTI isochrone with age of 8 Gyr and $[Fe/H] = -1.27$ and to a ZAHB of the same metallicity. The ZAHB marks the start of the helium burning phase for stars of the same metallicity but different mass, with mass increasing towards redder colours. This stellar population we chose corresponds to the youngest and most metal rich location in the age-metallicity plane, where significant star formation was thought to have happened, according to previous SFH measurements (Monelli et al., 2010). If the RGB stars of this population lose $0.19M_{\odot}$, as predicted by our model, they will start quiescent helium burning on the location marked by the blue dot. Since most of the stars on the HB clump are redder than this position, they must have higher stellar mass, i.e., they either experience a much lower amount of RGB mass loss or they come from a younger and/or more metal rich population. The most massive HB stars that can be produced by the stellar

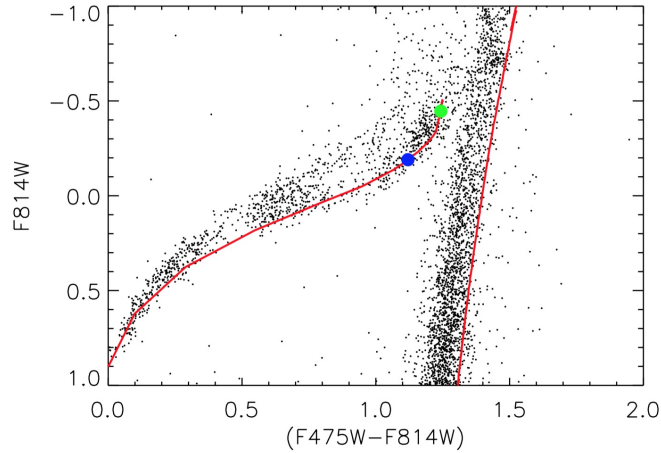


Figure 4.6: Observed HB and RGB of Tucana. A theoretical isochrone for $t=8$ Gyr and $[Fe/H] = -1.27$, and the corresponding ZAHB locus, are superimposed. The blue point marks the ZAHB position of HB stars experiencing the RGB mass loss as measured in this study. The green point marks the ZAHB location corresponding to no RGB mass loss, i.e., the maximum HB mass obtainable from this stellar population.

population displayed in Fig. 4.6, start quiescent helium burning on the location marked by the green dot. This position corresponds to no RGB mass loss. Although this location on the ZAHB is near the red end of Tucana’s HB, there are still a few redder stars, that are not compatible with assumed age and metallicity. More importantly, a null RGB mass loss is strongly unrealistic. Assuming a more reasonable mass loss value implies that most of the stars on the red HB have formed at more recent times or with higher metal content, in accordance with our measurement.

Our modelling relies on a number of measurements and assumptions to create the synthetic stellar population models. For this reason it is important to do a sanity check and verify the robustness of our results. For this reason, we repeated the SFH measurement many times, varying parameters such as distance, reddening or binary fraction. We also used different $[\alpha/Fe]$ vs $[Fe/H]$ relations, varying the knee position and the slope of the relation. We also repeated the measurement assuming all stars to have either alpha-enhanced ($[\alpha/Fe] = 0.4$) or scaled solar composition. Although these tests changed slightly the details of the SFH and of the RGB mass loss law, none of the assumed set-ups significantly altered the main result. The strongest effect on the SFH, especially when changing the $[\alpha/Fe]$ values, is the ability to resolve the two oldest bursts of star formation, which can become slightly blended together. However, the previ-

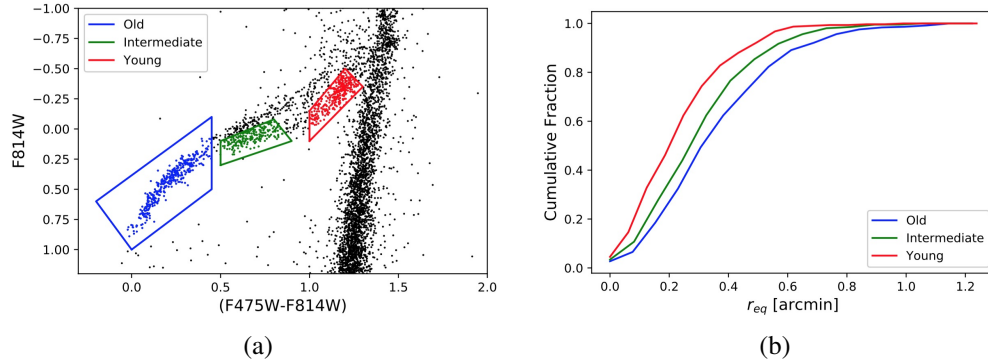


Figure 4.7: Our selection criterion to isolate the three HB clumps of Tucana. The red and green box are designed to minimize contamination from less massive stars evolving towards the AGB. b) Cumulative radial distribution of the HB stars in the three clumps.

ous detections using the RGB bump and the RR Lyrae properties, coupled with the peculiar structure of Tucana’s HB, make us confident of the existence of two different events of star formation in the early history of this galaxy. We also stress that the tail of more recent and metal rich star formation is the most resilient to systematics in the modelling parameters, and it is always present in our SFH.

As an additional piece of information, we can use the structure of the HB to trace the spatial distribution of star formation during the three events of Tucana’s SFH. The gradient in the HB morphology of Tucana was first reported by Harbeck et al. (2001) who concluded it was sign of a metallicity gradient. However, the quality of the data available at the time allowed only to a comparison between red and blue HB, with the first one sensitive to contamination from the RGB. With the high photometric precision of the dataset at our disposal, we can perform a much more precise selection, measuring the spatial distribution of HB in the three different clumps. This is shown in Fig. 4.7. The coloured boxes in Fig. 4.7a represent our selection for the old, intermediate and young age clumps. Care has to be taken when selecting stars in the intermediate and red HB clumps, as these regions are contaminated by lower mass stars that are evolving towards the asymptotic giant branch. These stars create the bifurcation seen at $(F475W - F814W) > 0.8$, and if they are not removed properly, they will soften the true radial gradient. For this reason we selected stars in the intermediate and red HB clump to minimise this contamination. Our final selection consists of 367 stars in

the blue clump, 206 in the intermediate clump and 308 stars in the red one. The radial distribution of the three clumps is shown in Fig. 4.7b. As expected, we find a spatial gradient in the distribution of HB stars, which reflects a different spatial distribution of the different events of star formation. The older the population, the more diffuse is its spatial distribution. The younger stellar population, corresponding to the red HB clump is the most centrally concentrated. Such radial segregation is statistically significant. A two-sample Kolmogorov-Smirnov test shows that the young population has a probability of $1.69 \cdot 10^{-6}$ to be drawn from the spatial distribution of the intermediate population, and a probability of $1.89 \cdot 10^{-13}$ to have the same distribution of the old population. On the other hand, the old and the intermediate stellar populations have a 4% probability to have the same radial distribution. Given the non collisional nature of stellar populations in dSphs and the isolated nature of Tucana, it is likely that these distributions reflect the original conditions in which these populations formed (or were accreted) in Tucana.

4.4 Conclusions

In this paper we carried out an accurate CMD modelling of the dwarf galaxy Tucana, that provided precise measurements for the SFH of this galaxy and for the RGB mass loss experienced by its stars.

The increased precision on the determination of the RGB mass loss provides useful constraints to theoretical models that aim to reproduce and characterise the mechanism beyond this poorly understood phenomenon. A comparison with previous measurements on the Sculptor dSph (Fig. 4.3b), shows good agreement within the uncertainties, suggesting that stars in different galaxies might experience similar amount of mass loss. Clearly, the modelling of deep CMDs from other external galaxies is required to ascertain whether a universal “mass loss law” exists for dwarf spheroidal galaxies.

The simultaneous modelling of the HB and of the MSTO revealed that the SFH of

Tucana is composed of three independent star formation events. The radial distribution of Tucana's HB stars reveals a different concentration for the different star formation events, with younger stars preferentially found in the central regions of the galaxy.

The complexity of stellar populations in dSphs, and their spatial gradients, have been long known (e.g., Harbeck et al., 2001; Bellazzini et al., 2001; Tolstoy et al., 2004). However, whether these galaxies host distinct stellar populations or a smooth gradient in age or metallicity it is still debated. Our result suggests that dSphs are composed by discrete stellar subpopulations.

The origin of these complex stellar populations is also debated. Scenarios for the formation of these galaxies include galaxy mergers (Amorisco & Evans, 2012a; del Pino et al., 2015), in situ star formation modulated by supernova feedback (Salvadori et al., 2008; Revaz et al., 2009) or tidal interaction with larger galaxies (Pasetto et al., 2011). At present, observational evidence is still unable to provide a definitive answer. Thanks to the high age resolution that our approach provides, we have, for the first time, been able to assign a precise formation time to the subpopulations of a dSph. This information complements the existing picture provided by the kinematic measurements and the chemical composition analysis of dwarf galaxies in the Local Group, representing a step forward to the solution of this problem.

Chapter 5

A Strömgren photometric analysis of the globular cluster M13.

This Chapter has been published as Savino et al. (2018).

5.1 Introduction

Once thought to be the quintessential simple stellar populations (Renzini & Buzzoni, 1986), globular clusters (GCs) have revealed a degree of complexity in their properties that is now challenging our understanding of these celestial objects.

Over the past few decades, a growing body of spectroscopic and photometric evidence has shown the presence of multiple stellar populations in nearly all the Galactic GCs (e.g. Carretta et al., 2010; Piotto et al., 2015), and also in those of nearby galaxies (e.g. Letarte et al., 2006; Mucciarelli et al., 2009; Larsen et al., 2014; Dalessandro et al., 2016). Such stellar populations are characterized by marked differences in the chemical abundance of light elemental species. A fraction of stars in GCs present a chemical abundance pattern that is compatible with that of halo stars of the same metallicity. This group of stars is called first, or primordial, population. However, a significant fraction of GC stars show enhancement or depletion of certain light elements (like C,

N, O, Na, Mg, Al), in the form of very clear correlations and anticorrelations. These stars, even when belonging to several subgroups, are collectively known as the second, or enriched, population. These light element abundance ‘anomalies’ appear to be linked to an enhancement of the helium content in the chemical mixture from which these stars originated (reviews for photometry and spectroscopy can be found in Piotto, 2009; Gratton et al., 2012).

Many theoretical models have been put forward to try to explain the multiple population phenomenon (e.g., Ventura et al., 2001; Decressin et al., 2007; de Mink et al., 2009; Bastian et al., 2013; Denissenkov & Hartwick, 2014). Most of them require the material of second population stars to be first processed by a class of objects called polluters, that are capable of sustaining high temperature CNO cycle reactions. Multiple episodes of star formation are required by some of these scenarios. The precise nature of these polluters is scenario-dependent and it remains a matter of debate. While each model is able to reproduce some of the globular cluster observed properties, each one of them has its own specific limitations (e.g., Gratton et al., 2012; Bastian et al., 2015; Renzini et al., 2015).

A crucial piece of information is thought to reside in the spatial distribution of multiple populations within a cluster. Differences in their radial distribution are expected for most scenarios where multiple star formation events are present. This prediction is complicated by the collisional nature of GCs. Over time, dynamical evolution naturally erases any difference in the initial conditions of the two populations. This effect is faster in the central regions of a cluster, where dynamical timescales are shorter. However, it has been shown by means of numerical simulations (Vesperini et al., 2013) that GCs can retain some memory of their primordial configuration, in particular in the external regions.

An ideal dataset to assess this problem would consist of chemical information for a large sample of stars over a wide field of view. While modern multi-object spectrographs have substantially increased the number of spectra, the stellar samples for which we have high-resolution elemental abundances are still too small to trace radial distributions in a reliable way.

Photometric studies, on the other hand, have the advantage to efficiently include a much higher number of stars, provided that there is a way to distinguish the different populations. Since the work of Marino et al. (2008) and Yong et al. (2008) it has become clear that appropriate combination of ultra-violet and optical photometric filters can reveal light element abundance spreads on the RGB. The most powerful tool to perform this kind of analysis is probably represented by the WFC3/UVIS camera, because it offers a filter combination covering features of C, N and O (the last not accessible from the ground – Milone et al., 2012), on board of the Hubble Space Telescope (hereafter HST). Unfortunately, the size of the HST field of view is small and rarely covers more than one half-light radius for nearby GCs. Fortunately, there are other filter combinations, involving the ultraviolet, which can be efficiently used, in particular narrow and medium-band filters (see, e.g., Lee, 2017, for a thorough study of M5 using a very effective choice of photometric filters).

In this paper we present the analysis of the multiple populations in the cluster NGC6205 (M13). M13 is a northern GC with a metallicity of $[Fe/H] \simeq -1.55$ dex (Snedden et al., 2004; Carretta et al., 2009) that exhibits strong light element variations (Snedden et al., 2004; Cohen & Meléndez, 2005; Johnson & Pilachowski, 2012). In addition, Dalesandro et al. (2013), by means of synthetic horizontal branch modeling, derived a helium spread of $\Delta Y \simeq 0.05$.

To study multiple populations of M13 we make use of Strömgren photometry, probing the cluster out to a distance of 6.5 half-light radii. The power of medium band Strömgren filters to identify globular cluster multiple populations has been firstly recognized by Yong et al. (2008). As demonstrated by Carretta et al. (2011) and Massari et al. (2016), in this analysis we exploit the efficiency of the c_y index in maximizing the effect of carbon and nitrogen abundance variations, to identify the cluster multiple populations and to investigate their spatial distribution. In § 5.2 we describe the dataset employed for this analysis, in § 5.3 we present our final photometric catalogue, while § 5.4 shows the multiple population identification and characterization. We discuss our results and conclusions in § 5.5.

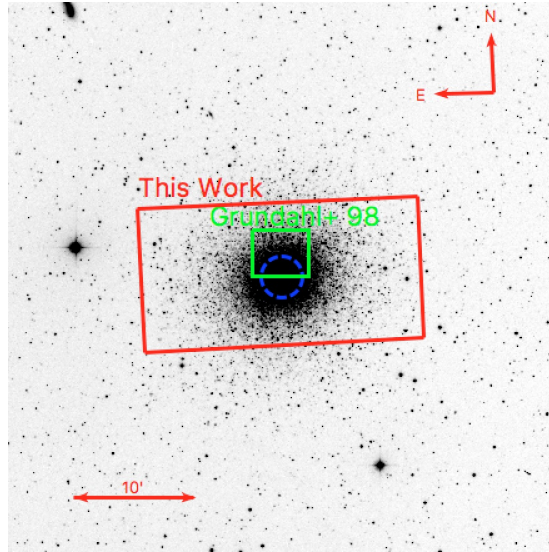


Figure 5.1: Archival image of M13 from Sloan Digital Sky Survey. The solid red box is the field of view of our dataset for WFC chip four. The solid green box is the field of view of NOT observations from Grundahl et al. (1998). The dashed blue circle marks M13 half-light radius.

5.2 Data reduction

Our primary dataset consists of archival images, acquired with the Isaac Newton Telescope - Wide Field Camera (INT-WFC). The INT-WFC has four chips, each covering a field of view of 12.1×23.1 arcmin, with a pixel scale of 0.33 arcsec. The data for this analysis come only from chip four. Using a single chip prevents any problem related to relative calibration between different detectors, allowing for more precise photometry. This choice is possible as chip four covers most of the extent of M13 (~ 6.5 half-light radii), which is sufficient for our goal. The analysed field of view is shown in Fig. 5.1.

The images have been acquired using the Strömgren *uvby* filters, and they come from different observational campaigns, covering different nights from 2004 June 19 to 2013 June 14. A summary of the employed exposures can be found in Table 5.1.

The image pre-reduction has been carried out using the IRAF package¹. For each night, we used ten biases and between five and ten flat-fields per filter. We computed 3σ clipped median biases and flat-fields using the *zerocombine* and *flatcombine* IRAF

¹IRAF is distributed by the National Optical Astronomy Observatory, which is operated by the Association of Universities for Research in Astronomy, Inc., under cooperative agreement with the National Science Foundation.

Table 5.1: Exposure times, number of frames and average seeing of our dataset.

Filter	t_{exp} s	n_{exp}	seeing arcsec
<i>u</i>	60	3	1.0
	120	4	1.2
<i>v</i>	45	2	1.1
	60	3	1.2
	120	2	1.2
<i>b</i>	30	2	1.2
	60	3	1.1
	80	2	1.4
<i>y</i>	30	2	1.2
	60	3	1.1
	80	2	1.3

tasks. These images have been used to correct the raw images by means of the *ccdproc* IRAF task.

The photometric reduction of the scientific images has been carried out using DAOPHOT and ALLSTAR (Stetson, 1987) to analyse individual exposures. For each of them, we modelled the point spread function as a Moffat function (with $\beta = 2.5$; Moffat, 1969), using 80 bright, isolated and unsaturated stars. We allowed a linear variation of the model parameters across the field of view. These models were used to build a stellar catalogue for each image. The catalogues were combined using DAOMATCH-DAOMASTER to estimate mean magnitudes and related uncertainties in each filter. Any zero-point offset caused by different exposure times was corrected by the software, which took into account every star detected in at least two exposures. This choice accounts for pointing differences, maximizing our final field of view.

Among these catalogues, the *u* filter had the highest number of detections so we used it as a reference to refine the analysis of all our images with ALLFRAME (Stetson, 1994). We then used DAOMATCH-DAOMASTER to create our final multi-band photometric catalogue. Since we want to analyse a combination of different filters, we included only those stars that were detected in all filters.

Stellar positions were transformed onto the equatorial reference by using the 2MASS

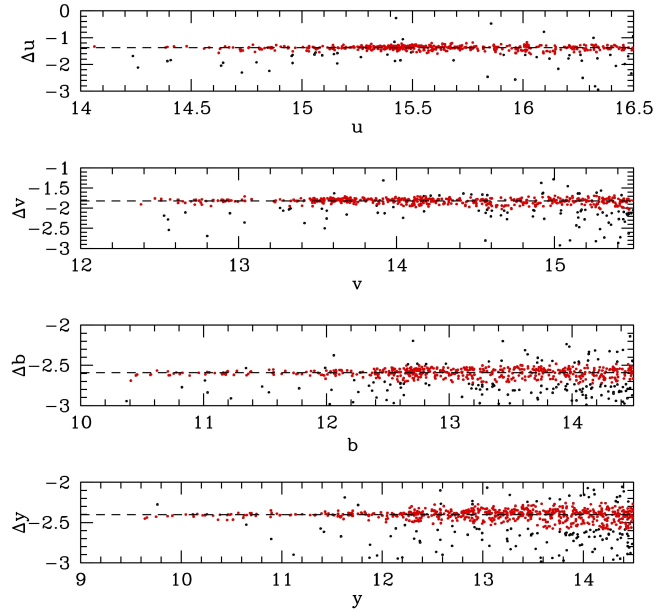


Figure 5.2: The magnitude difference as a function of magnitude for the bright stars in common between our catalogue and Grundahl et al. (1998). The four panels show the photometric filters used in this work. The red points are the stars used to calibrate the magnitudes of our dataset. The dashed black lines are the zero-point corrections estimated for our photometry.

astrometric system (Skrutskie et al., 2006). In order to do so, and for every other cross-match required by our analysis, we used the software CATAPACK², developed by P. Montegriffo. For each filter, the magnitudes have been calibrated onto the Strömgren photometric system using the M13 catalogue from Grundahl et al. (1998), made public at <http://www.oa-roma.inaf.it/spress/gclusters.html> (Calamida et al., 2007). The observations had been obtained with the Nordic Optical Telescope (NOT) on a small field of view of about 4×4 arcmin (see Fig. 5.1), with median seeing and pixel size of 0.6 and 0.175 arcsec, respectively. The zero-points were estimated using bright stars in common between the two datasets, adopting a 3σ -clipping procedure to exclude outliers. We verified the absence of possible colour correction terms between the two datasets. Figure 5.2 shows the stars used for the calibration, and the correspondent estimated zero-points for each filter. The complete catalogue will be made available through the CDS.

²www.bo.astro.it/~paolo/Main/CataPack.html

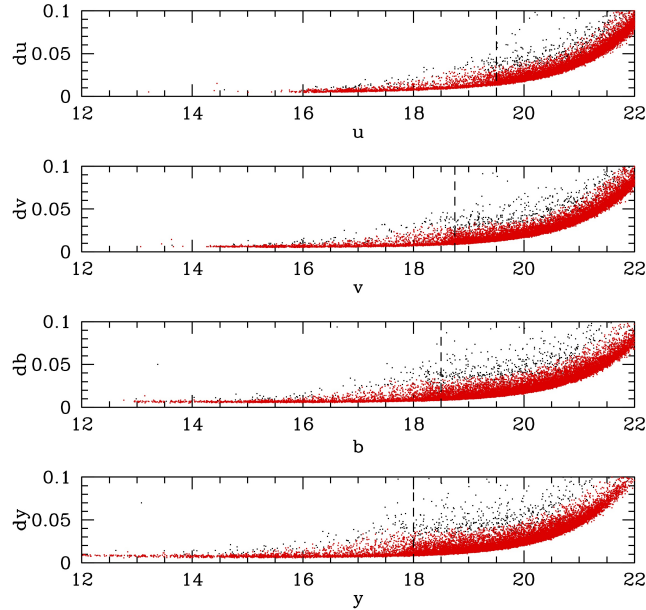


Figure 5.3: The photometric uncertainty as a function of magnitude for all stars with $|sharp| < 0.3$. The red points are the stars selected by our photometric error cut. The dashed vertical lines mark the position of the main sequence turn-off.

5.3 Colour-magnitude diagram

Our goal is to characterize M13 multiple populations on a photometric basis, and thus precise and reliable magnitudes are essential. For this reason, we applied a quality selection to our catalogue, to exclude stars with bad magnitude estimates, as well as non-stellar objects (background galaxies, cosmic rays, bad pixels, etc.) that were not identified properly during the photometric reduction.

We first applied a selection on the basis of DAOPHOT sharp parameter. This parameter is defined to be zero for point-like sources. A large positive sharp value typically means that the source is extended. A large negative sharp value means that the object is much smaller than the point spread function width, so it is likely to be an artifact. With that in mind, we excluded all the sources with $|sharp| \geq 0.3$.

Figure 5.3 shows the photometric error distribution as a function of magnitude, after the cut in sharp. We use this distribution to clean our sample further. We include only those stars that, in all four filters, are within three standard deviation from the

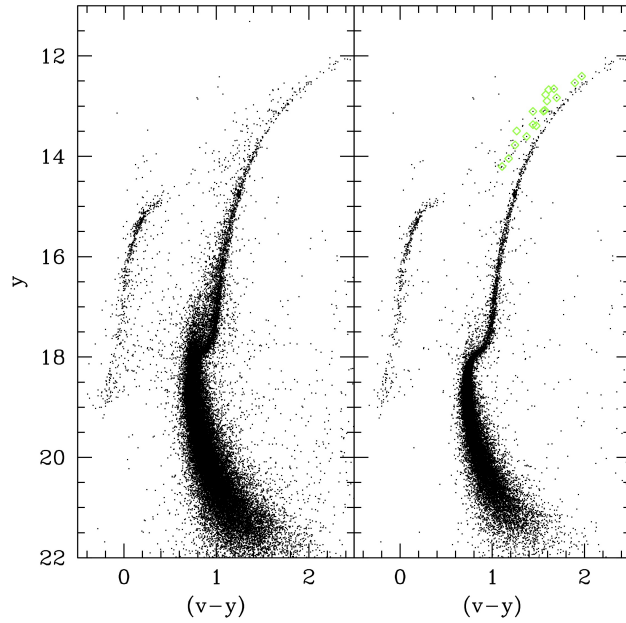


Figure 5.4: M13 $(v - y)$ vs y CMD. *Left panel:* the entire photometric catalogue. *Right panel:* only the stars selected by our cleaning criteria. Green diamonds are AGB stars with spectroscopic measurements (see § 5.4.1 for details).

mean photometric uncertainty at a given magnitude. The stars that do not satisfy this criterion are marked as black points in Fig. 5.3.

Figure 5.4 shows the resulting $(v - y)$ vs y colour magnitude diagram (CMD) before and after the selection. Our cleaning criteria are able to exclude most of stars scattered across the CMD, eliminating most of the potential contaminants. The cleaned sample makes each evolutionary phase more defined, as it can be seen by the thinness of the RGB.

Despite the absence of exposures shorter than 30 seconds in our dataset, we are able to recover the magnitude of bright giants up to $y \sim 12$. On the faint end we are able to detect stars ~ 4 magnitudes fainter than the main sequence turn off.

5.4 M13 multiple populations

As it has been demonstrated by numerous studies (e.g., Yong et al., 2008; Carretta et al., 2011; Sbordone et al., 2011; Roh et al., 2011; Massari et al., 2016), Strömgren

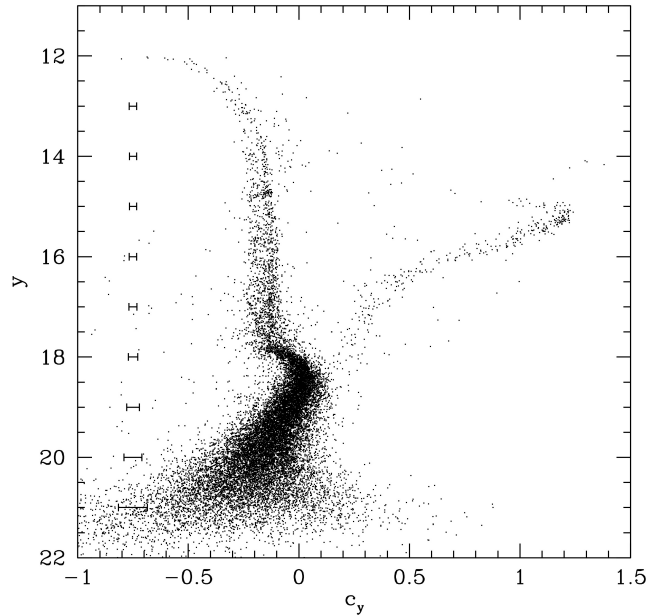


Figure 5.5: M13 CMD in the c_y index versus the y magnitude, extracted from our final catalogue. Average error bars in c_y are plotted to permit an easy comparison with the width of the RGB.

photometry is a powerful tool to characterize the chemical abundance of GC red giant stars. The small width of Strömgren filters, together with their characteristic wavelength, makes them sensitive to the strength of wide molecular features, such as the CN, CH and NH bands (see e.g. fig. 12 in Carretta et al., 2011).

In particular, the c_y index, defined by Yong et al. (2008)³, has the advantage of being less sensitive to temperature than the commonly used c_1 index, and it strongly correlates with the nitrogen abundance. Figure 5.5 shows the c_y vs y CMD of M13. The RGB clearly splits in two sequences, and the average spread is not compatible with the photometric uncertainties.

5.4.1 Spectroscopic confirmation

Given the correlation between the c_y index and the nitrogen abundance, we expect M13 multiple populations to reside in different regions of the RGB in Fig. 5.5. In particular, we expect N-poor stars to be located on the left side of the c_y vs y RGB, while the

³ $c_y = c_1 - (b - y)$, with $c_1 = (u - v) - (v - b)$

N-rich giants should occupy the right side. As M13 is a well studied globular cluster, we can confirm this, extending the work done by Carretta et al. (2011) on the original NOT data, and trace the c_y boundary between different populations, by comparing the results from our catalogue with other independent analyses.

We examine RGB stars for which light element abundances are available. We cross-match our photometric catalogue with three different spectroscopic samples, taken from Sneden et al. (2004), Cohen & Meléndez (2005) and Johnson & Pilachowski (2012). Across our field of view, we detect 31, 22 and 106 stars, belonging respectively to these datasets.

We use these elemental abundances to separate the different populations, with the criterion introduced in Carretta et al. (2009). We classify our stars into primordial (P), intermediate (I) and extreme (E) populations, based on their [O/Fe] and [Na/Fe] abundances. We call P population those stars with a [Na/Fe] abundance between the minimum measured value $[\text{Na/Fe}]_{min}$ (estimated excluding obvious outliers) and $[\text{Na/Fe}]_{min} + 0.3$. The I and E populations are defined as the non-P stars with $[\text{O/Na}] > -0.9$ dex and $[\text{O/Na}] < -0.9$, respectively.

Given the intrinsic differences among the three spectroscopic analyses, such as the spectral resolution and the choice of NLTE corrections, we prefer to apply this criterion separately for each sample, rather than consider all the abundance determinations together. In this way, we avoid the problem of possible zero-point offsets between the different elemental abundance samples.

An additional advantage of treating the samples individually is the presence of stars in common among them, that can be used to check the consistency of the different abundance scales. We have a total of 29 stars with multiple elemental abundance determinations. The catalogues from Sneden et al. (2004) and Johnson & Pilachowski (2012) have 26 stars in common, of which four are also present in Cohen & Meléndez (2005). The common targets between Cohen & Meléndez (2005) and Johnson & Pilachowski (2012) are seven.

The classification of these stars is in excellent agreement, with only three stars having

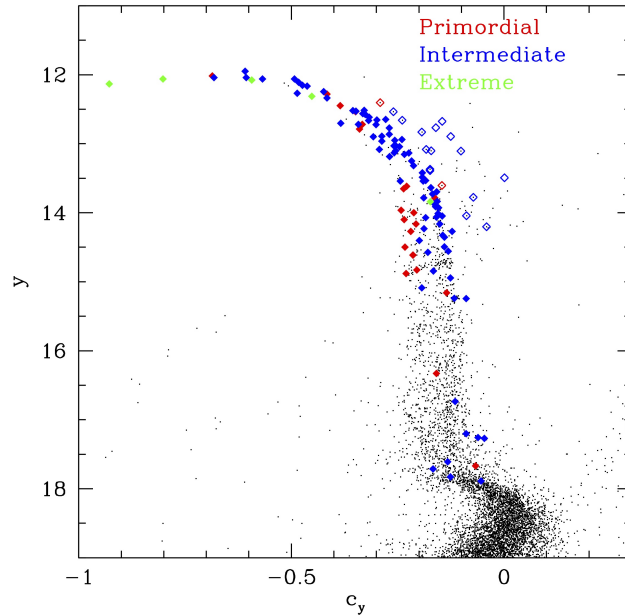


Figure 5.6: M13 c_y vs y CMD (black dots). The diamonds are the stars for which we have spectroscopic data, divided into primordial (red), intermediate (blue) and extreme (green) populations. The empty diamonds are stars that we identify as AGBs.

discordant classifications. Visual inspection reveals that these stars are located near the boundaries, in the parameter space, used to define the different populations. Thus, in principle, these different classifications are compatible with the spectroscopic errors. Given this classification issue we removed these three stars from our sample.

Figure 5.6 shows the spectroscopic targets, colour coded by population, superimposed to our c_y vs y CMD. Unfortunately, most of the elemental abundances are available only for very bright stars, where the pseudo-colour c_y is unable to separate the populations. Nonetheless, we reach magnitudes as faint as that of the RGB bump, where a clear separation is seen between the primordial and the enriched populations. It has already been shown (Carretta et al., 2011), that the optimal separation in c_y is obtained for stars at the level of the RGB bump and below. The result shown in Fig. 5.6 confirms our ability to use photometry to distinguish between primordial and enriched populations. The mostly clean segregation of the two populations in c_y allows us to define a photometric criterion to classify M13 stars based on their position on the RGB. As our spectroscopic sample is only representative of stars with $y < 15$, the classification of fainter RGB stars unavoidably requires an extrapolation of the trend we observe.

It is interesting that the stars with extreme chemical enrichment are mainly found near the tip of the RGB. This behaviour has already been mentioned by the authors of the three spectroscopic studies (note that the different number of E stars between our work and Johnson & Pilachowski, 2012, is due to different classification criteria). There is only one E star that falls in the magnitude range where the c_y spread is significant. As this is not enough to distinguish I and E stars on a photometric basis, in the rest of the analysis we will collectively refer to the I and E stars as the enriched population.

It should be noted that M13 has for long time been the prototype of a GC with very high O depletion, before the analysis of more extreme clusters, in particular NGC2808 (Carretta et al., 2006). Such clusters, however, do not show an excess of extreme stars near the RGB tip. In the case of NGC2808, this can be seen in the analysis of Carretta (2015). In spite of tentative explanations (such as the presence of extra mixing in bright stars, suggested by D’Antona & Ventura, 2007), the unique behaviour of very O-depleted stars in M13 still has to be understood properly. In addition, the presence of kinematic peculiarities in the extreme stars (Cordero et al., 2017), makes this population a very interesting subject for further investigation.

As a final remark, we have elemental abundances for a large sample of asymptotic giant branch (AGB) stars (empty symbols in Fig. 5.6). The AGB nature of these stars is more easily seen in Fig. 5.4 (green diamonds), where they clearly separated from the RGB. Many of the AGB show [O/Fe] and [Na/Fe] ratios typical of the enriched population. In particular, we classify 15 AGB stars to be part of the enriched population while only two AGB show elemental abundances compatible with the primordial population. While the fraction of enriched stars on the AGB ($88.2^{+4.7}_{-23.2}$ per cent) is somewhat higher than that observed on the RGB (see § 5.4.2), the uncertainties coming from the small sample size fully account for this difference.

This detection is interesting in the light of the recent controversy on the presence of second population stars on the AGB of globular clusters (see, e.g., Campbell et al., 2013; Lapenna et al., 2016; MacLean et al., 2016; Massari et al., 2016; Lardo et al., 2017; Gruyters et al., 2017). Stellar evolution theory predicts a fraction of enriched stars on the AGB of GCs, comparable or lower than what observed on the RGB de-

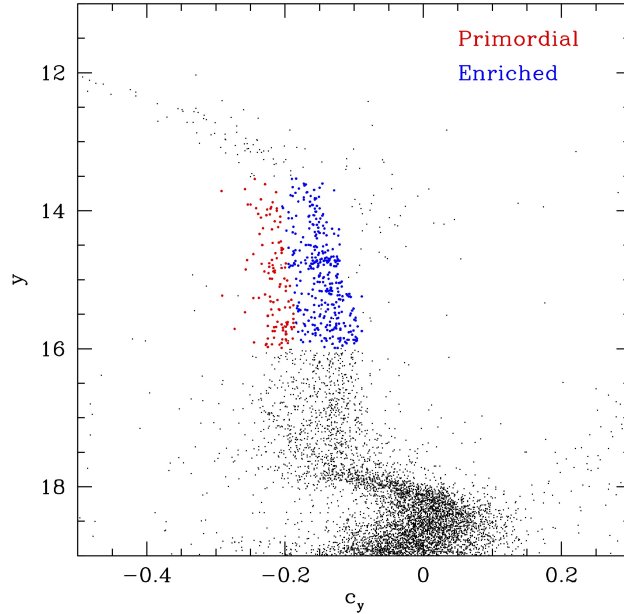


Figure 5.7: M13 c_y vs y CMD (black dots). The red and blue dots represent, respectively, the primordial and enriched population as selected by our photometric criterion. The upper and lower magnitude range for our selection have been obtained by comparison with HST data. See the text for more details.

pending on the horizontal branch morphology. However, the presence of these stars is currently debated, with different studies that yield contrasting results. It should be noted, that a scenario where second population stars skip the AGB altogether is hard to reconcile with standard stellar evolution, even when invoking extreme mass loss (Cassisi et al., 2014). Our detection in M13 favours enriched stars to ascend the AGB phase, as predicted by stellar population models.

5.4.2 Radial profiles

The photometric criterion we derived from our comparison with spectroscopy allows us to assign a population membership to RGB stars based solely on their position in the c_y vs y CMD (Fig. 5.7), where we have already applied the refined classification from a comparison with HST data (see below, Fig. 5.8). In order to avoid foreground contamination we apply the procedure described in Frank et al. (2015), to select genuine RGB stars on the basis of their position in the $(b - y)$ vs c_1 and $(b - y)$ vs m_1

planes.

According to this distinction, the fraction of enriched stars in M13 is $74.5^{+1.9}_{-2.2}$ per cent. For comparison, the fraction estimated from the spectroscopic sample is $79.8^{+3.2}_{-4.7}$ per cent. Before we proceed to the spatial characterization of these populations, some preliminary considerations need to be made regarding the completeness of our stellar catalogue.

For dense stellar systems such as Galactic GCs, the completeness level of post main sequence stars is driven mainly by crowding. Completeness varies with the radius of the globular cluster, with stars preferentially lost in the centre of the cluster rather than in the outskirts. The observed radial distribution is therefore less concentrated than the intrinsic one. For completely mixed populations, this effect is irrelevant, as stars are lost in the same way in the different populations. If one of the stellar populations is more concentrated than the others, it is affected more by incompleteness, and the net effect is a softening in the radial distribution difference.

This observational bias can be potentially important for INT observations. While the large field of view makes this telescope a great tool to study the external regions of the cluster, the typical seeing of our images makes it quite sensitive to the crowding of the cluster core.

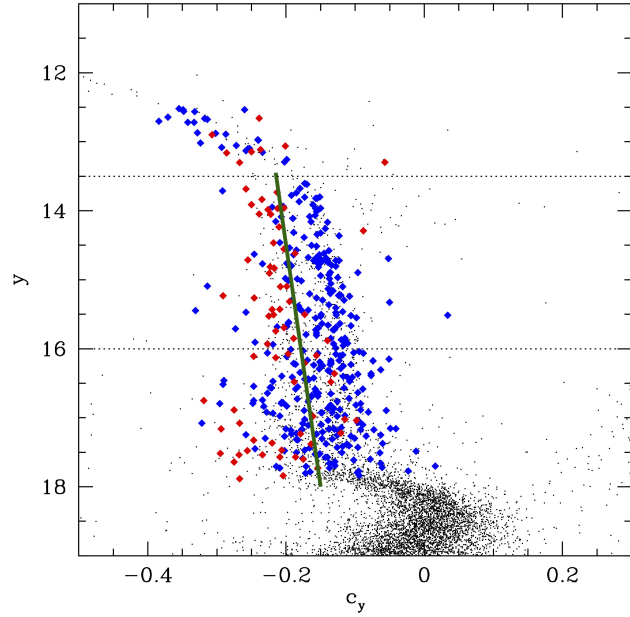
To assess this issue, we make use of HST observations from the ACS Globular Cluster Survey (Sarajedini et al., 2007). We compare our catalogue with HST data in the inner 90 arcsec of the cluster to estimate the difference in the number of detected RGB stars. Even though this comparison only permits us to derive only a relative completeness fraction, the performance of HST in crowded fields is such that nearly all the bright evolved stars are detected, even in the densest region of the cluster.

This instructive comparison allows us to determine that, over the central 90 arcsec of the cluster, the level of completeness of our catalogue is approximately 35 per cent. Such a low fraction of detected stars is mainly the consequence of our very conservative selection criteria. The cuts in sharp and photometric error described in § 3, while necessary to ensure an accurate characterization of the RGB in terms of c_y index, reject

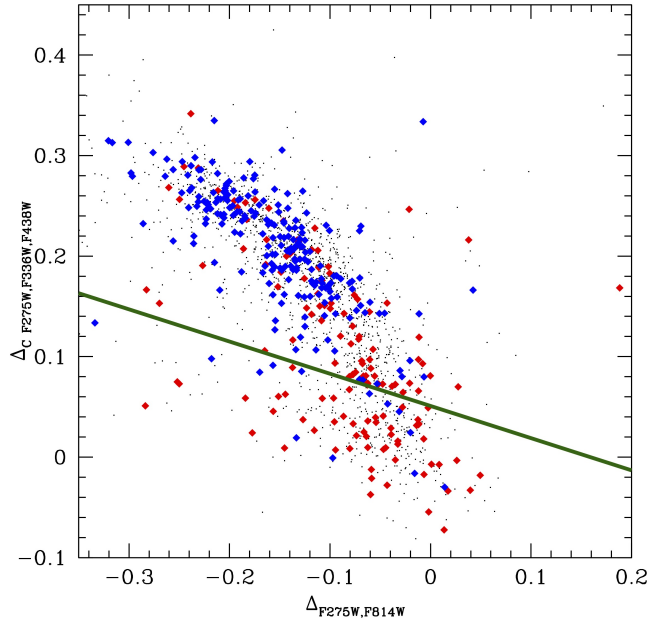
a large number of stars with poorly determined magnitudes. This is verified by looking at the completeness level of the catalogue prior to any cleaning selection, and this is nearly 100 per cent.

The low completeness level in the cluster centre makes it very difficult to assess the presence of different radial concentration with the INT observations of this region. For this reason we decided to use our catalogue to study the external regions of M13, while in the centre we make use of more accurate HST observations. As previously demonstrated. (e.g., Milone et al., 2012), HST is a very powerful instrument to study the multiple populations of globular clusters. We thus make use of data from the preliminary data release of the UV Legacy Survey of Galactic Globular Clusters (Piotto et al., 2015; Soto et al., 2017). We follow the procedure described in Milone et al. (2017) to distinguish primordial and enriched populations on the basis of M13 ‘chromosome map’ (see fig. 5 of Milone et al., 2017). Chromosome mapping is a technique that exploits the position of stars on the RGB, using different filter combinations, to distinguish between primordial and enriched populations. In particular, the two indices used are sensitive to light element and helium variations respectively. The fraction of enriched stars recovered with this method is $80.4^{+0.9}_{-1.0}$ per cent.

Before analysing the multiple population distribution in M13, it is important to assess the consistency of the results obtained with different instruments. Because of the different photometric filters of INT and HST, as well as the different methodologies employed to separate the two populations, we need to verify that the primordial and enriched populations as recovered by HST are consistent with those in our INT data. We cross-match the two catalogues and assess how the HST-defined multiple populations distribute in the c_y vs y CMD, and vice versa (Fig. 5.8). We found that stars labelled as primordial or enriched on the basis of the HST chromosome map tend to separate in the c_y distribution. The agreement with the criterion we defined using spectroscopic data is good, at least for the bright RGB, where INT photometric errors are small enough to permit an accurate classification. We make use of this comparison for a further calibration of our photometric criterion and to avoid extrapolation for stars with $y < 15$.



(a)



(b)

Figure 5.8: a) M13 c_y vs y CMD from the INT catalogue (black dots). The diamonds are the stars in common with the HST catalogue, divided into primordial (red) and enriched (blue) on the basis of the HST chromosome map criterion. The solid green line shows the photometric criterion defined by equation 5.1. The dotted black lines mark the magnitude range that we use for our analysis. b) Chromosome map built from the HST dataset (black dots). The diamonds are the stars in common with the INT catalogue, divided into primordial (red) and enriched (blue) on the basis of the INT photometric criterion. The solid green line shows the criterion used to separate multiple populations, corresponding to the mean ridge line for the lower sequence, shifted by three times the photometric uncertainty.

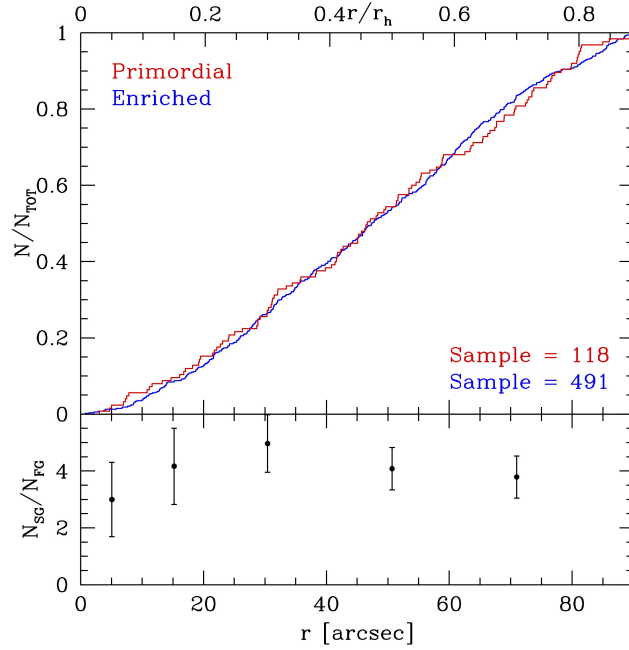


Figure 5.9: Upper panel: the cumulative distributions for the primordial (red) and enriched (blue) populations in the central regions of M13, obtained using HST data from the UV Legacy Survey of Galactic Globular Clusters. Lower panel: the number ratio of enriched stars to primordial stars in different radial bins.

In this way the division between primordial and enriched population is given by:

$$c_y = 0.014 \cdot y + 0.407 \quad (5.1)$$

which is applied for $13.5 < y < 16$ and $-0.3 < c_y < 0.07$. The magnitude range is the one for which the HST and INT multiple populations are in good agreement. We note that there are stars for which the two classification criteria don't match. In the colour and magnitude range specified above, the fraction of these stars is around 15%.

The radial distribution of the two populations that we find with HST is shown in Fig. 5.9. The two radial profiles are almost indistinguishable, suggesting a complete spatial mixing of the two populations. A Kolmogorov-Smirnov (KS) test gives us a probability of 94.9 per cent that the two distributions are drawn from the same parent population. As mentioned before, the field of view of HST allows us to cover only the inner 90 arcsec of the cluster, which correspond to slightly less than one half-light radius. The complete mixing of the two populations is thus unsurprising, as the dy-

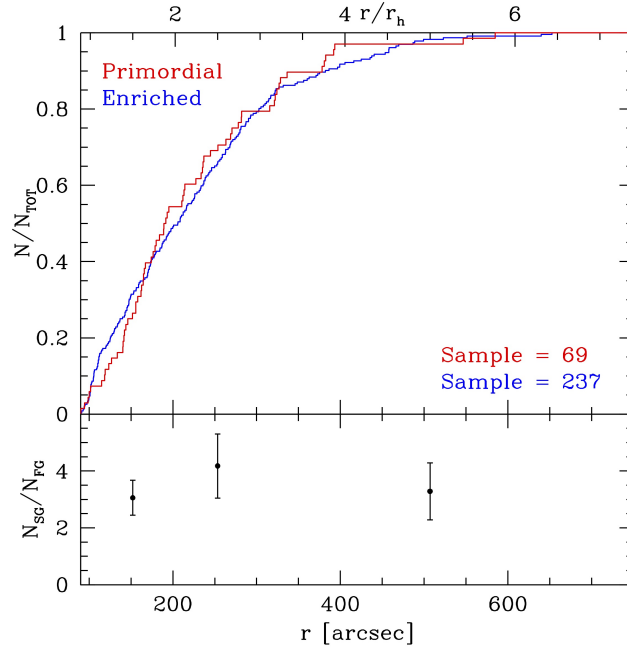


Figure 5.10: As for Fig. 5.9 but for the outer regions of M13. These distributions have been obtained using our INT catalogue.

namical timescales in this region are very short.

The occurrence of complete mixing in the cluster centre simplifies the study of outer spatial distributions. By definition, the shape of a cumulative distribution is influenced by the global properties of the sample. Making a separate cumulative distribution for the outer regions could in principle have led to a biased comparison, as the central properties were not taken into account. However, the high level of mixing in M13 core reassures us that any difference in the global spatial distribution of M13 multiple populations would be driven by the stars in the outer regions. In this context, a comparison of the outer regions alone is relatively safe.

As it can be seen from Fig. 5.10, the trend observed in the centre seems to continue also in the outskirts of cluster. The KS probability that the primordial and enriched radial distributions are representations of the same parent population is 65.2 per cent. While this test does not allow us to conclusively exclude the presence of some radial gradients between the multiple populations of M13, it is fair to conclude that they should be only minor and limited to the most external regions where we only have a small sample of stars.

5.5 Discussion and Conclusions

In this work, we analysed a photometric dataset in Strömgren *ubvy* filters to characterize the multiple stellar populations of the Galactic GC NGC6205 (M13). The use of the c_y photometric index revealed the presence of a spread on the RGB, consistent with the chemical inhomogeneity within the cluster.

The comparison with several spectroscopic studies, confirmed that the c_y index is a very efficient tracer of the light element abundance in RGB stars, and allows us to distinguish enriched and primordial populations on the basis of their position on the CMD.

Our analysis concluded that around 80 per cent of M13 giant stars belong to the enriched population. This high fraction is in line with the trend of enriched population fraction versus cluster absolute magnitude found by Milone et al. (2017).

To study the radial distribution of M13 multiple populations we complemented our dataset with HST observations from the UV Legacy Survey of Galactic Globular Clusters. The analysis of the radial profiles over a wide field of view revealed no significant evidence for spatial dishomogeneities between the primordial and the enriched population, neither in the inner nor the outer regions of the cluster.

This result is at odds with what was found by Lardo et al. (2011), who detected a radial gradient in the multiple population distribution of many clusters, including M13. The causes for these discordant results are difficult to assess. However, we note that Strömgren filters have a significantly smaller bandwidth and are more sensitive to light element abundances compared to the Sloan passbands used in Lardo et al. (2011). The photometric accuracy of our dataset is also better. Finally, we stress that the classification criteria of both studies have been defined empirically.

To date, only a few GCs have been observed to have fully spatially mixed multiple populations (Dalessandro et al., 2014; Nardiello et al., 2015). In this light, such a finding for M13 stars is very interesting, especially given that M13 is the most massive cluster in which this phenomenon has been observed.

An interesting comparison can be drawn with NGC5272 (M3). These two clusters are very similar in terms of mass, age and metallicity, and are a classical horizontal branch second parameter problem pair (e.g. Dalessandro et al., 2013). In contrast to M13, M3 multiple populations have been found to be mixed only out to ~ 0.6 half-light radii, while at larger distance from the cluster centre the enriched population is significantly more concentrated (Massari et al., 2016).

We suggest that this difference can be understood when considering the dynamical properties of the two clusters. M13's relaxation time at the half-light radius is of the order of 2 Gyrs, which is about three times shorter than that of M3 (Harris, 1996, 2010 version) and similar to that of the completely mixed NGC6362 (Dalessandro et al., 2014). As the dynamical timescale increases in the less dense regions of a stellar cluster, M3 has achieved a full spatial mixing only in its central part, while the more efficient M13 has also managed to become mixed in its outskirts. Following this argument, we expect that completely mixed stellar populations should be observed in clusters with similar, or shorter, relaxation times (e.g., M71, M30 or NGC 6218).

Chapter 6

Concluding remarks and future prospects

In this thesis I developed and validated tools to investigate the detailed properties of ancient stellar populations in the Local Group. In chapter 2 I have shown that current star formation history (SFH) analysis, based on the main sequence turn-off (MSTO), becomes less accurate at old ages. This was shown by analysing the horizontal branch (HB) of the Carina dSph, highlighting how star formation in certain regions of the age-metallicity space is ruled out by the absence of specific features in the observed HB of this galaxy. This demonstrated that the HB contains additional information that can be used to refine the accuracy of our measurements of the SFH of galaxies, based on their resolved populations.

This result motivated me to develop a new colour-magnitude diagram (CMD) modelling tool, presented in chapter 3, that, for the first time, determines the SFH of a galaxy combining detailed HB and MSTO modelling. The additional constraints coming from the HB result in a noticeable increase in the age resolution. This new approach also determines the amount of mass lost by stars on the RGB, providing precious insights to this long-standing uncertainty. This new method was demonstrated on the well studied Sculptor dwarf spheroidal galaxy (dSph), where the careful modelling of the HB can clearly distinguish the two known events of star formation. These two

events are more accurately measured than previous SFH analysis allowed, based only on the MSTO.

An application of this method to the distant Tucana dSph, in chapter 4, further demonstrated that, with high quality photometry, the modelling of the whole CMD, including the HB, improves the accuracy of the early star formation history of resolved galaxies. I confirmed the presence of the two distinct stellar populations that were already known and reported the presence of an additional third, younger, stellar population. This new and more detailed SFH for Tucana clearly shows that a multimodal stellar distribution along the HB is directly linked to a similarly complex star formation history. Not of minor importance, the modelling of the whole CMD resulted in a very accurate measurement of the RGB mass loss.

The work I carried out on dSphs contributes to the study of complex ancient stellar populations in low mass galaxies. The presence of distinct stellar components in these galaxies has been established by many independent investigations. The origin of this complexity is still unclear. Some of the proposed scenarios invoke mergers of different stellar systems (Amorisco & Evans, 2012a; del Pino et al., 2015) or bursty in-situ star formation (Salvadori et al., 2008; Revaz et al., 2009), potentially providing constraints to the picture of hierarchical mass assembly and to the efficiency of supernova feedback in low mass haloes. To date, our observational characterisation of dSphs cannot provide a clear picture of the early history of these systems. With the possibility to accurately detect these distinct early stellar components in a SFH, we can add valuable information. Reliable time scales are notoriously challenging to obtain for old stellar populations.

The next logical step for the work presented in chapters 2, 3 and 4 will be to extend the analysis of the HB to additional Local Group dSphs, to build a large sample of accurate high-resolution SFHs. This will provide us with the ability to identify differences and similarities in the very early history of Local Group galaxies. In a broader context, the information of the detailed SFH of dSphs can be combined with the constraints coming from chemical abundance and velocity measurements, to build a complete picture of the chemo-dynamical mechanisms that shape low mass galaxies, with the

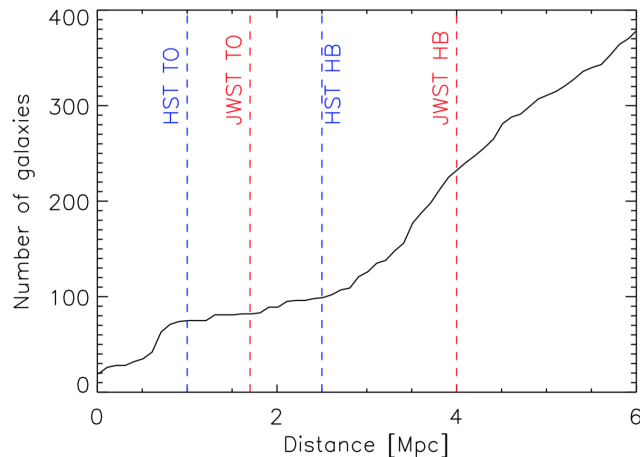


Figure 6.1: The cumulative number of known galaxies as a function of distance from the Milky Way, from the catalogue of Karachentsev et al. (2013). The dashed lines represent the detection limits, for 10 hours of integration, with HST and JWST of either old turn-off and horizontal branch stars in a 12.5 Gyr old stellar population with a metallicity of $[\text{Fe}/\text{H}] = -2.0$.

aim of disentangling the relative contributions of environmental and internal processes.

A second, equally important, benefit of modelling a larger sample of dSphs with MOR-GOTH will be to obtain a large number of measurements of the RGB mass loss in different extragalactic stellar systems. Such measurements will make it possible to understand this poorly constrained process, which remains one of the biggest uncertainties in stellar evolution theory. In addition, being able to determine the behaviour of RGB mass loss in a range of stellar systems will make it possible to calibrate the process, enabling us to measure detailed SFHs from the bright CMD alone. Detailed SFH measurements have so far mostly been confined to the Local Group, due to the necessity of detecting the old MSTOs. This not only limits the available sample of galaxies for which we have access to the old record of star formation, but also raises the possibility that the Local Group could somehow be a special environment, biasing our view of galaxy formation.

Next generation observing facilities, such as the James Webb Space Telescope and the 30-m class observatories, will provide increased sensitivity and spatial resolution that will allow us to resolve individual stars in more distant galaxies. Fig. 6.1 shows the cumulative distribution of known galaxies as a function of distance from the Milky Way. It can be seen how the improved observing capabilities of the James Webb Tele-

scope will only slightly increase the number of galaxies that can be resolved down to MSTO. This is due to the inhomogeneous distribution of galaxies on scales of a Mpc. In contrast, HBs are much brighter than the equivalent MSTOs and will be detectable for galaxies many Mpc away.

As demonstrated by Boylan-Kolchin et al. (2016), the study of nearby galaxies probes a co-moving volume that extends much beyond the present size of the Local Group neighbourhood. Thanks to the analysis of the HB with James Webb Space Telescope, we will have access to the formation histories for a sample of galaxies that is roughly five times larger than we have today. The co-moving volume spanned by the progenitors of these systems is expected to be of the order of $10^4 Mpc^3$ at $z \sim 7$, which is a cosmologically representative sample of the early Universe and much larger than what is probed by the HST Ultra Deep Field or any future deep JWST field.

Chapter 5 was devoted to the study of the massive globular cluster NGC6205 (M13). Carrying on on the work of Carretta et al. (2011) and Massari et al. (2016), I confirmed the effectiveness of Strömgren photometry to detect the multiple stellar populations in a resolved globular cluster. I analysed the spatial distribution of the multiple stellar populations out to 6.5 half-light radii and found no evidence for radial segregation in any region of the cluster. The comparison of my results with the work done on M3, which is similar to M13 in many regards and has a strong radial gradient in its multiple population distribution, not only highlights how these clusters are different in their multiple stellar population properties, but shows the importance of taking the dynamical state into account when characterising distinct components in dense stellar systems. In this regard, when complementary information on the stellar content comes from, e.g., the HB modelling, the distributions of multiple stellar population within a globular cluster can prove to be an independent clock for the dynamical evolutionary state of the object.

As for dSphs, the next step forward would be to carry a large survey of the multiple populations in globular clusters, employing Strömgren photometry to probe the outer regions of these systems. In June 2018 I have carried out wide-field Strömgren imaging, with the Wide-Field Camera on the Isaac Newton Telescope, for 17 globular

Table 6.1: List of Galactic star clusters included in the Wide-Field Strömgren survey carried out in June 2018. Metallicities, half light radii (r_h , in arcminutes) and relaxation times at the half light radius (t_h , in years) come from the 2010 version of Harris (1996). Estimates for the mass come from Baumgardt (2017).

Name	Alternative Name	$[Fe/H]$	$\log \frac{M}{M_\odot}$	r_h	$\log t_h$
NGC 5024	M 53	-2.10	5.58	1.31	9.76
NGC 5634		-1.88	5.33	0.86	9.54
NGC 5904	M 5	-1.29	5.57	1.77	9.41
NGC 6093	M 80	-1.75	5.40	0.61	8.80
NGC 6171		-1.02	4.94	1.73	9.00
NGC 6218	M 12	-1.37	4.94	1.77	8.87
NGC 6229		-1.47	-	0.36	9.15
NGC 6254	M 10	-1.56	5.26	1.95	8.90
NGC 6341	M 92	-2.31	5.43	1.02	9.02
NGC 6535		-1.79	4.3	0.85	8.20
NGC 6712		-1.02	-	1.33	8.95
NGC 6791	M 107	0.41	-	-	-
NGC 6838	M 71	-0.78	4.69	1.67	8.43
NGC 7078	M 15	-2.37	5.66	1.00	9.32
NGC 7089	M 2	-1.65	5.76	1.06	9.40
Palomar 5		-1.41	-	2.73	9.82
Palomar 11		-0.40	-	1.46	9.34
Palomar 14	AvdB	-1.62	-	1.22	10.02

clusters and one old open cluster (NGC6791), over a field of view of about 30×30 arcmin.

A list of the targets observed, along with some key properties, is reported in Table 6.1. Some of these targets have never been searched for multiple populations before (NGC 6229 and Palomar 11), whereas only tentative evidence exists for others (NGC 6791 and Palomar 14). The data reduction strategy and the analysis will be developed from the procedure outlined in chapter 5. The main goal of this survey will be to identify, if present, and trace the multiple populations out to the most external regions of the targets. Where sample overlap is present, this data will be a useful complement to HST surveys, which are deep and precise but have limited spatial coverage, and high-resolution spectroscopic investigations, which are limited by the sample size.

Bibliography

Aaronson M., Mould J., 1985, ApJ, 290, 191

Agnello A., Evans N. W., 2012, ApJl, 754, L39

Aloisi A., Tosi M., Greggio L., 1999, AJ, 118, 302

Amorisco N. C., Evans N. W., 2012a, ApJl, 756, L2

Amorisco N. C., Evans N. W., 2012b, MNRAS, 419, 184

Aparicio A., Gallart C., Bertelli G., 1997, AJ, 114, 680

Aparicio A., Hidalgo S. L., 2009, AJ, 138, 558

Aparicio A., Hidalgo S. L., Skillman E., Cassisi S., Mayer L., Navarro J., Cole A.,
Gallart C., Monelli M., Weisz D., Bernard E., Dolphin A., Stetson P., 2016, ApJ,
823, 9

Bastian N., Cabrera-Ziri I., Salaris M., 2015, MNRAS, 449, 3333

Bastian N., Lamers H. J. G. L. M., de Mink S. E., Longmore S. N., Goodwin S. P.,
Gieles M., 2013, MNRAS, 436, 2398

Bastian N., Lardo C., 2015, MNRAS, 453, 357

Bastian N., Lardo C., 2017, ArXiv e-prints

Battaglia G., Irwin M., Tolstoy E., Hill V., Helmi A., Letarte B., Jablonka P., 2008,
MNRAS, 383, 183

- Battaglia G., Tolstoy E., Helmi A., Irwin M. J., Letarte B., Jablonka P., Hill V., Venn K. A., Shetrone M. D., Arimoto N., Primas F., Kaufer A., Francois P., Szeifert T., Abel T., Sadakane K., 2006, *A&A*, 459, 423
- Baumgardt H., 2017, *MNRAS*, 464, 2174
- Beauchamp D., Hardy E., Suntzeff N. B., Zinn R., 1995, *AJ*, 109, 1628
- Beccari G., Bellazzini M., Lardo C., Bragaglia A., Carretta E., Dalessandro E., Mucciarelli A., Pancino E., 2013, *MNRAS*, 431, 1995
- Bellazzini M., Ferraro F. R., Pancino E., 2001, *MNRAS*, 327, L15
- Bernard E. J., Gallart C., Monelli M., Aparicio A., Cassisi S., Skillman E. D., Stetson P. B., Cole A. A., Drozdovsky I., Hidalgo S. L., Mateo M., Tolstoy E., 2008, *ApJL*, 678, L21
- Bernard E. J., Monelli M., Gallart C., Drozdovsky I., Stetson P. B., Aparicio A., Cassisi S., Mayer L., Cole A. A., Hidalgo S. L., Skillman E. D., Tolstoy E., 2009, *ApJ*, 699, 1742
- Bono G., Caputo F., Stellingwerf R. F., 1995, *ApJS*, 99, 263
- Bono G., Stetson P. B., Walker A. R., Monelli M., Fabrizio M., Pietrinferni A., Brocato E., Buonanno R., Caputo F., Cassisi S., Castellani M., Cignoni M., et al. 2010, *PASP*, 122, 651
- Boylan-Kolchin M., Weisz D. R., Bullock J. S., Cooper M. C., 2016, *MNRAS*, 462, L51
- Breddels M. A., Helmi A., van den Bosch R. C. E., van de Ven G., Battaglia G., 2013, *MNRAS*, 433, 3173
- Brown T., Ferguson H., Gardner J., Greggio L., Hammel H. B., Renzini A., Rich M., Richer H., Stiavelli M., Wyse R., 2008, *JWST White Paper*
- Calamida A., Bono G., Stetson P. B., Freyhammer L. M., Cassisi S., Grundahl F., Pietrinferni A., Hilker M., Primas F., et al. 2007, *ApJ*, 670, 400

- Caloi V., D'Antona F., 2008, *ApJ*, 673, 847
- Campbell S. W., D'Orazi V., Yong D., Constantino T. N., Lattanzio J. C., Stancliffe R. J., Angelou G. C., Wylie-de Boer E. C., Grundahl F., 2013, *Nature*, 498, 198
- Carretta E., 2015, *ApJ*, 810, 148
- Carretta E., Bragaglia A., Gratton R., D'Orazi V., Lucatello S., 2011, *A&A*, 535, A121
- Carretta E., Bragaglia A., Gratton R. G., Leone F., Recio-Blanco A., Lucatello S., 2006, *A&A*, 450, 523
- Carretta E., Bragaglia A., Gratton R. G., Lucatello S., Catanzaro G., Leone F., Bellazzini M., Claudi R., D'Orazi V., Momany Y., Ortolani S., Pancino E., Piotto G., Recio-Blanco A., Sabbi E., 2009, *A&A*, 505, 117
- Carretta E., Bragaglia A., Gratton R. G., Recio-Blanco A., Lucatello S., D'Orazi V., Cassisi S., 2010, *A&A*, 516, A55
- Cassisi S., Salaris M., 2013, *Old Stellar Populations: How to Study the Fossil Record of Galaxy Formation*
- Cassisi S., Salaris M., Castelli F., Pietrinferni A., 2004, *ApJ*, 616, 498
- Cassisi S., Salaris M., Irwin A. W., 2003, *ApJ*, 588, 862
- Cassisi S., Salaris M., Pietrinferni A., Vink J. S., Monelli M., 2014, *A&A*, 571, A81
- Catelan M., 2009, *Ap&SS*, 320, 261
- Cignoni M., Sabbi E., van der Marel R. P., Tosi M., Zaritsky D., Anderson J., Lennon D. J., Aloisi A., de Marchi G., Gouliermis D. A., Grebel E. K., Smith L. J., Zeidler P., 2015, *ApJ*, 811, 76
- Cignoni M., Tosi M., 2010, *Advances in Astronomy*, 2010, 158568
- Clementini G., Baldacci L., Bragaglia A., Carretta E., di Fabrizio L., Gratton R. G., Greco C., Gullieuszik M., Held E. V., Maio M., Marconi M., Matonti F., et al. 2004, in Kurtz D. W., Pollard K. R., eds, *IAU Colloq. 193: Variable Stars in the Local*

- Group Vol. 310 of Astronomical Society of the Pacific Conference Series, Distance scale, variable stars and stellar populations in Local Group galaxies. p. 60
- Cohen J. G., Meléndez J., 2005, *AJ*, 129, 303
- Cole A. A., Skillman E. D., Tolstoy E., Gallagher III J. S., Aparicio A., Dolphin A. E., Gallart C., Hidalgo S. L., Saha A., Stetson P. B., Weisz D. R., 2007, *ApJ*, 659, L17
- Coppola G., Stetson P. B., Marconi M., Bono G., Ripepi V., Fabrizio M., Dall’Ora M., Musella I., Buonanno R., Ferraro I., Fiorentino G., Iannicola G., Monelli M., Nonino M., Pulone L., Thévenin F., Walker A. R., 2013, *ApJ*, 775, 6
- Cordero M. J., Hénault-Brunet V., Pilachowski C. A., Balbinot E., Johnson C. I., Varri A. L., 2017, *MNRAS*, 465, 3515
- Da Costa G. S., Rejkuba M., Jerjen H., Grebel E. K., 2010, *ApJ*, 708, L121
- Dalessandro E., Cadelano M., Vesperini E., Salaris M., Ferraro F. R., Lanzoni B., Raso S., Hong J., Webb J. J., Zocchi A., 2018, *ArXiv e-prints*
- Dalessandro E., Lapenna E., Mucciarelli A., Origlia L., Ferraro F. R., Lanzoni B., 2016, *ApJ*, 829, 77
- Dalessandro E., Massari D., Bellazzini M., Miocchi P., Mucciarelli A., Salaris M., Cassisi S., Ferraro F. R., Lanzoni B., 2014, *ApJ*, 791, L4
- Dalessandro E., Salaris M., Ferraro F. R., Cassisi S., Lanzoni B., Rood R. T., Fusi Pecci F., Sabbi E., 2011, *MNRAS*, 410, 694
- Dalessandro E., Salaris M., Ferraro F. R., Mucciarelli A., Cassisi S., 2013, *MNRAS*, 430, 459
- Dall’Ora M., Ripepi V., Caputo F., Castellani V., Bono G., Smith H. A., Brocato E., Buonanno R., Castellani M., Corsi C. E., Marconi M., Monelli M., Nonino M., Pulone L., Walker A. R., 2003, *AJ*, 126, 197
- D’Antona F., Ventura P., 2007, *MNRAS*, 379, 1431

- de Boer T. J. L., Tolstoy E., Hill V., Saha A., Olsen K., Starkenburg E., Lemasle B., Irwin M. J., Battaglia G., 2012, *A&A*, 539, A103
- de Boer T. J. L., Tolstoy E., Lemasle B., Saha A., Olszewski E. W., Mateo M., Irwin M. J., Battaglia G., 2014, *A&A*, 572, A10
- de Boer T. J. L., Tolstoy E., Saha A., Olsen K., Irwin M. J., Battaglia G., Hill V., Shetrone M. D., Fiorentino G., Cole A., 2011, *A&A*, 528, A119
- de Mink S. E., Pols O. R., Langer N., Izzard R. G., 2009, *A&A*, 507, L1
- Decressin T., Meynet G., Charbonnel C., Prantzos N., Ekström S., 2007, *A&A*, 464, 1029
- del Pino A., Aparicio A., Hidalgo S. L., 2015, *MNRAS*, 454, 3996
- Denissenkov P. A., Hartwick F. D. A., 2014, *MNRAS*, 437, L21
- D’Ercole A., D’Antona F., Ventura P., Vesperini E., McMillan S. L. W., 2010, *MNRAS*, 407, 854
- D’Ercole A., Vesperini E., D’Antona F., McMillan S. L. W., Recchi S., 2008, *MNRAS*, 391, 825
- Di Criscienzo M., Marconi M., Caputo F., 2004, *ApJ*, 612, 1092
- Dolphin A., 1997, *NewA*, 2, 397
- Dolphin A. E., 2002, *MNRAS*, 332, 91
- Dolphin A. E., 2012, *ApJ*, 751, 60
- Dolphin A. E., 2013, *ApJ*, 775, 76
- Dotter A., Sarajedini A., Anderson J., Aparicio A., Bedin L. R., Chaboyer B., Majewski S., Marín-Franch A., Milone A., Paust N., Piotto G., Reid I. N., Rosenberg A., Siegel M., 2010, *ApJ*, 708, 698
- Fabrizio M., Merle T., Thévenin F., Nonino M., Bono G., Stetson P. B., Ferraro I., Iannicola G., Monelli M., Walker A. R., et al. 2012, *PASP*, 124, 519

- Fabrizio M., Nonino M., Bono G., Primas F., Thévenin F., Stetson P. B., Cassisi S., Buonanno R., Coppola G., et al. 2015, *A&A*, 580, A18
- Fattahi A., Navarro J. F., Sawala T., Frenk C. S., Oman K. A., Crain R. A., Furlong M., Schaller M., Schaye J., Theuns T., Jenkins A., 2016, *MNRAS*, 457, 844
- Fiorentino G., Bellazzini M., Ciliegi P., Chauvin G., Douté S., D’Orazi V., Maiorano E., Mannucci F., Mapelli M., Podio L., Saracco P., Spavone M., 2017, *ArXiv e-prints*
- Frank M. J., Koch A., Feltzing S., Kacharov N., Wilkinson M. I., Irwin M., 2015, *A&A*, 581, A72
- Gabriel M., Noels A., Montalbán J., Miglio A., 2014, *A&A*, 569, A63
- Gallart C., Aparicio A., Bertelli G., Chiosi C., 1996, *AJ*, 112, 1950
- Gallart C., Zoccali M., Aparicio A., 2005, *ARA&A*, 43, 387
- Gallazzi A., Brinchmann J., Charlot S., White S. D. M., 2008, *MNRAS*, 383, 1439
- Garrison-Kimmel S., Boylan-Kolchin M., Bullock J. S., Lee K., 2014, *MNRAS*, 438, 2578
- Geisler D., Wallerstein G., Smith V. V., Casetti-Dinescu D. I., 2007, *PASP*, 119, 939
- Goddard D., Thomas D., Maraston C., Westfall K., Etherington J., Riffel R., Mallmann N. D., Zheng Z., Argudo-Fernández M., Lian J., Bershadsky M., Bundy K., et al. 2017, *MNRAS*, 466, 4731
- Gratton R. G., Carretta E., Bragaglia A., 2012, *A&A Rev.*, 20, 50
- Gratton R. G., Carretta E., Bragaglia A., Lucatello S., D’Orazi V., 2010, *A&A*, 517, A81
- Gratton R. G., Lucatello S., Carretta E., Bragaglia A., D’Orazi V., Momany Y. A., 2011, *A&A*, 534, A123
- Greggio L., Falomo R., Zaggia S., Fantinel D., Uslenghi M., 2012, *PASP*, 124, 653

- Grillmair C. J., Lauer T. R., Worthey G., Faber S. M., Freedman W. L., Madore B. F., Ajhar E. A., Baum W. A., Holtzman J. A., Lynds C. R., O'Neil Jr. E. J., Stetson P. B., 1996, *AJ*, 112, 1975
- Grocholski A. J., van der Marel R. P., Aloisi A., Annibali F., Greggio L., Tosi M., 2012, *AJ*, 143, 117
- Grundahl F., VandenBerg D. A., Andersen M. I., 1998, *ApJl*, 500, L179
- Gruyters P., Casagrande L., Milone A. P., Hodgkin S. T., Serenelli A., Feltzing S., 2017, *A&A*, 603, A37
- Harbeck D., Grebel E. K., Holtzman J., Guhathakurta P., Brandner W., Geisler D., Sarajedini A., Dolphin A., Hurley-Keller D., Mateo M., 2001, *AJ*, 122, 3092
- Harris J., Zaritsky D., 2001, *ApJS*, 136, 25
- Harris J., Zaritsky D., , 2012, *StarFISH: For Inferring Star-formation Histories*, *Astrophysics Source Code Library*
- Harris W. E., 1996, *AJ*, 112, 1487
- Helmi A., Irwin M. J., Tolstoy E., Battaglia G., Hill V., Jablonka P., Venn K., Shetrone M., Letarte B., Arimoto N., Abel T., Francois P., Kaufer A., Primas F., Sadakane K., Szeifert T., 2006, *ApJl*, 651, L121
- Hidalgo S. L., Aparicio A., Skillman E., Monelli M., Gallart C., Cole A., Dolphin A., Weisz D., Bernard E. J., Cassisi S., Mayer L., Stetson P., Tolstoy E., Ferguson H., 2011, *ApJ*, 730, 14
- Hubble E. P., 1925, *ApJ*, 62
- Hubble E. P., 1926, *ApJ*, 63
- Hubble E. P., 1929, *ApJ*, 69
- Hurley-Keller D., Mateo M., Nemec J., 1998, *AJ*, 115, 1840
- Ibata R., Chapman S., Irwin M., Lewis G., Martin N., 2006, *MNRAS*, 373, L70

- Iben Jr. I., Rood R. T., 1970, *ApJ*, 161, 587
- Johnson C. I., Pilachowski C. A., 2012, *ApJl*, 754, L38
- Karachentsev I. D., Makarov D. I., Kaisina E. I., 2013, *AJ*, 145, 101
- Kleyna J., Wilkinson M. I., Evans N. W., Gilmore G., Frayn C., 2002, *MNRAS*, 330, 792
- Koch A., Grebel E. K., Gilmore G. F., Wyse R. F. G., Kleyna J. T., Harbeck D. R., Wilkinson M. I., Wyn Evans N., 2008, *AJ*, 135, 1580
- Koch A., Grebel E. K., Wyse R. F. G., Kleyna J. T., Wilkinson M. I., Harbeck D. R., Gilmore G. F., Evans N. W., 2006, *AJ*, 131, 895
- Koch A., Kleyna J. T., Wilkinson M. I., Grebel E. K., Gilmore G. F., Evans N. W., Wyse R. F. G., Harbeck D. R., 2007, *AJ*, 134, 566
- Kraft R. P., 1979, *ARA&A*, 17, 309
- Kroupa P., 2001, *MNRAS*, 322, 231
- Lanfranchi G. A., Matteucci F., 2004, *MNRAS*, 351, 1338
- Lapenna E., Lardo C., Mucciarelli A., Salaris M., Ferraro F. R., Lanzoni B., Massari D., Stetson P. B., Cassisi S., Savino A., 2016, *ApJl*, 826, L1
- Lardo C., Bellazzini M., Pancino E., Carretta E., Bragaglia A., Dalessandro E., 2011, *A&A*, 525, A114
- Lardo C., Salaris M., Savino A., Donati P., Stetson P. B., Cassisi S., 2017, *MNRAS*, 466, 3507
- Larsen S. S., Baumgardt H., Bastian N., Brodie J. P., Grundahl F., Strader J., 2015, *ApJ*, 804, 71
- Larsen S. S., Brodie J. P., Grundahl F., Strader J., 2014, *ApJ*, 797, 15
- Lee J.-W., 2017, ArXiv e-prints

- Lehnert M. D., Bell R. A., Hesser J. E., Oke J. B., 1992, *ApJ*, 395, 466
- Lemasle B., Hill V., Tolstoy E., Venn K. A., Shetrone M. D., Irwin M. J., de Boer T. J. L., Starkenburg E., Salvadori S., 2012, *A&A*, 538, A100
- Letarte B., Hill V., Jablonka P., Tolstoy E., François P., Meylan G., 2006, *A&A*, 453, 547
- Lianou S., Grebel E. K., Da Costa G. S., Rejkuba M., Jerjen H., Koch A., 2013, *A&A*, 550, A7
- MacLean B. T., Campbell S. W., De Silva G. M., Lattanzio J., D’Orazi V., Simpson J. D., Momany Y., 2016, *MNRAS*, 460, L69
- Madau P., Dickinson M., 2014, *ARA&A*, 52, 415
- Majewski S. R., Siegel M. H., Patterson R. J., Rood R. T., 1999, *ApJl*, 520, L33
- Marino A. F., Villanova S., Piotto G., Milone A. P., Momany Y., Bedin L. R., Medling A. M., 2008, *A&A*, 490, 625
- Martin N. F., Ibata R. A., Lewis G. F., McConnachie A., Babul A., Bate N. F., Bernard E., Chapman S. C., Collins M. M. L., Conn A. R., Crnojević D., Fardal M. A., Ferguson A. M. N., Irwin M., Mackey A. D., McMonigal B., Navarro J. F., Rich R. M., 2016, *ApJ*, 833, 167
- Martin N. F., Weisz D. R., Albers S. M., Bernard E., Collins M. L. M., Dolphin A. E., Ferguson A. M. N., Ibata R. A., Laevens B., Lewis G. F., Mackey A. D., McConnachie A., Rich R. M., Skillman E. D., 2017, *ApJ*, 850, 16
- Martínez-Vázquez C. E., Stetson P. B., Monelli M., Bernard E. J., Fiorentino G., Gallart C., Bono G., Cassisi S., Dall’Ora M., Ferraro I., Iannicola G., Walker A. R., 2016, *MNRAS*, 462, 4349
- Massari D., Lapenna E., Bragaglia A., Dalessandro E., Contreras Ramos R., Amigo P., 2016, *MNRAS*, 458, 4162
- Mateo M., Hurley-Keller D., Nemeč J., 1998, *AJ*, 115, 1856

- Mighell K. J., 1990, *A&AS*, 82, 1
- Milone A. P., Piotto G., Bedin L. R., King I. R., Anderson J., Marino A. F., Bellini A., Gratton R., Renzini A., Stetson P. B., et al. 2012, *ApJ*, 744, 58
- Milone A. P., Piotto G., Renzini A., Marino A. F., Bedin L. R., Vesperini E., D'Antona F., Nardiello D., Anderson J., King I. R., et al. 2017, *MNRAS*, 464, 3636
- Moffat A. F. J., 1969, *A&A*, 3, 455
- Monelli M., Cassisi S., Bernard E. J., Hidalgo S. L., Aparicio A., Gallart C., Skillman E. D., 2010, *ApJ*, 718, 707
- Monelli M., Gallart C., Hidalgo S. L., Aparicio A., Skillman E. D., Cole A. A., Weisz D. R., Mayer L., Bernard E. J., Cassisi S., Dolphin A. E., Drozdovsky I., Stetson P. B., 2010, *ApJ*, 722, 1864
- Monelli M., Pulone L., Corsi C. E., Castellani M., Bono G., Walker A. R., Brocato E., Buonanno R., Caputo F., Castellani V., Dall'Ora M., Marconi M., Nonino M., Ripepi V., Smith H. A., 2003, *AJ*, 126, 218
- Monkiewicz J., Mould J. R., Gallagher III J. S., Clarke J. T., Trauger J. T., Grillmair C., Ballester G. E., Burrows C. J., Crisp D., Evans R., Griffiths R., Hester et al. 1999, *PASP*, 111, 1392
- Mould J., Kristian J., Da Costa G. S., 1984, *ApJ*, 278, 575
- Mucciarelli A., Bellazzini M., Ibata R., Merle T., Chapman S. C., Dalessandro E., Sollima A., 2012, *MNRAS*, 426, 2889
- Mucciarelli A., Origlia L., Ferraro F. R., Pancino E., 2009, *ApJl*, 695, L134
- Nardiello D., Milone A. P., Piotto G., Anderson J., Bedin L. R., Bellini A., Cassisi S., Libralato M., Marino A. F., 2018, *MNRAS*, 477, 2004
- Nardiello D., Milone A. P., Piotto G., Marino A. F., Bellini A., Cassisi S., 2015, *A&A*, 573, A70

- Nelder J. A., Mead R., 1965, *Computer Journal*, 7, 308
- Origlia L., Ferraro F. R., Fabbri S., Fusi Pecci F., Dalessandro E., Rich R. M., Valenti E., 2014, *A&A*, 564, A136
- Pasetto S., Grebel E. K., Berczik P., Chiosi C., Spurzem R., 2011, *A&A*, 525, A99
- Pietrinferni A., Cassisi S., Salaris M., Castelli F., 2004, *ApJ*, 612, 168
- Pietrinferni A., Cassisi S., Salaris M., Castelli F., 2006, *ApJ*, 642, 797
- Pilachowski C. A., Sneden C., Wallerstein G., 1983, *ApJS*, 52, 241
- Piotto G., 2009, in Mamajek E. E., Soderblom D. R., Wyse R. F. G., eds, *The Ages of Stars Vol. 258 of IAU Symposium, Observations of multiple populations in star clusters*. pp 233–244
- Piotto G., Bedin L. R., Anderson J., King I. R., Cassisi S., Milone A. P., Villanova S., Pietrinferni A., Renzini A., 2007, *ApJ*, 661, L53
- Piotto G., Milone A. P., Anderson J., Bedin L. R., Bellini A., Cassisi S., Marino A. F., Aparicio A., Nascimbeni V., 2012, *ApJ*, 760, 39
- Piotto G., Milone A. P., Bedin L. R., Anderson J., King I. R., Marino A. F., Nardiello D., Aparicio A., Barbay B., Bellini A., Brown T. M., Cassisi S., Cool A. M., Cunial A., et al. 2015, *AJ*, 149, 91
- Press W. H., Teukolsky S. A., Vetterling W. T., Flannery B. P., 1992, *Numerical recipes in FORTRAN. The art of scientific computing*
- Preston G. W., Sheckman S. A., Beers T. C., 1991, *ApJ*, 375, 121
- Rejkuba M., Harris W. E., Greggio L., Harris G. L. H., 2011, *A&A*, 526, A123
- Renzini A., Buzzoni A., 1986, in Chiosi C., Renzini A., eds, *Spectral Evolution of Galaxies Vol. 122 of Astrophysics and Space Science Library, Global properties of stellar populations and the spectral evolution of galaxies*. pp 195–231

- Renzini A., D'Antona F., Cassisi S., King I. R., Milone A. P., Ventura P., Anderson J., Bedin L. R., Bellini A., Brown T. M., et al. 2015, *MNRAS*, 454, 4197
- Revaz Y., Jablonka P., Sawala T., Hill V., Letarte B., Irwin M., Battaglia G., Helmi A., Shetrone M. D., Tolstoy E., Venn K. A., 2009, *A&A*, 501, 189
- Rizzi L., Held E. V., Bertelli G., Saviane I., 2003, *ApJl*, 589, L85
- Roh D.-G., Lee Y.-W., Joo S.-J., Han S.-I., Sohn Y.-J., Lee J.-W., 2011, *ApJl*, 733, L45
- Romano D., Starkenburg E., 2013, *MNRAS*, 434, 471
- Sacchi E., Annibali F., Cignoni M., Aloisi A., Sohn T., Tosi M., van der Marel R. P., Grocholski A. J., James B., 2016, *ApJ*, 830, 3
- Saha A., Monet D. G., Seitzer P., 1986, *AJ*, 92, 302
- Salaris M., Cassisi S., 2005, *Evolution of Stars and Stellar Populations*
- Salaris M., Chieffi A., Straniero O., 1993, *ApJ*, 414, 580
- Salaris M., de Boer T., Tolstoy E., Fiorentino G., Cassisi S., 2013, *A&A*, 559, A57
- Salvadori S., Ferrara A., Schneider R., 2008, *MNRAS*, 386, 348
- Sandage A., Wallerstein G., 1960, *ApJ*, 131, 598
- Santucci R. M., Beers T. C., Placco V. M., Carollo D., Rossi S., Lee Y. S., Denissenkov P., Tumlinson J., Tissera P. B., 2015, *ApJl*, 813, L16
- Sarajedini A., Bedin L. R., Chaboyer B., Dotter A., Siegel M., Anderson J., Aparicio A., King I., Majewski S., Marín-Franch A., Piotto G., Reid I. N., Rosenberg A., 2007, *AJ*, 133, 1658
- Savino A., Massari D., Bragaglia A., Dalessandro E., Tolstoy E., 2018, *MNRAS*, 474, 4438
- Savino A., Salaris M., Tolstoy E., 2015, *A&A*, 583, A126
- Sbordone L., Salaris M., Weiss A., Cassisi S., 2011, *A&A*, 534, A9

- Schlegel D. J., Finkbeiner D. P., Davis M., 1998, *ApJ*, 500, 525
- Schulte-Ladbeck R. E., Hopp U., Drozdovsky I. O., Greggio L., Crone M. M., 2002, *AJ*, 124, 896
- Shetrone M., Venn K. A., Tolstoy E., Primas F., Hill V., Kaufer A., 2003, *AJ*, 125, 684
- Skrutskie M. F., Cutri R. M., Stiening R., Weinberg M. D., Schneider S., Carpenter J. M., Beichman C., Capps R., Chester T., Elias J., Huchra J., Liebert J., et al. 2006, *AJ*, 131, 1163
- Small E. E., Bersier D., Salaris M., 2013, *MNRAS*, 428, 763
- Smecker-Hane T. A., Mandushev G. I., Hesser J. E., Stetson P. B., Da Costa G. S., Hatzidimitriou D., 1999, in Hubeny I., Heap S., Cornett R., eds, *Spectrophotometric Dating of Stars and Galaxies Vol. 192 of Astronomical Society of the Pacific Conference Series, Chemical Abundances in the Carina dSph Galaxy*. p. 159
- Smecker-Hane T. A., Stetson P. B., Hesser J. E., Lehnert M. D., 1994, *AJ*, 108, 507
- Smecker-Hane T. A., Stetson P. B., Hesser J. E., Vandenberg D. A., 1996, in Leitherer C., Fritze-von-Alvensleben U., Huchra J., eds, *From Stars to Galaxies: the Impact of Stellar Physics on Galaxy Evolution Vol. 98 of Astronomical Society of the Pacific Conference Series, Episodic Star Formation in the Carina dSph Galaxy*. p. 328
- Snedden C., Kraft R. P., Guhathakurta P., Peterson R. C., Fulbright J. P., 2004, *AJ*, 127, 2162
- Sorce J. G., Gottlöber S., Yepes G., Hoffman Y., Courtois H. M., Steinmetz M., Tully R. B., Pomarède D., Carlesi E., 2016, *MNRAS*, 455, 2078
- Soto M., Bellini A., Anderson J., Piotto G., Bedin L. R., van der Marel R. P., Milone A. P., Brown T. M., Cool A. M., King I. R., Sarajedini A., Granata V., Cassisi S., Aparicio A., Hidalgo S., Ortolani S., Nardiello D., 2017, *AJ*, 153, 19
- Spitzer L., 1987, *Dynamical evolution of globular clusters*. Princeton, NJ, Princeton University Press, 1987, 191 p.

- Spruit H. C., 2015, ArXiv e-prints
- Starkenburger E., Helmi A., De Lucia G., Li Y.-S., Navarro J. F., Font A. S., Frenk C. S., Springel V., Vera-Ciro C. A., White S. D. M., 2013, MNRAS, 429, 725
- Starkenburger E., Hill V., Tolstoy E., González Hernández J. I., Irwin M., Helmi A., Battaglia G., Jablonka P., Tafelmeyer M., Shetrone M., Venn K., de Boer T., 2010, A&A, 513, A34
- Stetson P. B., 1987, PASP, 99, 191
- Stetson P. B., 1994, PASP, 106, 250
- Stetson P. B., Hesser J. E., Smecker-Hane T. A., 1998, PASP, 110, 533
- Suntzeff N. B., Mateo M., Terndrup D. M., Olszewski E. W., Geisler D., Weller W., 1993, ApJ, 418, 208
- Tailo M., Di Criscienzo M., D'Antona F., Caloi V., Ventura P., 2016, MNRAS, 457, 4525
- Tolstoy E., Hill V., Tosi M., 2009, ARA&A, 47, 371
- Tolstoy E., Irwin M. J., Helmi A., Battaglia G., Jablonka P., Hill V., Venn K. A., Shetrone M. D., Letarte B., Cole A. A., Primas F., Francois P., Arimoto N., Sadakane K., Kaufer A., Szeifert T., Abel T., 2004, ApJ, 617, L119
- Tolstoy E., Saha A., 1996, ApJ, 462, 672
- Tolstoy E., Venn K. A., Shetrone M., Primas F., Hill V., Kaufer A., Szeifert T., 2003, AJ, 125, 707
- Tosi M., Greggio L., Marconi G., Focardi P., 1991, AJ, 102, 951
- VandenBerg D. A., Stetson P. B., Brown T. M., 2015, ApJ, 805, 103
- Venn K. A., Shetrone M. D., Irwin M. J., Hill V., Jablonka P., Tolstoy E., Lemasle B., Divell M., Starkenburg E., Letarte B., Baldner C., Battaglia G., Helmi A., Kaufer A., Primas F., 2012, ApJ, 751, 102

- Ventura P., D'Antona F., Mazzitelli I., Gratton R., 2001, *ApJ*, 550, L65
- Vesperini E., McMillan S. L. W., D'Antona F., D'Ercole A., 2013, *MNRAS*, 429, 1913
- Walker M. G., Mateo M., Olszewski E. W., Peñarrubia J., Wyn Evans N., Gilmore G., 2009, *ApJ*, 704, 1274
- Walker M. G., Peñarrubia J., 2011, *ApJ*, 742, 20
- Weisz D. R., Dalcanton J. J., Williams B. F., Gilbert K. M., Skillman E. D., Seth A. C., Dolphin A. E., McQuinn K. B. W., Gogarten S. M., Holtzman J., Rosema K., Cole A., Karachentsev I. D., Zaritsky D., 2011, *ApJ*, 739, 5
- Weisz D. R., Dolphin A. E., Skillman E. D., Holtzman J., Gilbert K. M., Dalcanton J. J., Williams B. F., 2014, *ApJ*, 789, 147
- Weisz D. R., Skillman E. D., Hidalgo S. L., Monelli M., Dolphin A. E., McConnachie A., Bernard E. J., Gallart C., Aparicio A., Boylan-Kolchin M., Cassisi S., Cole A. A., et al. 2014, *ApJ*, 789, 24
- White S. D. M., Rees M. J., 1978, *MNRAS*, 183, 341
- Willson L. A., 2000, *ARA&A*, 38, 573
- Yong D., Grundahl F., Johnson J. A., Asplund M., 2008, *ApJ*, 684, 1159
- Zhu L., van de Ven G., Watkins L. L., Posti L., 2016, *MNRAS*, 463, 1117
- Zinn R., 1978, *ApJ*, 225, 790
- Zinn R., 1981, *ApJ*, 251, 52